2015-07-01

Transport Enhancement of Rate-Limited Chemical Reactions via Pt-Decorated, Carbon Nanotube Microarray Membranes

Kevin M. Marr
Brigham Young University - Provo

Transport Enhancement of Rate-Limited Chemical Reactions *via* Pt-Decorated, Carbon Nanotube Microarray Membranes

Kevin M. Marr

A thesis submitted to the faculty of
Brigham Young University
in partial fulfillment of the requirements for the degree of

Master of Science

Brian D. Iverson, Chair
Brian D. Jensen
Richard K. Watt

Department of Mechanical Engineering

Brigham Young University

July 2015

ABSTRACT

Transport Enhancement of Rate-Limited Chemical Reactions *via* Pt-Decorated, Carbon Nanotube Microarray Membranes

Kevin M. Marr
Department of Mechanical Engineering, BYU
Master of Science

Rate limited chemical reactions can be enhanced by improving the mass transport of the suspended analyte to the catalytic (or electrocatalytic) surface. While many attempts have been made to enhance this mass transport, these approaches are limited to utilizing only two enhancement methods – increasing available catalytic surface area, and increasing the flow of analyte in solution. Flow through high aspect ratio microstructures, however, would provide additional mass transport enhancement *via* boundary layer confinement. Platinum functionalized carbon nanotube microarray membranes (Pt-CNT-MMs) offer enhanced mass transport *via* all three methods, and were fabricated for demonstration in a H_2O_2 sample system, for which propulsion and chemical sensing applications were investigated.

Propulsion testing of Pt-CNT-MM samples demonstrated thrust typically required for MUV propulsion, while achieving high H_2O_2 fuel utilization. Also, the proposed approach minimizes component exposure to the environment and is comprised of a simple, static architecture relative to other micro-propulsion systems. Moreover, it was shown that additional thrust is attainable by further enhancing the introductory rate of the H_2O_2 fuel to the Pt-CNT-MMs, which would effectively increase the locomotive capability of this propulsion system.

Pt-CNT-MMs used for chemical sensing of H_2O_2 likewise demonstrated favorable performance. Initial studies revealed that the molar flux achieved for a Pt-CNT-MM sample in a through-flow environment (50 [$\mu L\ s^{-1}$]) was approximately a ten-fold increase over that achieved in a stirred environment (150 [rpm]). This ten-fold increase in molar flux can be attributed to both an increase in exposed electrocatalytic surface area, as well as increase in boundary layer confinement. Furthermore, comparison of sensed molar flux to calculated molar flux for through-flow conditions revealed that Pt-CNT-MMs can achieve near-complete H_2O_2 oxidation within the flowrate range studied. Additionally, chronoamperometric testing of a Pt-CNT-MM sample demonstrated a sensitivity toward H_2O_2 of 9.18 [mA mM^{-1} cm^{-2}], over one hundred times that of the GluOx/Pt-SWCNT/PAA structures referenced herein (0.0724 [mA mM^{-1} cm^{-2}]).[1]

These findings suggest that mass transport enhancement, achieved by Pt-CNT-MMs applied in through-flow environments, heightens the performance achieved in rate-limited chemical reactions. Specifically, Pt-CNT-MMs demonstrate high fuel utilization in H_2O_2 based propulsion applications, as well as offer a highly sensitive preliminary structures for non-invasive glucose sensing.

Keywords: carbon nanotube, hydrogen peroxide, platinum, nanoparticle, microchannel

ACKNOWLEDGEMENTS

Looking back on all of the research and work that has been accomplished, and is addressed in this thesis, I recognize how very much of this would not even be imaginable without the help, support, and mentoring of so many individuals. I address them here, acknowledging their critical roles in this work.

First and foremost is Dr Brian Iverson – his mentoring has helped shape me into a self-motivated and capable researcher. I also here acknowledge Dr. Brian Jensen and Richard Watt for their support and encouragement throughout my studies. Also, I would like to gratefully acknowledge Jonathan Claussen for introducing me to much of the processes and testing used within this work. Also, I wanted to thank Trevor Smith for providing so much help with our electrochemistry studies.

Our collaborators, including individuals from NRL and Iowa State University, have also provided invaluable support in our propulsion-related studies. These individuals include Jonathan Claussen, Eric Mootz, Jason Geder, Bolin Chen, Marius Pruessner, and Brian Melde.

Others here at BYU have provided help and assistance in a number of ways. I would like to thank Dr. Richard Vanfleet for help with TEM characterization as well as his insight shared at our weekly CNT meetings. Also, I would like to thank Nick Hawkins for his help in machining of our through-flow Teflon flow cell, as well as Kevin Cole for access to instrumentation. Thanks to Mike Standing for his training me to use the SEM facilities. Friends, including Jason Lund, Lawrence Barrett, and John Stout, have also helped in teaching me a variety of topics including CNT growth and microfabrication.

Of particular note are Carson Storey and Ben Brownlee. They have both worked *very* diligently alongside me throughout much of this work. In particular, Carson provided invaluable

work in fabricating our new lithography masks, documenting said work, and machining our deposition Teflon flow cell. Ben also has spent many hours learning electrochemistry, coding the associated software (MATLAB) and performing tests, which are presented herein. Thank you to you both.

I would also like to give special thanks to my wonderful wife Kaytlyn, who has always given me the patient support and kindness I needed to accomplish all that I have. Thank you for being interested in my work, and investing in me. I love you Kaytlyn.

Lastly, and above all, I recognize the Lord's hand through it all. For truly, "all things denote there is a God; yea, even the earth, and things that are upon the face of it" (Alma 30:44).

TABLE OF CONTENTS

LIST OF TABLES

LIST OF FIGURES

CHAPTER 1. INTRODUCTION

1.1 Conventional Methods for Enhancing 'Rate-Limited' Chemical Reactions

Chemical reactions involving catalytic structures or surfaces are commonly rate-limited, by nature. Rate limiting reactions are present when the rate of reaction *at* a catalytic surface does not match the rate of molecule (analyte) introduction *to* that surface. In many cases, it is the catalytic reaction rate that exceeds the analyte introduction rate. In other words, the overall chemical reaction is inhibited by the introduction rate of fresh analyte to the catalytic surface.

Many attempts have been made to enhance the introduction rate of analyte to a catalytic surface for the purpose of improving chemical reactions or processes. Methods for the improvement of analyte introduction rates are apparent in the governing equation for mass transport,

$$N_A = \bar{h}_m A_s (C_{A,s} - C_{A,\infty}) \quad (1)$$

where N_A is the molar transfer rate [mol s^{-1}], $\bar{h}_m$ is the mass transport coefficient [m s^{-1}], A_s is the surface area [m^2] and the term in parenthesis is the molar concentration difference between the surface and far from the surface [mol m^{-3}]. For a fixed concentration difference, enhancement of the introduction rate N_A can be achieved by increasing $\bar{h}_m$ (often by increasing the flow rate of analyte in solution), or by increasing the available catalytic surface area, A_s.

Enhancement of the analyte introduction rate is often achieved by simply increasing the flow rate of the analyte in solution. This can be achieved by increasing the concentration of analyte

in solution for given flow rate or increasing the flow rate directly. As the motion of the analyte is promoted by sonication, stirring, mixing, or other means, the probability of a given analyte to encounter a catalytic surface increases. For this reason, several recent studies have investigated catalytic structures, which move through the analyte solution,[2-7] thus increasing the *apparent* analyte flow and enhancing its introduction rate.

Enhancement of the analyte introduction rate can also be achieved by simply increasing the available catalytic surface area. For most applications, however, there is an upper limit to how large a catalytic surface can be, without becoming cumbersome or impractical. Microfabricated sensors have become ubiquitous and minimize the catalyst's spatial footprint; much research has been devoted to the fabrication of high surface area microstructures in order to maximize surface area for small sensor volumes. Microstructures such as three-dimensional graphene,[8-10] magnesium oxide,[11-13] and zeolites,[14-16] all possess considerable surface area and can either be used as a catalyst for a given chemical reaction or, if necessary, be appropriately functionalized with catalytic material (Figure 1-1). Use of these high surface area microstructures for catalytic-based applications promote intimate contact between a given analyte and its associated catalytic surface, while minimizing the structure's spatial footprint.

Many alternative high surface area microstructures appear as 2-D surfaces with some extension of the surface topography into the chemical flow field. Alternatively, high-aspect ratio microstructures (pillars, channels, *etc*.) allow for large exposure of surface area to chemical volume which facilitates enhanced mass transport much in the same way as fins enhance heat transfer.[17,18] The utility of enhanced surface area structures in the literature have been shown to outperform related planar geometries.[19,20]

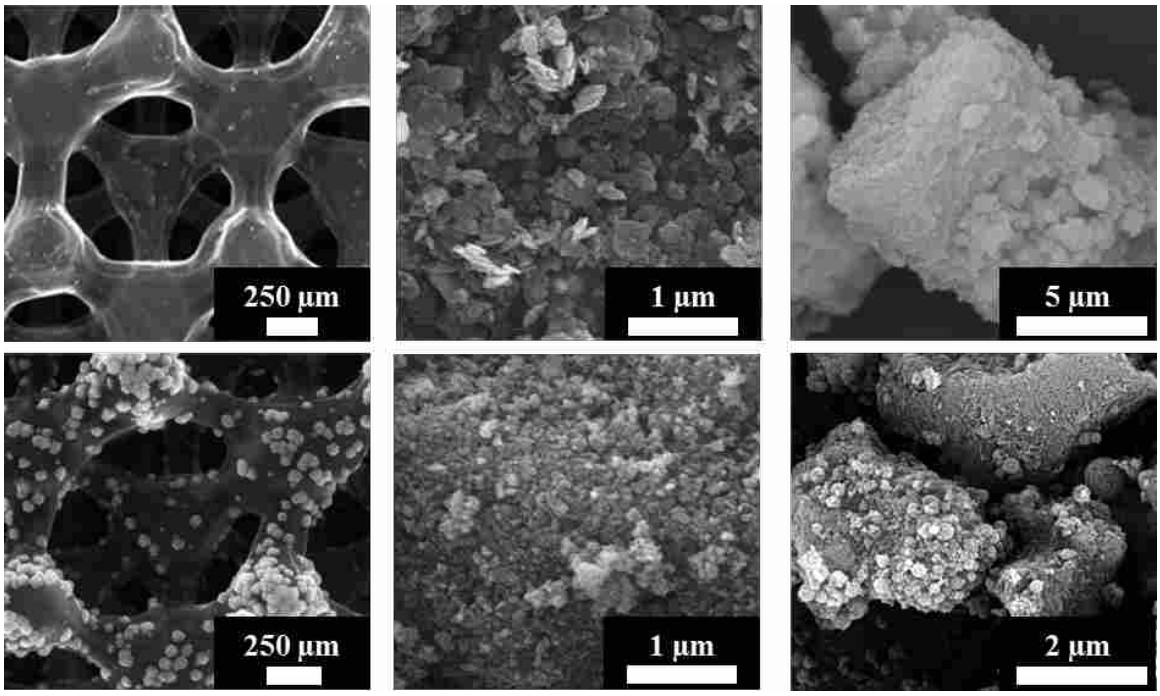

(a) (b) (c)

Figure 1-1: High surface area microstructures for catalyst support including **(a)** three-dimensional graphene,[8] **(b)** magnesium oxide,[11] and **(c)** zeolite[16] microstructures. Upper and lower images indicate before and after catalyst functionalization, respectively.

Although enhancement of the introduction rate of analyte to catalyst surface is readily achieved by increasing the flow of analyte solution and employing high-aspect ratio microstructures, these traditional methods fail to capitalize on a third enhancement method – boundary layer confinement through the use of high-aspect ratio microchannels (with large length to diameter ratios) which afford very high surface area to chemical volume ratios.

1.2 Enhancement of 'Rate-Limited' Reactions *via* Boundary Layer Confinement

While external flow *past* high-aspect ratio microstructures provides enhanced mass transport, internal flow *through* high-aspect ratio microstructures allows for a third enhancement method – boundary layer confinement. For flow in a confined geometry such as a channel,

boundary layer growth is limited once the boundary layers have merged ('Method 3' of Figure 1-2). An analyte in solution therefore has a maximum transport distance of half the channel diameter once boundary layers have merged and fully developed conditions have been reached. This improvement is much like using a microchannel heat exchanger in place of a finned heat sink. The ability to reduce and then limit the thermal boundary layer growth of a free stream fluid, flowing across a microchannel surface, enhances thermal transport between the surface and fluid. Likewise, restricting the growth of the concentration boundary layer allows for enhanced mass transport between that surface and solution. Boundary layer growth can be reduced or limited by either increasing the fluid flow, and/or imposing a physical confinement on the mass transport. As the microchannel diameter is reduced, the concentration boundary layer growth is limited resulting in shorter transport lengths and high mass transport coefficients. Specifically, the mass transport coefficient ($\bar{h}_m$) is very high for small hydraulic diameters (D_h), as $\bar{h}_m$ is proportional to $1/D_h$.

Combining increased analyte flow, high catalytic surface area, *and* boundary layer confinement could be realized using geometry as shown in Figure 1-2. This geometry is referred to as a high-aspect ratio microarray membrane, and it is anticipated that fabrication of such a microstructure would allow for considerable improvement on current approaches for catalytic-based chemical reactions. This microarray membrane arrangement enables millions of microchannels to be constructed in a parallel arrangement, drastically reducing the pressure required to drive the flow through a single, long channel with the same surface area as an array.

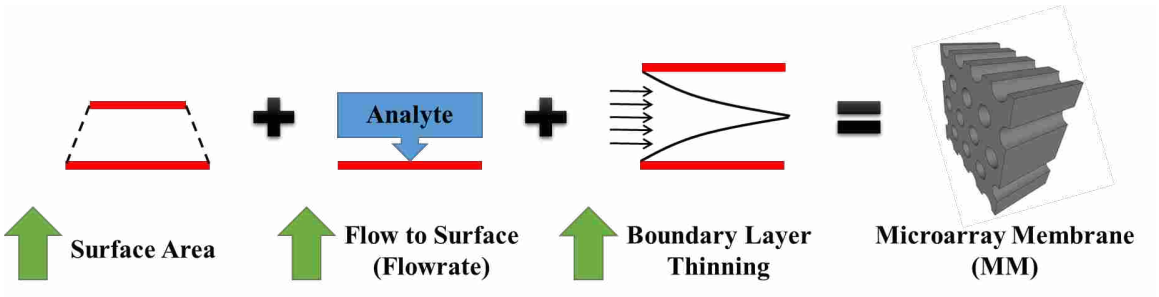

Figure 1-2: Microarray membrane structure envisioned from combination of mass transport enhancement methods.

The enhanced performance afforded by a microarray membrane structure can be demonstrated using a sample chemical system with hydrogen peroxide (H_2O_2). Catalytic microstructures are employed in propulsion and biosensing applications wherein H_2O_2 plays a central role.[2-7,10,21-24] The goal of this work was to successfully fabricate and characterize the microarray membranes and demonstrate the utility of these structures within a H_2O_2 sample system including propulsion and biosensing applications. Specifically, is it shown that these structures facilitate high fuel utilization for propulsion, and sensitivity for biosensing applications.

1.3 Thesis Objectives

Mass transport in catalyst-based chemical reactions can be enhanced by increasing the available catalytic surface area, increasing the flow of the analyte solution, and confining the concentration boundary layer. Flow of analyte solution through high-aspect ratio microstructures incorporates all three mass transport enhancements, thereby allowing for considerable improvement on current approaches. Fabrication and characterization of such a structure, and its successful demonstration in a chemical sample system, would validate its efficacy and provide opportunities for chemical applications yet to be explored.

This work aims to address the following objectives pertaining to chemical mass transport enhancement:

1. Synthesize a microarray membrane fabrication scheme.
2. Fabricate and characterize microarray membrane structure.
3. Demonstrate enhanced mass transport using microarray membrane in H_2O_2 sample system.
    - Underwater propulsion *via* decomposition of H_2O_2
    - H_2O_2 sensing for glucose detection applications

1.4 Thesis Accomplishments

1.4.1 Synthesized Fabrication Scheme for Microarray Membrane

A wide variety of fabrication processes are available for producing high aspect ratio microstructures. After outlining key design requirements for a microarray membrane, suitable fabrication and catalyst functionalization schemes were selected. Combining these schemes allowed for the fabrication and characterization of the resultant catalytic microarray membranes. Specifically, platinum (Pt) coated carbon nanotube microarray membranes (Pt-CNT-MMs) were used.

1.4.2 Fabricated and Characterized Pt-CNT-MMs

A suitable fabrication scheme for high aspect ratio microstructures was demonstrated and characterized using an electroless Pt deposition process. These microstructures were then characterized using scanning electron microscopy (SEM), transmission electron microscopy

(TEM), contact angle measurements, as well as surface area analysis using from Brunauer-Emmett-Teller (BET) analysis using nitrogen adsorption.

1.4.3 Demonstrated Mass Transport Enhancement in H_2O_2 Sample System

The efficacy of mass transport enhancement for rate-limited chemical reactions was demonstrated using a H_2O_2 sample system for the following applications:

- Underwater Propulsion *via* H_2O_2 Decomposition
- Amperometric Sensing of H_2O_2 for Glucose Detection Applications

Testing within these applications revealed favorable performance and motivates further research using Pt-CNT-MM structures.

1.5 Thesis Contributions

While many publications report Pt nanoparticle deposition onto carbon structures, this work is the first to demonstrate Pt nanoparticle deposition onto carbon-infiltrated MWCNTs. Additionally, this work reports the successful union between CNT-templated microfabrication and chemical deposition of nanoparticles. Much of the work contained herein has been demonstrated to the academic community through a variety of conferences. These include the 67th Annual Meeting of the APS Division of Fluid Dynamics (San Francisco, CA; November 2014), as well as the ASME 2013 IMECE Conference (San Diego, CA; November 2013). Additionally, material regarding Pt-CNT-MM fabrication, characterization, and application to underwater propulsion is taken from a paper accepted for publication in ACS Nano.[25]

CHAPTER 2. SYNTHESIZED FABRICATION SCHEME

2.1 Introduction

To facilitate high mass transport rates in through-flow environments, the following attributes for a microchannel array are desirable:

- Electrically conductive
- High-aspect ratio microchannels (> 10)
- Mechanically robust material
- Geometrically versatile (microchannel shape, diameter, length, *etc*.)
- Amenable to catalyst functionalization

To facilitate simple and effective functionalization of the microarray membranes, the following catalyst attributes are desirable:

- Simple functionalization scheme
- Strong catalyst adherence to substrate material (robust, *etc*.)
- High catalytic responsiveness toward H_2O_2
- Controllable catalyst coverage and morphology

Schemes suitable to both the fabrication and functionalization of microarray membrane structures, according to the above specified design requirements, were researched in the literature; the following sections outline the selected approaches.

2.2 Microarray Membrane Fabrication Scheme

Fabrication of 3D microstructures has been studied extensively and has led to the development of a variety of approaches. Porous materials such as 3D graphene and carbon foams offer an electrically conductive substrate which can be functionalized with catalytic material.[8,26] Though such structures meet nearly all of the previously stated requirements, they are unable to provide an ordered array of microchannels which would confine growth of the concentration boundary layer.

Porous anodic alumina (PAA) offers a means to produce an ordered array of nanopores with tunable pore diameter.[27,28] Unfortunately, post-processing such as ion milling must be used to open pores capped by the barrier layer developed during fabrication.[29] Additionally, alumina is both nonconductive and brittle, which disqualify it from our search for candidate microstructures.

CNTs are often used in catalytic-based chemical reactions because of their conductivity, high electron transfer rate, and mechanical robustness.[30-32] CNT-templated microfabrication (CNT-M) is a new approach which has been demonstrated to fabricate high-aspect ratio microchannels, and other geometries, by capitalizing on the very large length to diameter ratios present for carbon nanotubes.[33,34] For modest growth lengths of 1 [mm] and a nominal 100 [nm] spacing between CNTs, aspect ratios of 10-10,000 are achievable for vertically aligned growth. When combined with lithographically defined growth, almost any aspect ratio in this range can be realized (Figure 2-1). This range is significantly better than typical etching techniques for high-aspect ratio structures such as Deep Reactive Ion Etching (DRIE) and offers distinct advantages over Lithography, Electroplating, and Molding (LIGA) in cost, time, and scalability.[33]

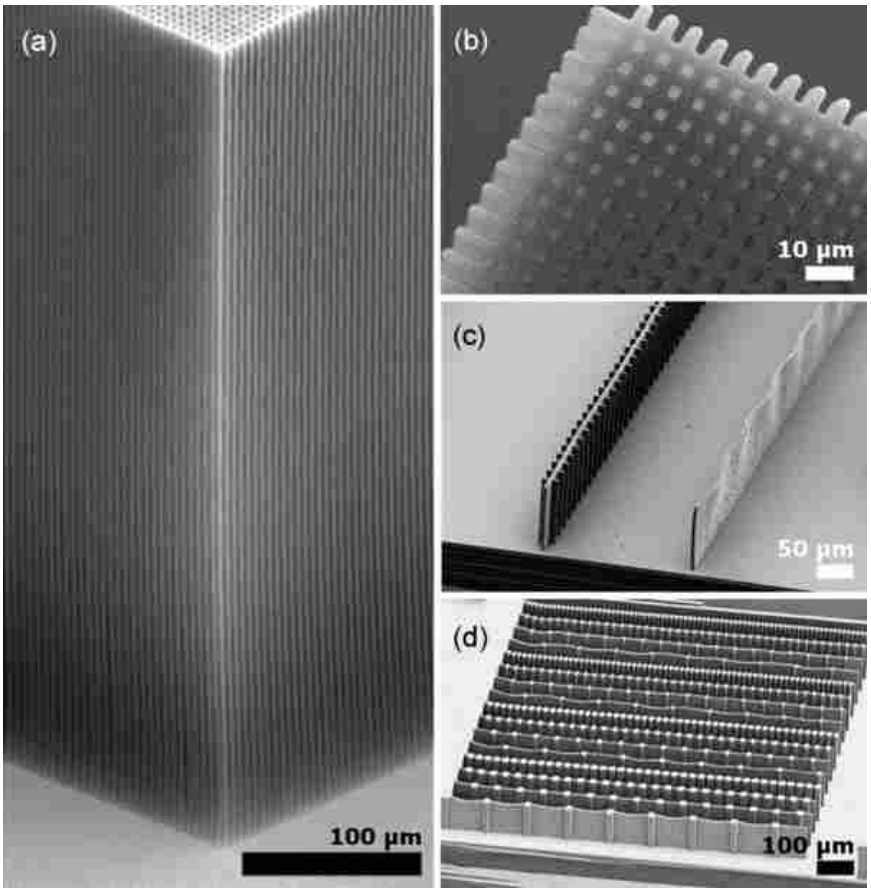

Figure 2-1: Example high-aspect ratio microstructures fabricated using CNT-templated microfabrication techniques. **(a)** Side and **(b)** top views of high-aspect ratio microchannel arrays. **(c-d)** Side views of self-supported high-aspect ratio geometries.[33]

Using patterned CNTs as a scaffold, additional materials can be coated on or 'infiltrated' into the forest, making these structures rigid and mechanically robust.[33] The conditions and duration of an infiltration procedure can be controlled to result in highly dense or highly porous regions. Therefore two-tier, porous materials can be constructed with CNT-M; larger (micron-scale) spacings controlled by lithography and smaller (nanometer-scale) spacings controlled by carbon nanotube forest density and subsequent infiltration. Multi-walled carbon nanotube microarray membranes (CNT-MMs) fabricated by this method thereby provide a geometrically versatile microstructure. Thus, this distinct CNT-M process enables the growth of aligned, high-

aspect ratio CNT micro-channel membranes – a three-dimensional microstructure that cannot be formed from conventional, stand-alone CNT fabrication techniques such as screen-printing,[35,36] electrospraying,[37] alcohol catalytic chemical vapor deposition,[38] plasma-enhanced chemical vapor deposition,[39-41] self-assembled monolayer linking,[42] and thermal crosslinking.[43]

Fabrication of CNT-MMs according to the practices cited above will provide a microstructure well suited for catalytic functionalization and use in through-flow environments. Specifically, the CNT-MMs will be high-aspect ratio microstructures composed of conductive, mechanically robust material, allow for geometric versatility, and will be amenable to catalyst functionalization.

2.3 Catalytic Functionalization Scheme

Functionalization of carbon based microstructures with catalytic materials has been demonstrated in the literature. In particular, atomic layer deposition (ALD) has been shown to deposit Pt onto CNT structures while allowing for good control over nanoparticle size.[44,45] Unfortunately, ALD is potentially time-intensive because it often requires many layering cycles to form the desired metal thickness on the substrate material.[46]

Electrodeposition is an attractive functionalization scheme because it offers control over the morphology and density of deposited nanoparticles.[10] Approaches include electrodepositing gold,[31,47,48] palladium,[1,39] and platinum[1,22] nanoparticles on CNTs. This scheme typically involves submersion of the microstructure in a metal suspension bath, as part of a three electrode cell. To simplify our approach, however, we sought an *electroless* deposition scheme.

Electroless deposition of Pt has been investigated on carbon based structures including carbon powders/spheres,[49-51] three-dimensional graphene,[8] and CNTs.[52,53] With a variety of proven deposition schemes for catalytic materials on carbon based microstructures, it is likely that similar

processes can be successfully adapted to functionalize CNT-MMs for H_2O_2 based reactions. Platinum deposition by the reduction of chloroplatinic acid is a simple, one-step process offering several advantages as demonstrated by Sun *et al*. (Figure 2-2).[49,52,53] Most notably is that the Pt nanoparticles are easily deposited and display strong adherence to carbon support structures. Furthermore, the Pt coverage and morphology on carbon structures is controllable, which allows for the coverage of high surface area microstructures with highly electrocatalytic nanoparticles.

Coverage of Pt nanoparticles on carbon scaffolds can be controlled by the relative loading of Pt precursor (chloroplatinic acid) to the carbon structure.[49,50] This is done on a *per mass* basis, and designated by '% [w/w] Pt-C.' It should be noted that these Pt-C loading ratios are made with respect to the initial mass of Pt in solution and initial carbon scaffold mass. While high % [w/w] Pt-C solutions help ensure coverage of the carbon substrate with Pt, highly dense Pt coverage results in the deposition of inaccessible or wasted Pt for H_2O_2 based reactions. Thus, careful consideration must be taken into account for finding optimal coverage while minimizing poor Pt utilization.

Previous work indicates that nanostructured morphologies can be tuned and subsequently exploited to enhance performance.[10,54,55] Specifically, 'needle-like' or 'urchin-like' structures display favorable catalytic activity because of their large surface area and desirable geometry (corners, edges, *etc.*).[56] Dense coverage of urchin-like Pt nanoparticles is produced as the reduction time of the Pt precursor is increased. This is realized when there is an abundance of H^+ ions in solution (*i.e.*, low pH; Figure 2-2e).[57]

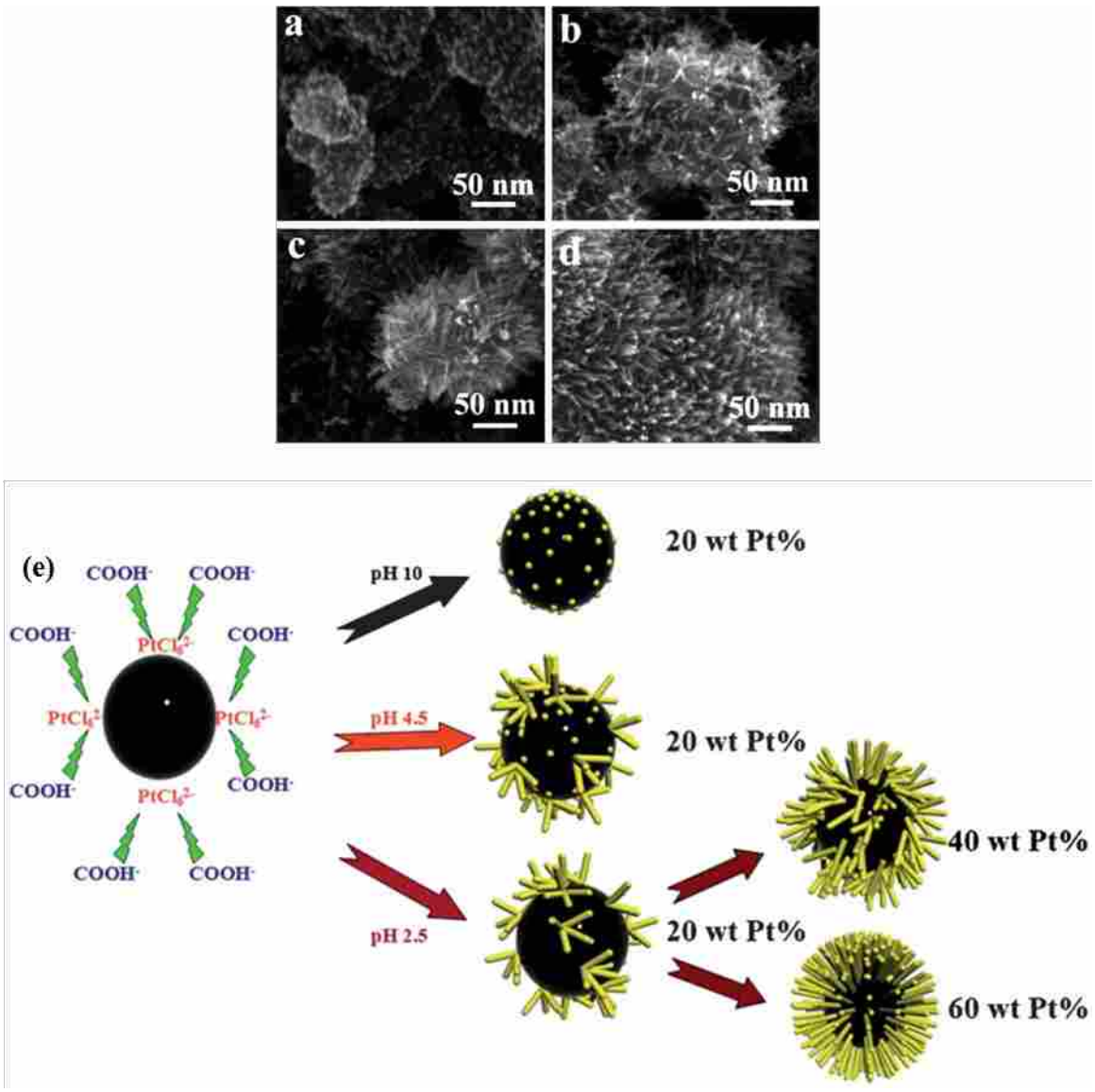

Figure 2-2: Various Pt nanoparticle morphology and coverage on carbon powder for conditions of **(a)** 20% [w/w] Pt-C, pH 10, **(b)** 20% [w/w] Pt-C, pH 2.5, **(c)** 40% [w/w] Pt-C, pH 2.5, and **(d)** 60% [w/w] Pt-C, pH 2.5. Pt nanoparticle coverage and morphology dependent on Pt-C loading and solution pH, respectively **(e)**.[49]

Given that no base additives are employed, and all other solution components are dispensed in a fixed amount, solution pH is inversely related to Pt loading (molarity). Thus, for a given

volume of solution, a highly catalytic Pt morphology with good surface coverage can be obtained by adjusting the Pt-C loading of the solution while maintaining a low solution pH (≤ 2.5).

Catalytic functionalization of CNT-MMs, according to the practices cited above, allows for ready production of Pt coated CNT-MMs (Pt-CNT-MMs) well suited to H_2O_2 based chemical reactions. The catalyst functionalization scheme is simple, and produces a Pt catalyst that displays both high adherence to its carbon substrate and high catalytic responsiveness toward H_2O_2. Furthermore, the deposition scheme allows for controllable Pt catalyst coverage and morphology.

Combination of the high aspect ratio CNT-MM geometry with the highly catalytic Pt nanoparticles will provide a microstructure well suited for catalytic reactions involving H_2O_2. Specifically, large H_2O_2 introduction rates should be realized *via* the Pt-CNT-MM microstructure as it permits mass transport enhancement using all three methods – increase of catalytic surface area, increase of flow of the H_2O_2 solution, and boundary layer confinement

CHAPTER 3. FABRICATION AND CHARACTERIZATION OF PT-CNT-MMS

3.1 Fabrication of Pt-CNT-MMs

The following sections describe in further detail the processes and capabilities associated with using CNT-M, as well as the procedures followed to fabricate Pt-CNT-MMs. Specifically, an overview of the CNT-M process and fabrication considerations is given along with a description of the microchannel geometries to be fabricated. Procedures followed for the fabrication and electroless functionalization of CNT-MMs with Pt nanoparticles are then provided.

3.1.1 CNT-M Background and Selected Microchannel Geometries

High-aspect ratio CNT-MMs were fabricated using CNT-M. This process consists of exploiting lithographically defined iron (Fe) catalyst regions to grow vertically aligned CNT forests in a quartz tube furnace with ethylene gas acting as the carbon feedstock gas (Figure 3-1, a-d). By a similar chemical vapor deposition (CVD) process, these CNT forests are infiltrated with a mixture of graphitic and amorphous carbon to coat the outer walls of the CNTs (Figure 3-1e). However, the potential exists for materials other than carbon to be infiltrated into the CNT-MM, as the application may require. In the extreme case, nearly all void space between CNTs can be filled with a desired material, thereby forming solid walls patterned according to the existing CNT layout during growth.[33] The variable porosity of the CNT structures is controlled in part by the exposure time of these structures to the infiltration process. Figure 3-1f shows a representative

carbon-infiltrated CNT-MM with low-porosity sidewall surfaces. The precise patterning capabilities of photolithography and the macro-scale growth size of CNTs, in conjunction with the added structural versatility afforded by CNT-M, allows for the creation of a variety of high-aspect ratio, nanocomposite materials of varying porosity/composition with enhanced structural integrity.[33,58]

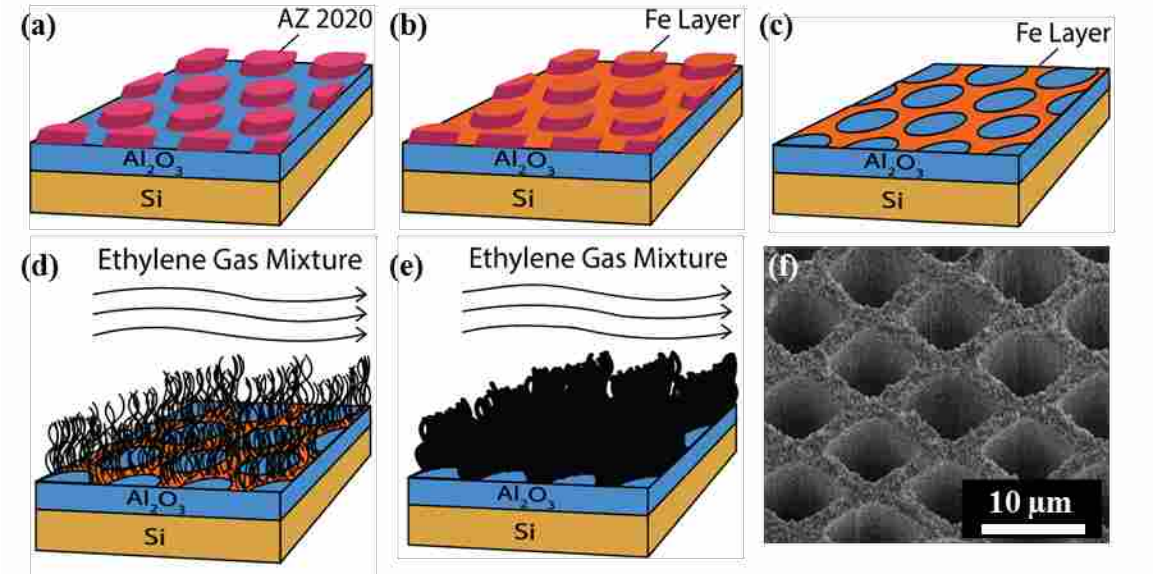

Figure 3-1: Multi-step fabrication process for a CNT-MM. **(a)** Step 1: photoresist patterned onto Si wafer coated with Al_2O_3. **(b)** Step 2: thermal evaporation of Fe for CNT growth. **(c)** Step 3: resultant Fe pattern after solvent lift-off process to obtain desired pattern. **(d)** Step 4: CVD growth of high-aspect ratio CNT-MMs (~600 [µm] height) with an ethylene gas mixture as the carbon feedstock gas. **(e)** Step 5: carbon-infiltration of CNT-MM; **(f)** SEM image of resultant CNT-MM structure (diamond pattern shown; hydraulic diameter of 4 [µm]).

The CNT-MMs studied in this work were patterned using three different photolithography masks. The first incorporated a close-packed, diamond-shaped channel used for fabrication of CNT-MMs having hydraulic diameters of 4.0 [µm] and a minimum wall thickness of ~2.0 [µm]. The fraction of the surface area occupied by channels to that filled by CNTs ('void ratio') imposed by this mask is approximately 0.704. The other two masks were fabricated such that they have also the same void ratio. Both have close-packed, circular channels with one mask comprised of 4.0

[μm] channel diameters and the other with 16.1 [μm] channel diameters (approximately four times that of the small circle mask; section A.2). Comparison of through-flow performance of CNT-MMs made using each of these masks enable studies regarding dependence on channel geometry and size. These studies are the topic of future investigation. A tutorial for the design of photolithography masks using KLayout, as well as the drawings for the CNT-MM patterns mentioned previously, are included in Appendix A.

3.1.2 Methods: CNT-MM Fabrication

A 4" silicon wafer was coated with a thin aluminum oxide film (Al_2O_3, > 30 [nm]) using e-beam evaporation primarily to act as a barrier to subsequent reactions between the iron layer and the underlying silicon substrate.[33] Photoresist (AZ 2020 and AZ 3312 for negative and positive masks, respectively) was spun on at 2750 [rpm] for 60 [sec] and soft baked at 110 [°C] for 60 [sec] for both photoresist types. CNT-MM pore geometry and dimensions were defined on the wafer by photolithography, and hard baked at 110 [°C] for 60 [sec] (Figure 3-1a). The photoresist was developed in a lightly agitated, AZ300MIF solution. A thin iron film (Fe, ~7 [nm]) was thermally evaporated onto the wafer surface as a catalyst for CNT growth (Figure 3-1b). The wafer was sonicated in solvent for > 10 [min], rinsed, and dried with compressed nitrogen (N_2) to remove the entire photoresist layer and portions of the Fe layer in a lift-off process (Figure 3-1c). To protect the wafer during sample dicing, a thin photoresist layer (AZ 3330) was spun on the wafer and soft baked. Samples were then diced using a Disco DAD-320 dicing saw. Immediately prior to CNT growth, diced samples with patterned Fe were solvent cleaned to remove the protective photoresist layer.

After a quality inspection check with an optical microscope, diced samples were placed on a quartz boat in a Lindberg/Blue M Tube Furnace for CNT growth. CNTs were grown for 26 [min] in flowing hydrogen (H_2, ~216 [sccm]) and ethylene (C_2H_4, ~280 [sccm]) at 750 [°C] (Figure 3-1d). This resulted in CNT-MM heights of approximately 600-900 [μm], depending on the sample pattern and Fe layer thickness, and resulting in channel aspect ratios of up to 225:1. CNT-MMs were then coated with carbon in a subsequent infiltration step at 900 [°C] for 20 [min] with similar gases and flowrates as those used during CNT growth (H_2 at ~200 [sccm] and C_2H_4 at ~280 [sccm]; Figure 3-1e). This resulted in carbon-infiltrated CNTs with diameters of approximately 150 [nm]. During carbon infiltration, the CNT-MM structure self-released from the wafer substrate. CNT-MMs were exposed to a brief 7 [min] O_2 plasma etching at 300 [W] using an Anelva Reactive Ion Etcher (RIE), DEM-451 to remove the carbon floor (additional carbon blocking the base of the CNT-MM channels; 5 [min] etch for removal of carbon floor layer; 2 [min] etch for opposite face; Figure 3-1f). The RIE process also serves to enhance the hydrophilicity of the CNT-MMs which, in turn, improves subsequent deposition of Pt catalyst.[10,59] Effects of O_2 etching are discussed in greater detail in section 3.2.2. Standard procedures for each of the above described fabrication processes can be found in Appendix B.

3.1.3 Methods: Integration of Pt Urchin Catalyst (Pt-CNT-MM)

Following an approach similar to those available in the literature,[49,50,52] highly catalytic urchin-like Pt nanoparticles were deposited onto the CNT-MMs. The ability to deposit Pt deep within the CNT microchannels was also confirmed. This electroless deposition involves CNT-MM submersion in a static solution of low pH (< 2.5) and high Pt molarity ($H_2PtCl_6 \cdot (H_2O)_6$ at ~10 [mM]) for each deposition.

Deposition of Pt onto the CNT-MMs was performed on a per-mass basis to maintain a 25-30% [w/w] Pt-C solution loading. For a CNT-MM with a mass of 0.1071 [g], 122.8 [mg] chloroplatinic acid hexahydrate was weighed out (37.5% Pt, Sigma Aldrich 206083) and mixed with 2.0 [mL] formic acid (88% HCOOH, Macron 2592-05) and 18.0 [mL] of either deionized or ultrapure H_2O. These chemicals were added to a 50 [mL] glass beaker (VWR, 89000-198) whereupon their pH level was measured. The pH for this deposition was 1.16, enabling urchin-like nanoparticle growth. Using a slotted Teflon ring for a sample stand, the CNT-MM was positioned vertically in the Pt acid solution. Keeping the sample oriented in this manner ensured that the Pt nanoparticles would nucleate and grow on the carbon substrate rather than precipitating out of solution and simply collecting on the sample face (Figure 3-2). For a CNT-MM mass of 0.1071 [g], the solution molarity (11.80 [mM]) corresponded to a 30.07% [w/w] Pt-C loading. The beaker was then covered by Parafilm® and left until the deposition process was complete, indicated by solution color change from amber to clear. Upon removal from the beaker and prior to subsequent testing, the sample was submerged in deionized water for at least 5 [min] and then placed in an Ultra-Clean 100 (3497M-3) dehydration bake oven for a minimum of 8 [min] (Appendix B.13).

All depositions performed in this work follow that of the static deposition scheme described above. It should be noted that enforcing a convective deposition environment could potentially improve Pt utilization and penetration. Future work would include investigating the effect of electroless Pt deposition in stirred and through-flow environments.

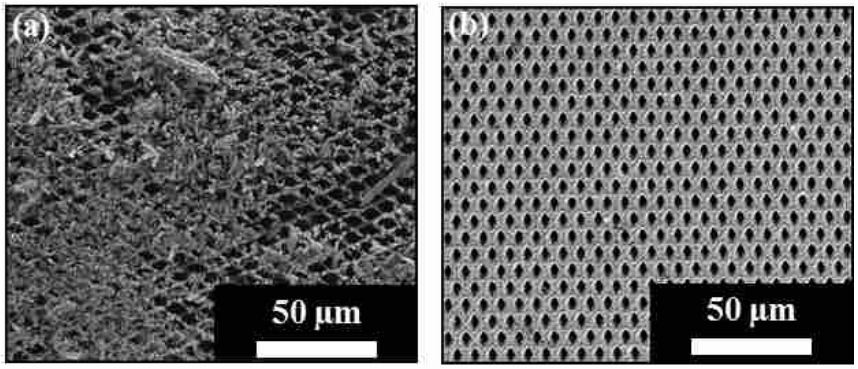

Figure 3-2: CNT-MM orientation dependent Pt deposition. Crystalline Pt deposited onto top surface of CNT-MM sample **(a)** when deposited while resting on bottom of beaker. Uniform Pt deposited onto top surface of CNT-MM sample **(b)** when deposited while oriented vertically in solution.

3.2 Characterization of CNT-MM and Pt-CNT-MM Samples

Preliminary to Pt deposition, the Brunauer-Emmett-Teller (BET) surface area of O_2 etched CNT-MM samples were measured using nitrogen adsorption methods. Additionally, water contact angle measurements were taken to determine the hydrophobicity of the CNT-MM structures. Following Pt deposition, surface areas and water contact angles were measured in a like manner for Pt-CNT-MM samples. Pt-CNT-MMs were further inspected and characterized using both SEM and TEM methods which revealed Pt penetration throughout the CNT microchannels. Unless stated otherwise, all characterization methods presented throughout this manuscript involved CNT-MM/Pt-CNT-MM samples fabricated according to the diamond pattern (4 [µm] hydraulic diameter) described previously in section 3.1.1.

3.2.1 Surface Area Analysis

A micromeritics ASAP 2010 system was used to characterize the surface area of the O_2 etched CNT-MM samples (analysis details, along with characterization of Pt-CNT-MM samples,

are found in Appendix C). It was determined that the CNT-MM samples exhibited a type II nitrogen adsorption isotherm indicative of a macroporous material, with an average calculated BET surface area of 61 [m^2 g^{-1}] and a pore volume of 0.118 [cm^3 g^{-1}] (Appendix C.2). Table 1 shows the average calculated BET surface area for CNT-MM samples with comparison to related structures. Most notably, the BET surface area for the CNT-MMs is approximately half that of pristine CNTs. This is likely attributable to the carbon-infiltration step of the CNT-M fabrication process, which not only contributes additional mass throughout the structure, but may also cause a reduction in surface area by joining adjacent CNTs. However, the infiltration procedure allows for controllable porosity and improved structural integrity.

Table 1: Comparative BET surface area values.

Structure	BET Surface Area [m^2 g^{-1}]	Reference
Pristine CNTs	131	[60]
Polycarbonate Monolith	69	[61]
CNT-MM	**61**	**This Work**
Polyacrylonitrile Membrane	39	[62]
Zirconia Microtube	23	[63]

From the BET surface area analysis it is observed that for an O_2 etched CNT-MM sample, having frontal dimensions of 16.933 [mm] x 16.933 [mm] (grown 600 [μm] thick), there is approximately 6.3 [m^2] of carbon based surface area (assuming a typical sample mass of 0.1032 [g]). This provides a surface area that is roughly twenty thousand times that offered by a planar carbon structure of the same frontal dimensions, while maintaining a very small volumetric footprint. The high surface area CNT-MM microstructures can then be deposited with Pt catalyst, allowing for enhanced mass transport for rate-limited chemical reactions.

3.2.2 Hydrophobicity of Pt-CNT-MMs

Due to their high surface energy and micro/nanoscale surface roughness, the CNT-MM structures were natively hydrophobic.[64] Hydrophilic enhancement of CNTs facilitates intimate contact between aqueous reagents and catalyst, thereby leading to improved chemical reaction rates. In order to provide hydrophilic enhancement without jeopardizing the structural integrity of the Pt-CNT-MM, a controllable hydrophilic enhancement scheme was sought, suitable to CNT structures.

Studies have shown that the hydrophobic disposition of CNT substrates can be altered by ultraviolet assisted ozone treatment,[65] RIE,[66,67] chemical oxidation and subsequent functionalization,[68] chemical etching,[69,70] and by patterning the CNTs to form macroscale hydrophobic topologies.[64,71] Among these, O_2 RIE was deemed most favorable as it allows for a controllable means of modifying the CNT surfaces to be hydrophilic.[10,67] Accordingly, each CNT-MM was exposed to a brief O_2 etch after growth to improve the penetration of aqueous solution into the CNT-MM pores during Pt deposition and other related applications.

A study of the hydrophobic nature of the CNT-MMs was conducted during each stage of the fabrication process. Ultrapure water droplets (10 [μL]) were dispersed onto separate regions across the surface of a CNT-MM sample before O_2 etching. The water droplets did not appear to wet the CNT-MM channels at any appreciable rate indicating that the surface appeared to be hydrophobic (Figure 3-3a). This observation was confirmed as the wetting angle of each droplet was measured using a Ramé-Hart precision contact angle goniometer, and was found to have an average value of 110.6° with a standard deviation of 2.1° (*i.e.* 110.6 ± 2.1°). This angle is indicative of a hydrophobic surface,[72] but is lower than the reported water contact angles for CNTs

given in related studies.[64,67,68] This discrepancy is likely caused by the smooth graphitic/amorphous carbon coating on the outer walls and caps of the CNTs.

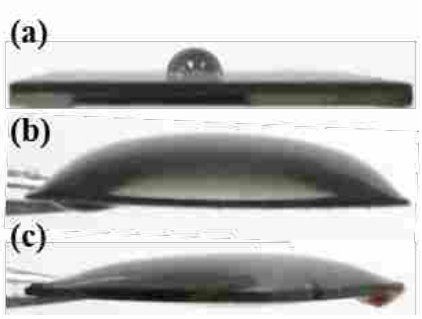

Figure 3-3: Images of ultrapure water droplet(s) on a CNT-MM at various stages of fabrication (all images taken at same magnification). Water droplet **(a)** on a CNT-MM before O_2 RIE, showing hydrophobic nature of CNTs; **(b)** wicking through and dispensing on top of an O_2 RIE etched CNT-MM, showing a hydrophilic nature; and **(c)** wicking through and dispensing on top of a Pt-CNT-MM, exhibiting hydrophilic response as observed for **(b)**.

Hydrophobicity tests for post O_2 etched CNT-MM samples revealed hydrophilic behavior as water was observed to spread along the top surface of the membrane and then wick through to the bottom surface of the membrane (Figure 3-3b); similar hydrophilic behavior was exhibited by the Pt-CNT-MM samples (Figure 3-3c). If the channel sidewalls were hydrophobic at these stages, aqueous solution would not fill a small channel of this diameter. As a result of the spreading and capillary action, no contact angles are reported for either the O_2 etched CNT-MM samples or Pt-CNT-MM samples. These wetting observations support the additional aqueous-based characterization and applications discussed later, where analyte must effectively penetrate the pores of the Pt-CNT-MM samples.

3.2.3 SEM Imaging

Pt nanoparticle morphology and density on the Pt-CNT-MM samples was verified by SEM. Imaging the nanoparticles, using SEM, revealed that the entry region sidewalls of a diamond

patterned Pt-CNT-MM were uniformly covered with dense urchin-like Pt clusters (Figure 3-4a), with a morphology that resembles those produced in 60% [w/w] Pt-C solution and 2.5 pH loadings by Meng *et al*.[49] Around these entry regions, Pt clusters were observed to protrude from the sidewall into the microchannel by as much as 400 [nm]. The apparent roughness that these clusters, and their urchin-like structure, add to the microchannels will serve to facilitate additional analyte/catalyst interaction.

Inspection of Figure 3-4, b-c taken at successively longer distances (approximately 25 and 280 [μm], respectively) into the CNT-MM microchannel, also revealed a uniform deposition of Pt catalyst at a lower coverage density with Pt needle extensions of approximately 120 [nm] and 13 [nm], respectively. Hence, the size of urchin-like Pt nanowires near the midpoint of each microchannel is considerably smaller than their entry-region counterparts. Nevertheless, evidence of Pt coverage in the axial center of the channel indicates that static Pt deposition is indeed capable of reaching even the most inward portions of the CNT microchannels. Furthermore, SEM imaging of a peripheral region of the Pt-CNT-MMs shows the high affinity of Pt precursor to the O_2 etched CNT-MM structure (Figure 3-4d). Comparison of the lightly coated inner regions of the Pt-CNT-MM against the densely coated peripheral regions suggest that exposure to the bulk Pt solution enhances Pt coverage, and thus the deposition process is likely diffusion-limited near the axial center of the channel. Possible future work would include convection-enhanced Pt deposition (stirred or through-flow depositions) to facilitate greater Pt coverage throughout the entirety of the CNT-MM microstructure. In this way, more of the available carbon based surface area can be utilized for catalytic applications.

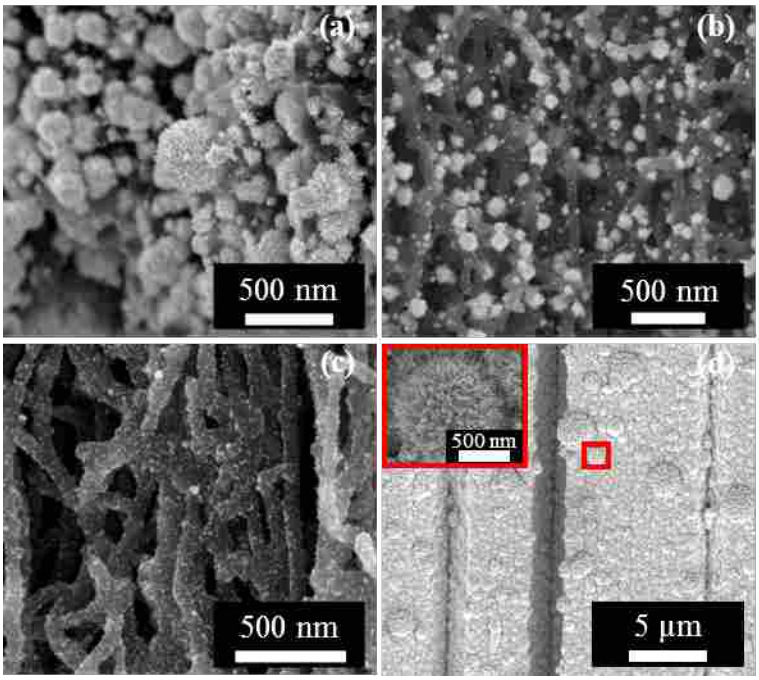

Figure 3-4: Sample SEM images of fabricated Pt-CNT-MMs (diamond pattern). Pt nanoparticle morphology at **(a)** the microchannel entrance of Pt-CNT-MM, **(b)** approximately 25 [µm] into the microchannel, **(c)** and at the axial center (~280 [µm]; half the thickness of the CNT-MM sample) of the microchannel. **(d)** Total coverage along the periphery of the Pt-CNT-MM with inset showing the urchin-like morphology and arrangement of the deposited Pt.

Having confirmed the morphology and penetration of the Pt catalyst on the CNT-MM microstructure, additional lithography masks were designed and produced for the investigation of Pt-CNT-MMs with different pore geometries and hydraulic diameters. As mentioned previously, small and large circle patterns were produced, having microchannel diameters of 4.0 and 16.1 [µm] respectively. Pt deposition, as described above, was conducted and imaged using SEM as for the diamond patterned Pt-CNT-MMs.

An SEM Pt penetration analysis is shown in Figure 3-5 where it can be seen that all samples revealed Pt coverage throughout the entire length of their respective microchannels. Again, evidence of Pt coverage in the axial center of the channel indicates that static Pt deposition is indeed capable of reaching even the furthest interior portions of the CNT microchannels.

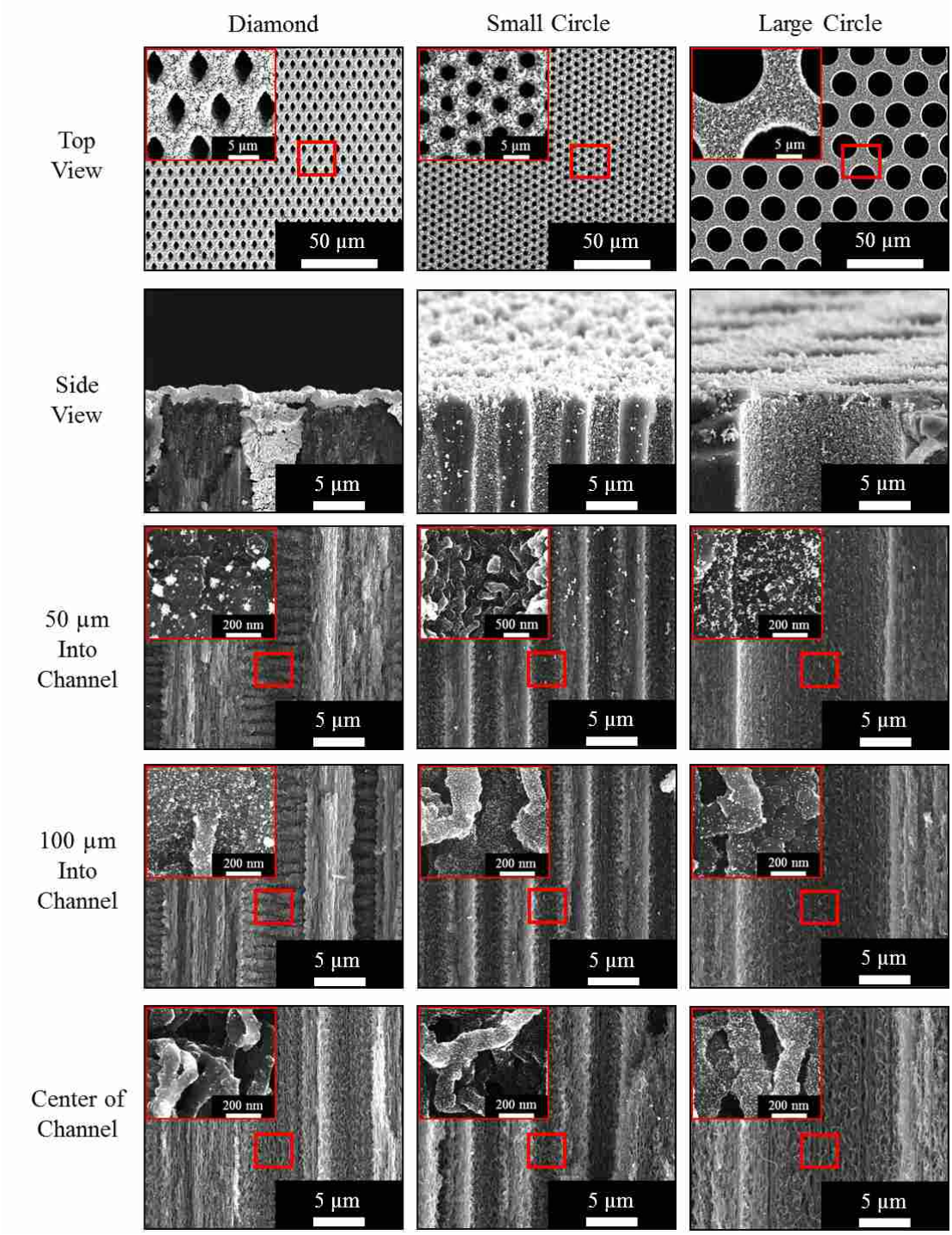

Figure 3-5: SEM Pt penetration analysis. Pt-CNT-MM samples made from the diamond, small circle, and large circle patterns and deposited in ~30% [w/w] Pt-C solutions all reveal Pt coverage throughout the entire length of their respective microchannels. Depths to "Center of Channel" for the diamond, small circle, and large circle samples are 475, 220, and 264 [µm], respectively. Also, it should be noted that successive images for a given pattern are not necessarily taken from the same sample, or same microchannel for a given sample.

3.2.4 TEM Imaging

High-resolution TEM was used to confirm the deposition of Pt nanoparticles onto CNTs, as well as further characterize the dimensions of the Pt nanowires. Characterizing the Pt-CNT-MM by TEM reveals a d-spacing between (111) planes of 0.23 [nm], confirming that the deposited nanoparticles are Pt (Figure 3-6, a-b).[50,57,73,74] TEM analysis further confirms that the larger Pt urchins have nanowires with lengths of up to 30 nm, which are comparable to lengths reported by Sun *et al.*, and three times longer than those reported by Meng *et al.* on carbon nanotubes and carbon powder respectively.[49,52]

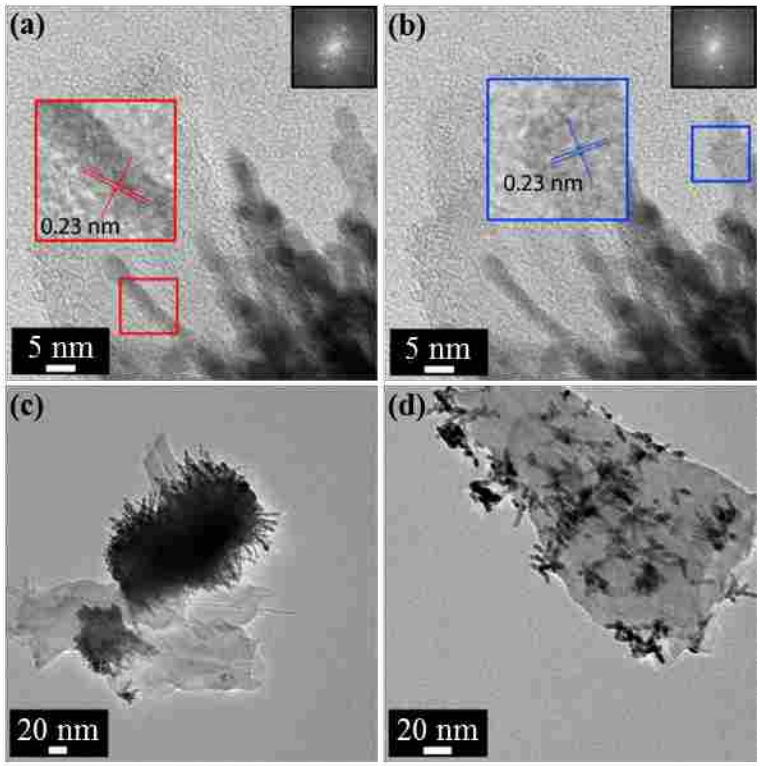

Figure 3-6: TEM images of Pt-CNT-MM sample. **(a)** TEM image showing lattice spacing of a synthesized Pt nanowire with Fast Fourier Transform (FFT) inset. **(b)** Same TEM image showing the lattice spacing of the Pt nanowire on the same cluster but having different crystal plane orientation with FFT inset. **(c)** Fragment having dense Pt cluster coverage and large growth size, similar to the entrance region of Pt-CNT-MM microchannels. **(d)** Fragment having less dense urchin-like Pt cluster coverage and smaller growth size, similar to the central interior of Pt-CNT-MM.

Morphologies of the type illustrated in Figure 3-6c dominate the *entry regions* of the Pt-CNT-MM microchannels whereas smaller clusters, as illustrated in Figure 3-6d, fill the central interior. It is also seen that urchin-like Pt nanowires in the *central interior* are approximately half this maximum length, or approximately 15 [nm]. Pt nanowire diameters measured in both of the aforementioned studies, however, coincide with the 3 [nm] dimension typically observed here. It is also interesting to note that while average Pt nanowire dimensions (length and diameter) are consistent between clusters at comparable regions along the Pt-CNT-MM channels, the orientation of their (111) planes vary drastically between nanowires, regardless of region and cluster.

3.3 Conclusions

CNT-M techniques were used to fabricate carbon-infiltrated multi-walled CNT scaffolds composed of highly ordered and aligned microchannels with a desired geometry. The O_2 etched CNT-MM microstructure BET surface area was characterized using nitrogen adsorption methods and was found to be 61 [$m^2\ g^{-1}$], affording large surface area for catalyst functionalization while minimizing volumetric footprint. Furthermore, urchin-like Pt nanoparticles were deposited onto, and throughout, the entirety of the CNT-MMs. While many publications report Pt nanoparticle deposition onto carbon structures, this work is the first to demonstrate Pt nanoparticle deposition onto carbon-infiltrated MWCNTs. Additionally, this work reports the successful union between CNT-templated microfabrication and chemical deposition of nanoparticles. Such an electroless deposition technique is capable of depositing nanoparticles > 200 [μm] deep within the pores of the CNT microchannels, reaching even the furthest interior portions of the CNT-MM microstructure. When exposed to water, the Pt-CNT-MMs displayed hydrophilic response – wicking the water into the microchannels, thereby providing high aspect ratio, hydrophilic, catalytic microstructures for transport enhancement of rate-limited chemical reactions.

Depleting coverage density, toward the axial center of the CNT-MM microchannels, suggests that the Pt deposition process is diffusion limited. Enforcing a convective deposition environment could potentially improve Pt utilization and penetration throughout the CNT-MM microchannels. Accordingly, future work will include investigating the effects of electroless Pt deposition in stirred and through-flow environments to achieve better coverage of the large surface area afforded by the CNT-MM microstructure. Additional future work may also include varying microchannel geometry, sample thickness, and porosity. These variations can then be monitored as the Pt-CNT-MM samples are demonstrated in other chemical sample systems.

CHAPTER 4. UNDERWATER PROPULSION *VIA* H_2O_2 DECOMPOSITION

4.1 Introduction

An upward trend in the research and use of unmanned underwater vehicles (UUVs), and in particular micro underwater vehicles (MUVs, small UUVS between 1-50 [cm] in length), for exploration of confined spaces such as ship wrecks, submerged oil pipeline, and various military purposes has been observed over recent years.[75-77] The locomotion of these vehicles is typically controlled by propeller-based systems, which are often used for long-endurance missions.[78-80] However, propeller-based systems are usually limited in their ability to perform tight radius turns, burst-driven docking maneuvers, and low-speed course corrections.[57,76] These motions often require energy-dense fuels, which can be quickly and efficiently utilized to provide sudden bursts of propulsion. Such energy-dense fuels/reagents include H_2O_2,[81] methanol,[82] and carbohydrates,[83] all of which have been the focus of many recent fuel-catalyst reaction studies.

The decomposition of H_2O_2 as a means for locomotion in micro-scale applications is of particular interest because of its scalability, as well as possessing a large power density (up to 45 times that of Ni-Cd batteries in MUVs).[84] In addition, H_2O_2 is an environmentally friendly fuel, expending only 'green' by-products (*i.e.* oxygen, or O_2, and water) during decomposition.[57] Specifically, when exposed to a metal catalyst such as platinum (Pt), H_2O_2 is broken down in an exothermic reaction into O_2 and water, which provides thrust through the significant volumetric change relative to the liquid fuel.

Many micro/nanoscale structures have been fabricated to utilize the decomposition of H_2O_2 by Pt for propulsion, including janus motors,[6,85,86] conical-shaped bubble thrusters,[7,87-89] and catalytic nano/micromotors.[3,5,90] In other examples, structures resembling a parallel arrangement of microtubular bubble thrusters[2,91] has also been investigated to achieve design requirements of high aspect ratio and small volumetric profile.

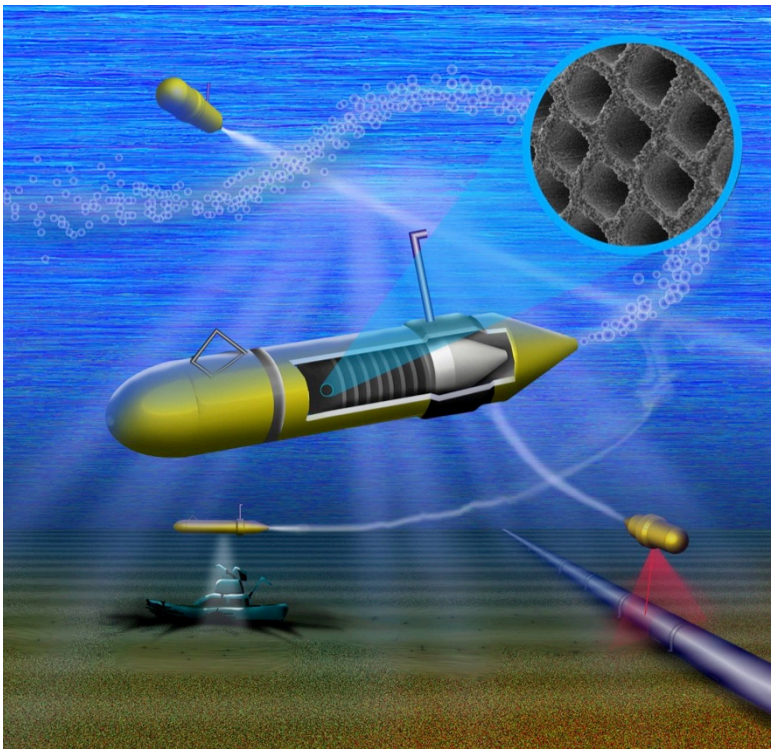

Figure 4-1: Envisioned propulsion of MUV *via* Pt-CNT-MMs and H_2O_2 decomposition. Graphic courtesy of Robert Gates.

Each of these structures rely on transport-enhancing mechanisms to decompose H_2O_2 fuel. Transport enhancement afforded by the use of the CNT-MM catalytic platforms is herein demonstrated, allowing for underwater burst-propulsion of MUVs and their associated payloads. Thrust required for these applications is provided by achieving enhanced fuel decomposition *via* increased fuel flowrate, increased catalytic surface area, and increased boundary layer confinement. This study investigates the efficacy of employing Pt-CNT-MM microstructures for

underwater propulsion, which utilize all three transport enhancement methods (Figure 4-1). All samples used in this study were fabricated using the diamond pattern.

4.2 Results and Discussion

Enhanced H_2O_2 fuel decomposition for underwater propulsion of MUVs was demonstrated using Pt-CNT-MM samples fabricated according to the techniques presented in 0Catalytic performance of the Pt-CNT-MM samples toward the decomposition of H_2O_2 can be measured by conducting activation energy tests. These tests, along with thrust measurements using a water tank setup, are used to demonstrate the efficacy of CNT-MM catalytic platforms for transport enhancement of a rate-limited chemical reaction – H_2O_2 decomposition by catalysis for underwater propulsion of MUVs.

4.2.1 Hydrogen Peroxide Decomposition

The effectiveness and durability of catalysts for H_2O_2 decomposition is dependent upon multiple factors including material composition, surface area, and reaction temperature. Namely, catalytic performance is defined by its ability to reduce the activation energy required for a given chemical reaction. A variety of catalysts have been developed for lowering the activation energy associated with H_2O_2 decomposition including metal catalysts[92,93] (e.g., Pt, Pd, Au and Ag) as well as metal oxide catalysts[94-96] (e.g., MnO_2, Fe_2O_3, $K_2Cr_2O_7$). Although highly effective at lowering the activation energy of H_2O_2 decomposition, metal oxide catalysts are consumed during H_2O_2 decomposition and therefore would not be able to provide recurring thrust for MUV propulsion. Thus, metal catalysts were chosen for this work. The effectiveness of metal catalysts for H_2O_2 decomposition is proportional to the exposed catalyst surface area. In the case of Pt catalysts, more exposed metal correlates to more free catalytic sites available for Pt-(OH) and Pt-(H) binding—

two reactions that are involved in the eight kinetic steps in H_2O_2 decomposition with Pt metal catalysts.[97] Furthermore, the reaction rate for the decomposition of H_2O_2 tends to dramatically increase as the temperature of the exothermic reaction increases. This phenomenon is due to the auto decomposition of H_2O_2 at elevated temperatures and to the fact that oxygen solubility remains low even at higher temperatures.[98] Hence the reaction rates of H_2O_2 decomposition tend to increase due to the conflation of both increased surface area and reaction temperature.

Transport processes may also alter the performance of the Pt-CNT-MM catalysts, including the following: transport of reactants from the main fuel stream to the Pt-CNT-MM surface; transport of reactants within the CNT microchannels to the Pt metal surface; adsorption/desorption of reactants/products at the Pt metal surface; transport of desorbed products from the Pt metal through the CNT microchannels; and transport of desorbed products from within the CNT microchannels to the main stream of fluid.[99] Consequently, the activation energy can change according to the rate of flow introduced into the reaction chamber. Therefore, an "effective activation energy" of the Pt-CNT-MM is reported, as measured within a convective fuel flow field to mimic, in part, the convective flow field that would be experienced in an actual MUV reaction chamber. Many researchers have not considered the impact of convection on activation energy and often the conditions of fluid stirring are not provided though present during testing. The activation energy provided by others under flowing conditions is equivalent to the effective activation energy defined here, though specific to the conditions of the flow field.

The effective activation energy (E_a) required for H_2O_2 decomposition by the micro/nanostructured Pt-CNT-MMs was empirically determined. It is noted here that the effective activation energy of Pt-CNT-MMs with respect to alternate chemical reactions (such as the *oxidation* of H_2O_2 for chemical sensing) may also be determined. However, our current work

investigates the effective activation energy of Pt-CNT-MMs for H_2O_2 decomposition *via* catalysis only (*i.e.* chemical reaction for propulsion applications), but future work may include activation energy testing with respect to alternate chemical reactions.

H_2O_2 decomposition testing was performed on three replicate Pt-CNT-MM samples (referred to as Samples A, B, and C), each being fabricated as described in the Methods section. Each sample was exposed to 1% [w/w] H_2O_2 solution at three different temperatures (0 [ºC], 17.5 [ºC] and 35 [ºC]) in a test flask while the differential pressure (Appendix D.1), resulting from O_2 generation during decomposition of H_2O_2, was monitored (eq 1).

$$2H_2O_2 \rightarrow 2H_2O(g) + O_2(g) \quad (1)$$

The measured differential pressure generated by the reaction products (taken as the average of two or more test runs per sample) was plotted for comparison against two distinct control samples, both tested at 35 [ºC] (Figure 4-2a). These control samples (referred to as 'Samples D and E') were fabricated following the same procedure as for Samples A, B, and C, but received no Pt deposition. As can be seen, Samples A, B, and C generate significantly more pressure than Samples D and E, despite being tested at a lower (less favorable) temperature. Furthermore, negligible pressure rise was observed for the uncoated samples, demonstrating that catalytic performance of Pt-CNT-MMs toward H_2O_2 is strongly dependent on the presence of Pt nano-urchins deposited onto the multi-walled carbon nanotube (MWCNT) microstructure.

Differential pressure data shown in Figure 4-2a, for Samples A, B, and C, were used in conjunction with the ideal gas law ($PV = nRT$), to determine the number of moles of O_2 released during the reaction (n), where P is the measured differential pressure [kPa], V is the volume of the flask (125 [mL]) R is the ideal gas constant (8.314 [J mol^{-1} K^{-1}]), and T is the bath temperature for the flasks [K]. Using this data, in accordance with stoichiometry associated with eq 2, the quantity

of H_2O_2 decomposed by the catalyst was determined. The reaction rate constant for the decomposition of H_2O_2 can be determined by the following first-order reaction equation[100]

$$ln\left(\frac{[H_2O_2]}{[H_2O_2]_o}\right) = -k_{obs}t \quad (2)$$

where $[H_2O_2]$ is the quantity of H_2O_2 remaining in solution at time t, $[H_2O_2]_o$ is the initial quantity of H_2O_2 in solution, k_{obs} is the reaction rate constant [s^{-1}] over time. Figure 4-2b illustrates the ratio of the remaining fuel to the initial quantity of fuel (10 [mL] of 1% [w/w] H_2O_2 solution), used to determine the reaction rate constant for the data in Figure 4-2a according to eq 2. To avoid inclusion of initial noise/outliers in the pressure data, measurements taken between 60 and 120 [s] were used for all calculations of k_{obs}. Additional testing of Sample A under three different temperatures (0 [ºC], 17.5 [ºC] and 35 [ºC]) illustrated higher observed decomposition rates with increasing temperature (Figure 4-2, c-d).

The natural log of the Arrhenius Equation (eq 3) with the calculated observed reaction rate constants are used to calculate the effective activation energy.

$$ln(k_{obs}) = -\frac{E_a}{R}\frac{1}{T} + ln(A) \quad (3)$$

Here, E_a is the effective activation energy of the catalyst [J mol^{-1}], and A is the pre-exponential factor [s^{-1}]. By plotting the natural log of the observed reaction rate constant for each test run as a function of inverse temperature for Sample A, the activation energy (26.96 [kJ mol^{-1}]) was acquired from the slope of the linear fit of the data (Figure 4-2e). Error associated with the activation energy value is bounded by the upper and lower limits of 33.70 and 20.12 [kJ mol^{-1}], respectively, calculated using the slopes of the extreme cases presented in Figure 4-2e.

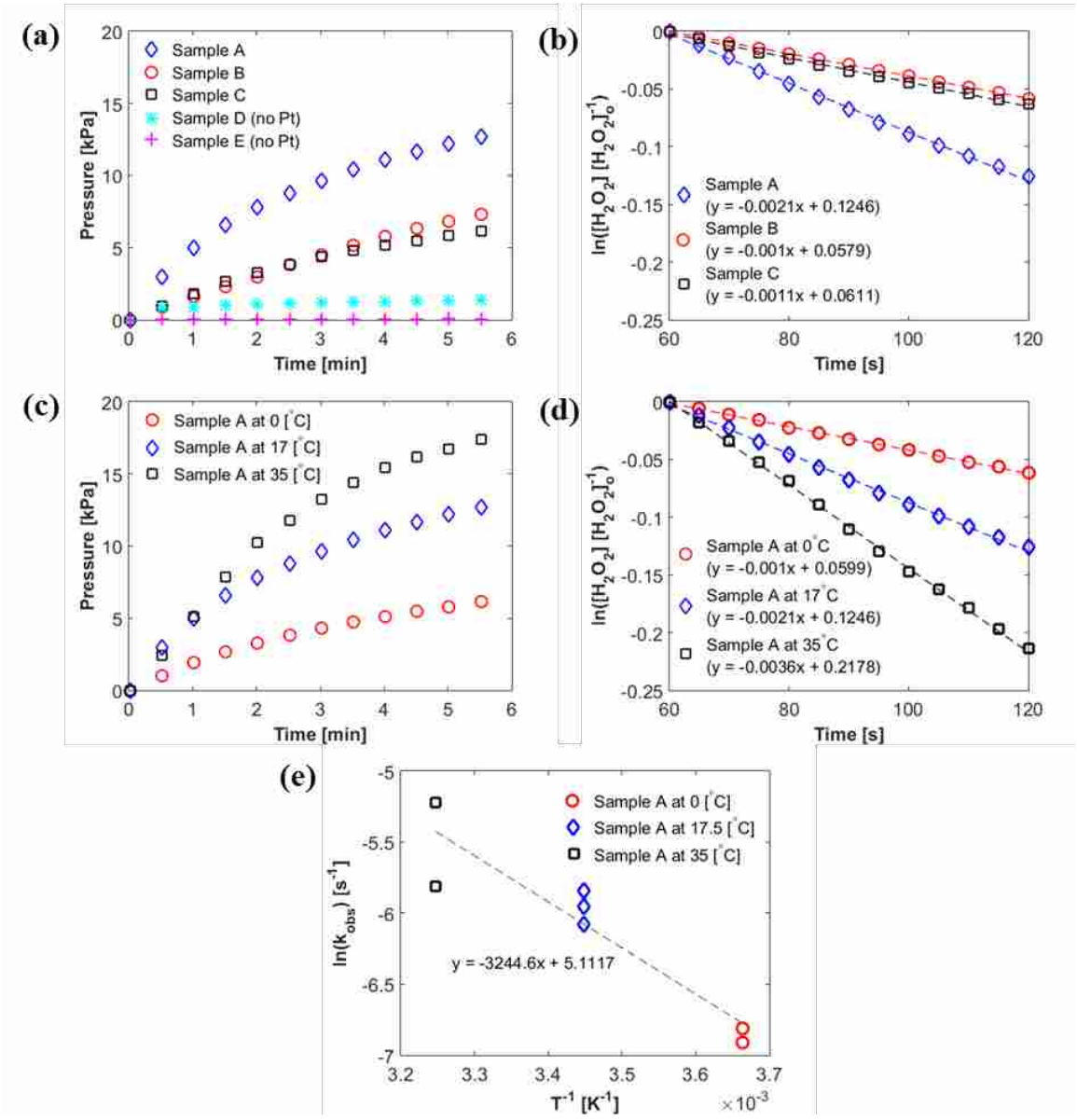

Figure 4-2: Effective activation energy data for CNT-MM and Pt-CNT-MM samples. **(a)** Measured differential pressure *vs.* time data taken as the average of two or more test runs per sample at 17.5 [°C] for Pt-CNT-MM Samples A, B, and C, as well as for CNT-MM Samples D and E at 35 [°C]; data recorded at 1 [Hz], sample data shown at 0.033 [Hz]. **(b)** Reaction rate plots calculated according to eq 3, using data from **(a)** and shown at 0.2 [Hz]. **(c)** Measured differential pressure *vs.* time data taken as the average of two or more test runs for Sample A, performed at three temperatures (0 [°C], 17.5 [°C] and 35 [°C]); data recorded at 1 [Hz], sample data shown at 0.033 [Hz]. **(d)** Reaction rate plots calculated according to eq 3, using data from **(c)** and shown at 0.2 [Hz]. **(e)** Plot of the natural log of the Arrhenius Equation for Sample A (for each individual test run) with slope used to determine effective activation energy. Dashed lines represent linear curve fits of the data, with equations provided for figures **(b)**, **(d)** and **(e)**. Goodness of fit values for **(b)** and **(d)** are $R^2 > 0.996$ and for **(e)** is $R^2 = 0.867$.

Table 2, provides an overview of the calculated decomposition kinetics for a Pt-CNT-MM (Sample A), including the entropy of activation, ΔS ([J mol^{-1} K^{-1}]; where $\Delta S = R \cdot \ln(A)$). This reported effective activation energy of 26.96 [kJ mol^{-1}] seems to improve upon similar nanostructured surfaces such as those comprised of graphene (28.8 [kJ mol^{-1}])[101] and Pt/palladium nanoparticles on Nafion (34.0-36.3 [kJ mol^{-1}]).[98] Furthermore, the effective activation energy is lower than our previous Pt-paper catalyst (29.5 [kJ mol^{-1}])[57] where similar Pt nano-urchins were deposited on cellulose sheets – such improvement is most likely due to the higher surface area achieved by the three dimensional architecture created by the CNT microchannels of the CNT-MM as opposed to the planar structure of the cellulose sheets. These reported activation energies are among the lowest found in the literature, confirming that the Pt-CNT-MM catalyst is highly efficient for the decomposition of H_2O_2.

Table 2: Average H_2O_2 decomposition kinetics for the Pt-CNT-MMs. Range of possible values and one standard deviation shown in parenthesis for E_a and ΔS, respectively.

Temperature [°C]	k_{obs} [s^{-1} x 10^{-3}]	E_a [kJ mol^{-1}]	A [s^{-1}]	ΔS [J mol^{-1} K^{-1}]
0	1.0 ± 0.1	26.96 (33.70 < E_a < 20.12)	165.84	42.47 (±34.36)
17.5	2.1 ± 0.3			
35	3.6 ± 1.7			

4.2.2 MUV Platform and Propulsion Testing

An MUV test submersible was created in order to test the capability of the developed Pt-CNT-MMs to produce thrust *via* H_2O_2 decomposition. The developed MUV test submersible, fabricated *via* a 3D printer (Appendix D.2), is capable of housing eight inline Pt-CNT-MM samples (each with a square planar surface area of 2.867 [cm^2]; Figure 4-3a). Measurement of the propulsive thrust generated by the decomposition of H_2O_2 by Pt-CNT-MMs housed within the test submersible was performed by attaching a strain gauge to the mounting rod holding the test

submersible. Syringe-fed tubing was secured to the inlet port of the test submersible for the supply of H_2O_2 fuel, and the assembly was then lowered into a water tank for testing (Figure 4-3b).

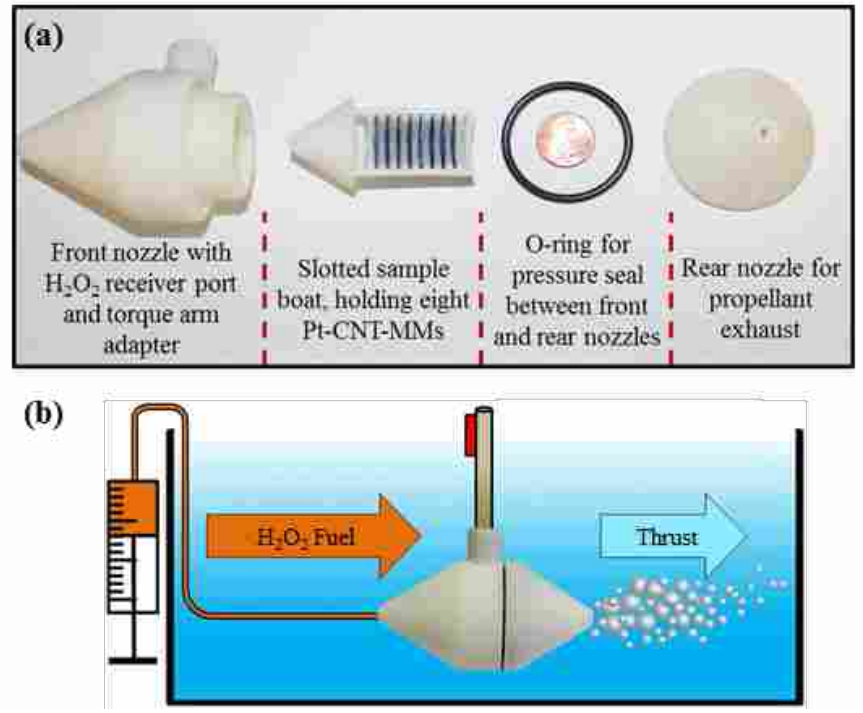

Figure 4-3: Test submersible assembly and water tank setup for thrust measurement. **(a)** Optical image displaying disassembled test submersible with corresponding descriptions and **(b)** schematic illustrating assembled test submersible and water tank setup.

Heterogeneous catalytic reactions are heavily dependent on the mass transport of reactant (fuel) to the catalytic surface.[102] Thrust generated *via* decomposition of H_2O_2 fuel is therefore dependent on the introduction rate of the fuel to the Pt-CNT-MM surface. As mentioned previously, this introduction rate can be enhanced in three ways – by increasing the available catalytic surface area, increasing the fuel flowrate (or, synonymously, the fuel concentration), and employing boundary layer enhancement. While enhancement by boundary layer confinement will be relatively intrinsic in these studies, the former two enhancement methods can be easily studied through a series of propulsion tests. Accordingly, propulsion testing was performed using three different H_2O_2 concentrations (20, 35, and 50% [w/w]), each at a given average flowrate (10 [mL

s^{-1}]) for one, two, four, six, and eight Pt-CNT-MMs. Also, a manually driven (high burst) flowrate using 50% [w/w] H_2O_2 was conducted for one, four, and eight Pt-CNT-MMs. As a control, water was injected into the submersible reaction chamber, holding eight Pt-CNT-MMs, at the highest flow rate tested (manually driven burst). With no appreciable thrust observed for this water control run, all measured thrust was attributed to the decomposition of H_2O_2. Reported thrust values for each combination of test conditions were taken from the average of two or more tests.

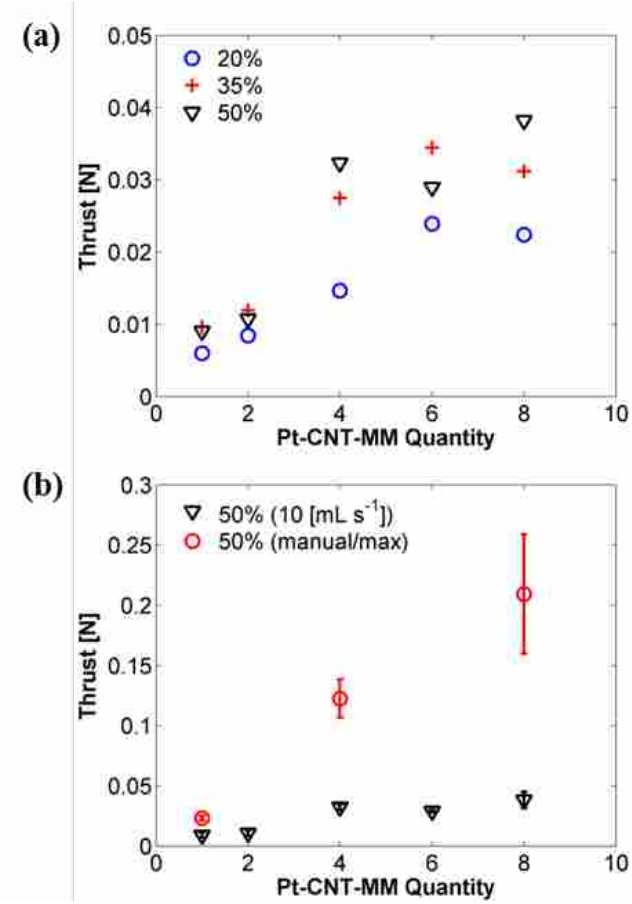

Figure 4-4: Thrust measurement plots for H_2O_2 decomposition-driven propulsion. **(a)** Varying H_2O_2 concentration (20, 35, and 50% [w/w] H_2O_2) per fixed flowrate (10 [mL s^{-1}]); 20 and 35% [w/w] H_2O_2 fuel approaching total decomposition with addition of Pt-CNT-MM samples. **(b)** Fixed H_2O_2 fuel concentration (50% [w/w] H_2O_2) per varied flowrates (10 [mL s^{-1}] and manually driven high burst flow); illustrates thrust generation dependence on H_2O_2 fuel flowrate. Reported thrust values for each combination of test conditions were taken from the average of two or more tests. Error bars indicate the standard deviation among tests for a given test condition.

Measured thrust under the 10 [mL s^{-1}] flow conditions is shown in Figure 4-4a. Comparison of the corresponding 20 and 50% [w/w] H_2O_2 cases demonstrates that an increase in fuel concentration lends to greater generated thrust. Initially, it is also observed that with an increased quantity of Pt-CNT-MMs (increased catalytic surface area), there is a notable increase in measured thrust. For the 20 and 35% [w/w] H_2O_2 test runs, no appreciable thrust is observed by having greater than six Pt-CNT-MMs. This may be due to the H_2O_2 fuel approaching total decomposition within the reaction chamber of the test submersible for these conditions.

Thrust produced at a fixed fuel concentration (50% [w/w] H_2O_2) for varying flowrates is presented in Figure 4-4b. It is shown that both the 10 [mL s^{-1}] and manually driven flowrates exhibit monotonically increasing thrust per additional Pt-CNT-MM, suggesting incomplete fuel decomposition. It is anticipated that higher thrusts would be attained by the addition of more inline Pt-CNT-MM samples until total fuel utilization occurs. Ultimately, for the manually driven flowrate, a maximum average burst thrust of 209 [mN] (with a standard deviation of 49 [mN]; *i.e.* 209 ± 49 [mN]) was achieved using eight Pt-CNT-MMs, which is within the milli-newton thrust range typically required for MUV propulsion.[57,103] It was also observed that, for the same number of Pt-CNT-MM samples and H_2O_2 fuel concentration, the manually driven flowrate produced significantly greater thrust than that for 10 [mL s^{-1}], suggesting a flowrate dependent thrust. The maximum average thrust achieved using Pt-CNT-MMs and 50% [w/w] H_2O_2 is compared below against thrust values reported for several biomimetic propulsion designs (Table 3); thrust produced by the decomposition of H_2O_2 *via* Pt-CNT-MMs in this work is more than six times greater than that produced by several biomimetic propulsion systems.[104-107]

Table 3: Comparative thrust values.

Propulsion System	Thrust [mN]	Reference
H_2O_2 Decomposition *via* Pt-CNT-MMs	**209 ± 49**	**This Work**
Miniature Robotic Fish (Trapezoidal Fin)	~32	[104]
SMA Wires Actuator	27	[107]
Monolithic IPMC Fin	0.4	[106]
IPMC Actuator	0.089	[105]

Application of the Pt-CNT-MM microstructures in a MUV test submersible confirmed that increase of the H_2O_2 fuel introduction rate to the catalyst (*i.e.* increase of H_2O_2 fuel flowrate/concentration and available catalyst surface area) contributes to additional thrust, and that the Pt-CNT-MMs can be used to provide burst propulsion for MUVs. It was further demonstrated that, for a given H_2O_2 fuel concentration and flowrate, total fuel utilization can likely be achieved by addition of Pt-CNT-MM catalysts. Specifically, the effects of boundary layer confinement and catalytic surface area increase with increasing Pt-CNT-MM quantity, ultimately lending to total fuel utilization as was observed for the tests involving a 10 [mL s^{-1}] flowrate of 25 and 35% [w/w] H_2O_2 with six or more Pt-CNT-MMs. Because increasing the Pt-CNT-MM quantity leads to total fuel utilization, it is confirmed that Pt-CNT-MMs enhance fuel decomposition. In addition to catalytic surface area and flowrate, enhancement *via* of boundary layer confinement is addressed more *explicitly* in a second case study of the H_2O_2 sample system – chemical sensing.

4.3 Conclusions

CNT-M techniques were used to fabricate Pt-CNT-MMs to provide high aspect ratio catalytic microstructures for the enhanced propulsion of MUVs. In summary, it has been demonstrated that the Pt-CNT-MM catalyst possesses a low activation energy (26.96 [kJ mol^{-1}]),

thereby achieving high reaction efficiency for the decomposition of H_2O_2. Furthermore, the reported effective activation energy of the Pt-CNT-MM catalyst rivals the lowest reported values in the literature.

The efficacy of Pt-CNT-MMs, functionalized in 25-30% [w/w] Pt-C solution, for the propulsion of MUVs was demonstrated using a water tank setup. Application of the Pt-CNT-MM microstructures in the water tank setup confirmed that increase of the H_2O_2 fuel introduction rate to the catalyst (*i.e.* increase of H_2O_2 fuel flowrate/concentration and available catalyst surface area) contributes to additional thrust, and that the Pt-CNT-MMs can be used to provide burst propulsion for MUVs. Namely, using eight inline Pt-CNT-MMs, exposed to manually driven high burst flows of 50% [w/w] H_2O_2, producing a maximum average burst thrust of 209 ± 49 [mN]. This propulsive bursting thrust falls within the milli-newton thrust range typically required for MUV propulsion,[57,103] and is shown to be at least six times greater than that produced by several biomimetic propulsion designs.[104-107] Further, the proposed approach minimizes component exposure to the environment and is comprised of a simple, static architecture relative to other micro-propulsion systems.

It was further demonstrated that, for a given H_2O_2 fuel concentration and flowrate, total fuel utilization can likely be achieved by addition of Pt-CNT-MM catalysts. Because it is common knowledge that boundary layer confinement provides further enhancement to the introductory rate of analyte to a surface, it is believed that this method contributed to the increase in thrust, in conjunction with the thrust afforded by the increase in H_2O_2 fuel flowrate/concentration and Pt-CNT-MM quantity, thereby successfully demonstrating enhanced fuel decomposition *via* Pt-CNT-MMs.

Future work will be devoted to studying Pt-CNT-MM performance under varying microchannel geometry and porosity. Due to the 'free-standing' nature of the Pt-CNT-MM samples in the MUV reaction chamber, it is likely that the much of the H_2O_2 fuel was not confined to pass through the catalyst microchannels. Additional work, therefore, may also include thrust measurements taken for Pt-CNT-MM samples held in place using pressurized seals (O-rings, *etc*.) such that all H_2O_2 fuel is forced exclusively through the Pt-CNT-MM microchannels. It can be expected that such a setup, for a given number of Pt-CNT-MMs at a prescribed flowrate, would increase the generated thrust per Pt-CNT-MM and induce total fuel utilization earlier than a setup using free-standing Pt-CNT-MM catalysts.

CHAPTER 5. H_2O_2 SENSING FOR GLUCOSE DETECTION APPLICATIONS

5.1 Introduction

Sensor usage has increased dramatically in detection applications due to miniaturization of components through micro- and nano-fabrication. Small-scale fabrication methods have not only reduced the size of sensors, but have also greatly increased production rate as several sensors can be constructed in parallel. However, as sensors have reduced in size, their surface area has also experienced a corresponding decrease, which can have a negative impact on the ability to sense target-molecules (analytes) in suspension rendering some sensors less sensitive.

One application of sensors is found in the monitoring of glucose levels in the body as a mechanism to manage diabetes. Approximately 25.8 million people in the United States have diabetes, or just over 8% of the total population.[108] It is estimated that another 79 million people have prediabetes or impaired glucose tolerance. This metabolic disorder is evidenced in blood glucose concentrations outside of the normal range of 4.4-6.6 [mM].[109] While diabetes can result in or be a contributing factor to fatalities, many more confront the condition on a daily basis as they monitor and control blood glucose levels. This monitoring commonly involves lancing one's fingertips to draw blood for testing. The invasive nature of this test is cited as one contributing factor as to why people with diabetes do not regularly monitor their glucose levels. In recent studies, non-invasive routes to glucose sensing have been investigated that target saliva, sweat, tears, and urine as alternatives to blood.[10,109-111]

Today the preferred approach for glucose sensing is amperometric measurement of H_2O_2 concentration.[112] As glucose is bound to a surface that has been functionalized with the catalyst glucose oxidase (GO_x), it is decomposed into gluconic acid and H_2O_2 (eq 4).[113] The H_2O_2 is subsequently oxidized releasing two electrons per molecule, thereby producing a measureable electric current (eq 5).[10,113]

$$glucose + O_2 \xrightarrow{GO_x} gluconic\ acid + H_2O_2 \quad (4)$$

$$H_2O_2 \xrightarrow{(Electrode)} 2e^- + 2H^+ + O_2 \quad (5)$$

The electric current is directly correlated to the glucose concentration and is limited by the rate of glucose transport to the functionalized sensing surface. Furthermore, electron transfer kinetics highly affect biosensor performance. For this reason, it is desirable for the sensing surface to be composed of highly *electro*catalytic (electrochemically active) materials such as palladium (Pd), nickel (Ni), or platinum (Pt). To facilitate the sensing of current, it is also advantageous that the functionalized supporting structure(s) be a highly conductive material such as carbon.

Given a bias voltage, electrocatalytic materials promote chemical redox reactions within solution. Unlike catalysis, as used in our propulsion work, electrochemical processes investigate the explicit monitoring of electron exchange between electrocatalytic surfaces and molecules during redox reactions. Hence, while our previous work allowed us to demonstrate introduction rate enhancement via Pt-CNT-MMs for the *decomposition* of H_2O_2, electrochemistry allows us to investigate the same for the *oxidation* of H_2O_2. Electrochemistry also allows us to better study the mass transport enhancement involved with using Pt-CNT-MMs, as well as gives us the ability to further characterize the microstructure in terms of electroactive surface area (surface area available for the participation in chemical redox reactions).

Several chemical sensing studies conducted in recent years have demonstrated that CNT based electrodes have shown excellent electrocatalytic activity toward H_2O_2.[1,114] These microscale

structures also satisfy the need for facilitating greater mass transport rates of analyte to a sensing surface because of their high aspect ratio geometry. The utility of CNTs in electrochemical biosensing has been summarized by Rivas *et al*.[114]

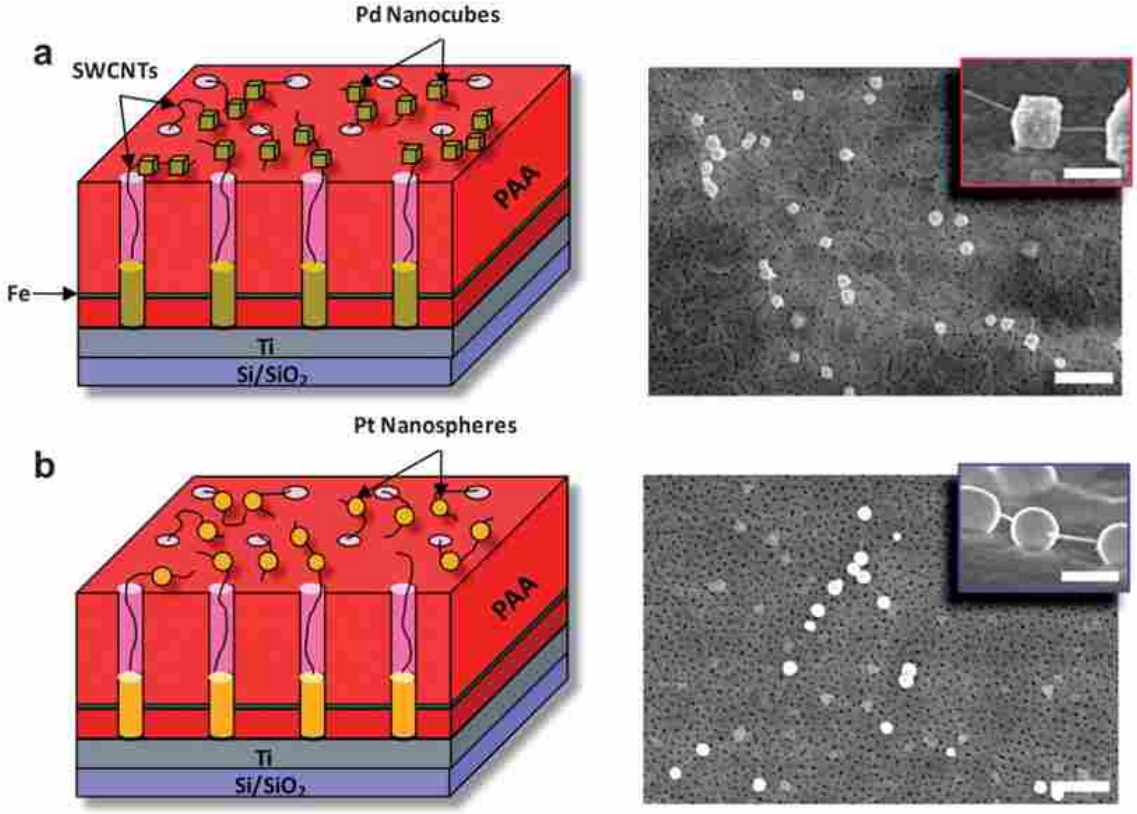

Figure 5-1: Illustrations and accompanying SEM images of **(a)** Pd-SWCNT/PAA and **(b)** Pt-SWCNT/PAA electrodes grown from a PAA templated substrate. These nanostructured sensing platforms can be used for H_2O_2 sensing applications, or be functionalized with GluOx to be used in glucose/H_2O_2 sensing applications (GluOx/Pd-SWCNT/PAA and GluOx/Pt-SWCNT/PAA).[1]

Previous work involving CNTs for glucose sensing includes the attachment of gold-coated palladium nanocubes (Au-Pd) tethered to a conductive substrate by means of CNTs.[39] This approach provided a surface topology for the sensing platform and catalyst in an attempt to increase the analyte introduction rate. Other studies involved tethering Pd nanocubes and Pt nanospheres in like manner (Figure 5-1).[1] As an extension to these, a study on the *packing density*

of Pt nanospheres along CNT tethers revealed that tightly packed nanospheres outperformed sparse Pt nanosphere loadings in terms of greater sensing range and sensitivity.[22]

One of the most effective glucose sensors studied, however, incorporated multilayered graphene petal nanosheets (MGPNs) on a planar substrate.[10] The MGPNs were then functionalized with Pt nanospheres of varying packing density and used in H_2O_2 and glucose sensing. This study confirmed that an increase in functionalized surface area had a significant impact on the performance of the sensor (sensitivity and sensing range). The performance increase was achieved through three surface area enhancements: usage of non-planar graphene topologies, increased Pt loading/proximity, and usage of Pt morphologies that had urchin-like nanowire extensions (Figure 5-2). It is worth noting, however, that loading the graphene structure beyond a certain threshold led to a slight decrease in the sensor's performance. Therefore, it is important to determine a deposition procedure that yields optimal loading based on available substrate surface area.

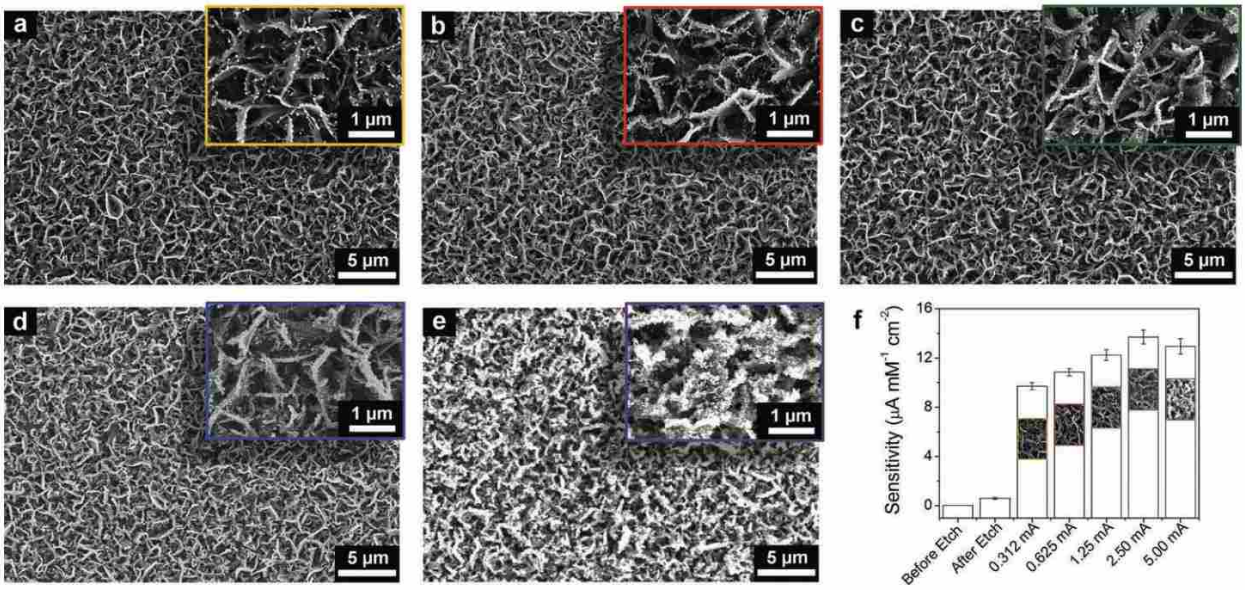

Figure 5-2: MGPNs functionalized **(a-e)** with increasing Pt nanoparticle density. Plot **(f)** showing sensitivity threshold indicates an optimal Pt loading.[10]

While increased sensing surface area has been pursued using novel topologies (namely carbon structures), transport of the analyte to sensing surfaces in previous studies has been essentially similar to flow past a flat plate in a stirred solution.[1,10,22,115,116] The reason for stirring is to quickly achieve a homogeneous solution while additional glucose is added to increase the concentration. Surface textures may protrude into the flow like extended surfaces but even graphene[10] and CNT devices[117] are essentially flat relative to the bulk fluid they are contacting. Further, only those analytes close to the sensing surface are detected while the remaining analytes depend on diffusion, potential advection (if stirred), or migration (movement caused by an electric field) to be presented to the sensing surface for detection. Thus planar sensing structures within static/stirred environments have inherently limited analyte introduction rates.

Initial testing involved the use of Pt-CNT-MMs for the amperometric sensing of H_2O_2 in static and stirred analyte flow conditions. As will be shown, the amperometric response is dependent on the analyte flow condition – something often overlooked in related studies. Specifically, exploiting flow conditions to achieve higher analyte introduction rates contributes to larger amperometric response. Accordingly, the amperometric response of Pt-CNT-MMs toward H_2O_2 oxidation will be shown to increase with increasing stir speed (or flowrate, in the case of through-flow testing). Application of Pt-CNT-MMs in *through-flow* conditions will then be demonstrated to show enhanced amperometric response, relative to the static/stirred cases, due to the larger analyte exposure to catalytic surface area and the introduction of boundary layer confinement. Because large amperometric response corresponds to high sensitivity, through-flow sensing using Pt-CNT-MM structures is demonstrated to be a very promising route to non-invasive glucose sensing. Initial studies will be limited to H_2O_2 sensing exclusively, with future work including glucose sensing upon biofunctionalization of the Pt-CNT-MM microstructure.

5.2 Results and Discussion

Transport enhancement for amperometric sensing of H_2O_2 was demonstrated using Pt-CNT-MM samples fabricated according to the techniques presented in Chapter 3, and includes samples fabricated using all three lithography masks referred to in section 3.2.3. Surface area available for participation in redox reactions (electroactive surface area) can be determined using cyclic voltammetry (CV). This measurement, taken for sample fabricated using each of the three lithography masks (diamond, small/large circle), is then used in subsequent calculations for the determination of Pt-CNT-MM performance, with regard to amperometric sensing of H_2O_2. Amperometric sensing was conducted under static, stirred, and through-flow conditions using Pt-CNT-MMs, and preliminary data is used for comparison of microstructure sensitivity with respect to a conventional sensor.

5.2.1 Electroactive Surface Area (Cyclic Voltammetry)

Cyclic voltammetry is a common standard by which the effective electrocatalytic surface area of an electrode can be measured. In a standard CV setup, three electrodes are present and submerged in a mediator solution. This solution is carried through several redox cycles as a changing voltage is applied between the working and reference electrodes. During this time, the current is measured between the working and counter electrodes and plotted versus applied potential.[118] With knowledge of the diffusion coefficient of the mediator solution, and using the electrical current to quantify the redox reaction rate at the electroactive surface, these measurements can be used for calculating the electroactive surface area. This measurement is important, as greater electrocatalytic surface area translates to larger amperometric signal for a given concentration of analyte.

The measurement metrics of CV, however, depend upon the diffusion of fresh analyte to the electrocatalytic structure as it is performed in a quiescent solution. Thus, it is believed that CV may not be the most representative means of characterizing a structure intended for through-flow applications. In other words, it is likely that most of the redox reactions occurring during CV happen on the frontal and entry-region surfaces of the Pt-CNT-MMs with limited contributions deep within the microchannels of a Pt-CNT-MM. This limitation could very well lead to inaccurate quantification of the electroactive surface area. A related study demonstrated the potential inaccuracies from CV regarding electroactive surface area of gold nanopillars.[19] Although CV may not be the most suitable means for the electrochemical characterization of Pt-CNT-MMs, selected CV data is presented here from which useful observations regarding mass transfer and sensitivity can be drawn.

Duralco 120 silver epoxy was used to attach Nichrome wire to each sample used for CV testing. After the silver epoxy had cured (approximately 24 [hrs]), a chemically inert lacquer coating was applied to the silver joint. CV tests were conducted using a CHI 630E Potentiostat/Galvanostat. A three-electrode cell was setup with the CNT-MM samples (no Pt) acting as the working electrode, a Ag/AgCl electrode acting as reference electrode and a coiled Pt wire as counter electrode. Initial tests were performed using a ferricyanide solution acting as mediator. Three cycles were run per sample through a potential range of -0.2 to 0.6 [V] at a scan rate of 10 [mV s^{-1}]. The peak redox current for each sample was taken as the average of both anodic/cathodic peak currents of the latter two CV cycles. All runs were performed at room temperature.

Electroactive surface area (EASAs) was calculated using the Randles-Sevcik Equation (eq 6), where i_p is the peak redox current [A], n is the number of electrons transferred per redox

reaction, A is the EASA [cm^2], D is the mediator diffusion coefficient (6.7×10^{-6} [$cm^2\ s^{-1}$] for a ferricyanide solution of 4 [mM] $Fe(CN)_6^{3-}$ and 1 [M] KNO_3),[1,119] c is the solution concentration [mol cm^{-3}], and v is the potential scan rate [V s^{-1}].[120]

$$i_p = 2.686 \times 10^5\, n^{3/2}\, A\, c\, D^{1/2}\, v^{1/2} \quad (6)$$

To allow for comparison between samples of any dimension as well as account for variations in growth across the sample surface, all CV data was normalized according to sample mass (Figure 5-3a). Hence, EASA calculations were used to determine the electroactive specific surface area (ESSA, *i.e.* EASA per unit mass) for each sample. Three O_2 etched CNT-MM samples were shown to have an average ESSA of 293.1 [$cm^2\ g^{-1}$] with a standard deviation of 27.8 [$cm^2\ g^{-1}$] (*i.e.* 293.1 ± 27.8 [$cm^2\ g^{-1}$]). This measurement indicates that not only is our O_2 etched CNT-MM sensing platform conductive, it is electrocatalytic. Thus, the O_2 etched CNT-MM structures can participate in the electrochemical reduction of a given chemical species while providing a conductive substrate on which catalytic Pt nanoparticles may be deposited.

Repeating CV tests for a given (O_2 etched) CNT-MM sample under varying scan rates revealed a linear relationship between the magnitude of the normalized anodic peak current and the square root of the scan rate for the CNT-MM sample within the ferricyanide mediator solution (Figure 5-3b). This linear correlation (R^2 value > 0.99) suggests that the redox reaction of ferricyanide at the surface is a diffusion-controlled process for CV in a static environment.[121-123] It is therefore expected that in a convective-enhanced environment, larger measured currents would be obtained for a given solution concentration (increased sensitivity). This further motivates the fabrication of MM geometries for use in through-flow environments.

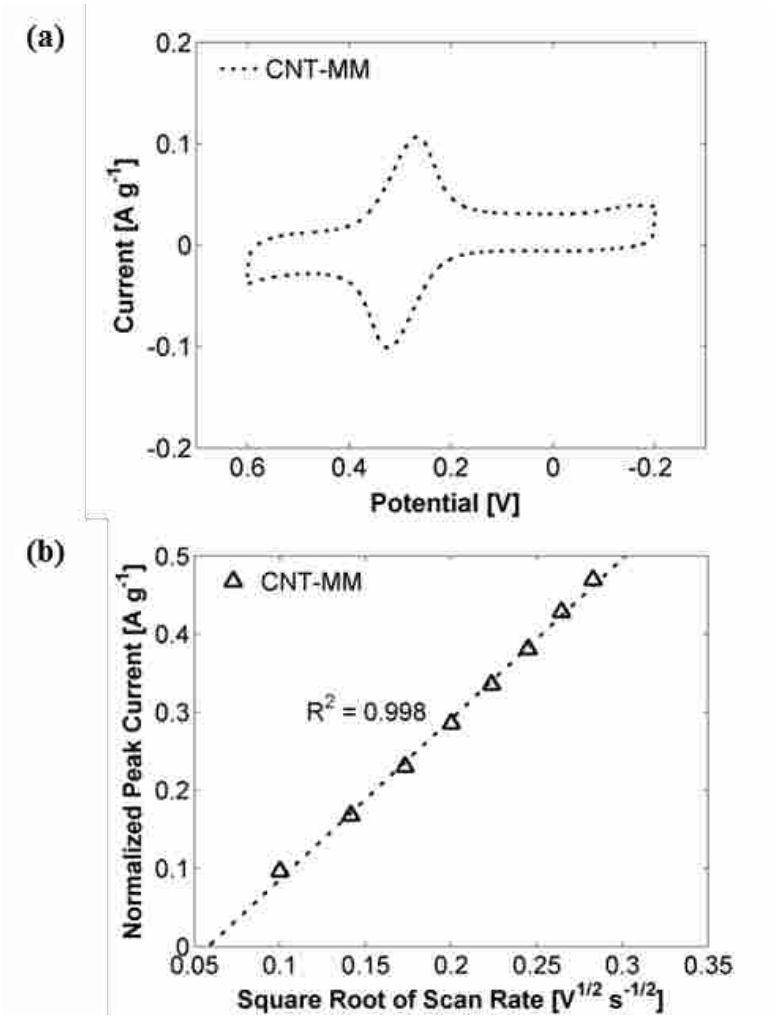

Figure 5-3: CV characterization of an O_2 etched CNT-MM sample within ferricyanide mediator solution (4 [mM] $Fe(CN)_6^{3-}$ and 1 [M] KNO_3). **(a)** Representative cyclic voltammogram (current normalized by sample mass) for (O_2 etched) CNT-MM sample. **(b)** Plot of the magnitude of the normalized anodic peak current *vs.* the square root of the scan rate for an O_2 etched CNT-MM sample, indicating that the transport of ferricyanide to the CNT-MM surface is a diffusion-controlled process.

After receiving Pt deposition, the Pt-CNT-MM samples were characterized using CV. Representative data for the diamond patterned samples is provided in Appendix E.1, including a comparison between CNT-MM and Pt-CNT-MM samples. When using a ferricyanide mediator solution, the CNT-MM sample displays a larger electroactive surface area. During the majority of each scan, however, the Pt-CNT-MM samples produce a consistently larger current. Further

comparison of CV responses for CNT-MM and Pt-CNT-MM structures, with respect to various mediator solutions, may be the focus of future studies.

Of interest to our current work, the ESSA was determined for each Pt-CNT-MM pattern using two or more test samples per pattern type. The ESSAs, with respect to a ferricyanide solution, were determined to be 53.3 ± 6.3, 82.0 ± 9.5, and 70.4 ± 0.3 [$cm^2\ g^{-1}$] for the diamond, small circle, and large circle patterns, respectively. It should be noted that only nominal values for ESSA were used, in conjunction with additional testing, to determine parameters such as sensitivity, *etc*. in the following sections.

5.2.2 Chronoamperometry

'Chronoamperometry,' or the study of current with respect to time, typically refers to measuring a current between electrodes given some time-dependent applied voltage. In this study, electrical current between electrodes was measured given some time-dependent *molar introduction rate*. By amperometrically measuring the rate of electrons exchanged at an electrode surface (electrical current) during oxidation, one can calculate the number of molecules *oxidized* at that surface per unit time (molar oxidation rate). It should be noted, however, that the molar oxidation rate (or 'sensed' molar introduction rate) may be less than the *actual* molar introduction rate because of slow electron transfer kinetics at the electrode. Section 5.2.4 reveals, however, that through-flow chronoamperometric testing of Pt-CNT-MM samples demonstrate near equivalence between the molar oxidation and introduction rates. Amperometric measurements correspond to the molar oxidation rate according to the equation shown below (eq 7).

$$Molar\ Oxidation\ Rate\ [mol\ s^{-1}] = \tag{7}$$

$$(Current\ [A])\left(\frac{1\ [C\ s^{-1}]}{1\ [A]}\right)\left(\frac{6.24151\times10^{18}\ [e^-]}{1\ [C]}\right)\left(\frac{1\ H_2O_2\ [molecule]}{2\ [e^-]}\right)\left(\frac{1\ [mol]}{6.02\times10^{23}\ [molecules]}\right)$$

Using chronoamperometry to measure the molar oxidation rate enables us to quantify the relative mass transport enhancement among a variety of electrocatalytic structures and for a variety of flow conditions. With respect to sensing applications, mass transport enhancement will result in lower limits of detection (LOD) and higher sensitivities, so long as the oxidation reaction rate at the sensing surface exceeds the analyte introduction rate to that surface. Parameters such as LOD and sensitivity (in addition to linear sensing range and response time) can all be determined using amperometric testing (current-time plots) such as the one shown below for the Pt nanosphere and Palladium nanocube structures mentioned previously (Figure 5-4).

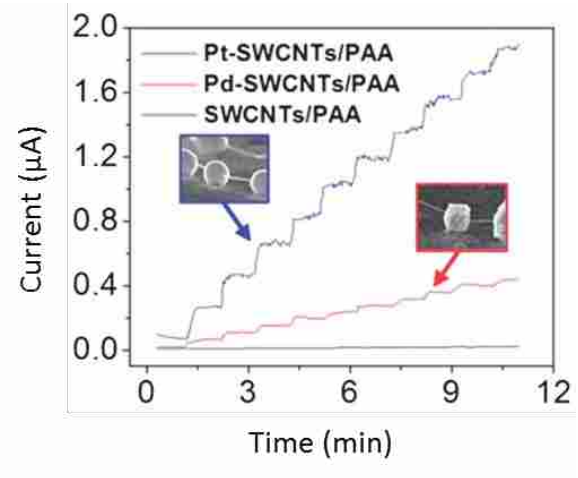

Figure 5-4: Current-time plot indicating responsiveness of GluOx/Pt-SWCNTs/PAA, GluOx/Pd-SWCNTs/PAA and GluOx/SWCNTs/PAA sensing structures to successive aliquots of H_2O_2, where GluOx indicates biofunctionalization of the aforementioned electrodes with glucose oxidase. Samples were tested in 20 [mL] of phosphate buffer solution (PBS at pH 7.4) using a three electrode cell and working voltage of 350 [mV]. Adapted from Claussen *et al*.[1]

In the interest of investigating mass transport enhancement *via* increased surface area, flow rate of analyte solution, and boundary layer confinement, initial studies are restricted to the measurement of the molar oxidation rate. As discussed previously, the molar oxidation rate is surface area dependent. Normalizing this value by the electroactive surface area of the sensing

device removes the surface area dependence and allows for conclusions to be drawn about the effects of increased analyte flow rate and boundary layer confinement, as well as relative electrocatalytic performance. Normalization of the molar oxidation rate by the electroactive surface area is shown below (eq 8). An analysis of the data presented in Figure 5-4 is demonstrated here as an example of how equations 7 and 8 can be used to better understand the mass transport involved in amperometric chemical sensing studies.

$$Molar\ Flux\ [mol\ m^{-2}s^{-1}] = \left(\frac{Molar\ Oxidation\ Rate\ [mol\ s^{-1}]}{Electroactive\ Surface\ Area\ [m^2]}\right) \quad \textbf{(8)}$$

In the case of the amperometric testing shown in Figure 5-4, the electrical current was measured as successive aliquots of H_2O_2 were added to the 20 [mL] of PBS test solution at approximately 1 [min] intervals. As an illustration of the molar flux sensed by the GluOx/Pt-SWCNT/PAA and GluOx/Pd-SWCNT/PAA platforms, the respective measured currents shown in Figure 5-4 were investigated. At 1.5 [min], the measured currents for the GluOx/Pt-SWCNT/PAA and GluOx/Pd-SWCNT/PAA sensing platforms were approximately 0.27 and 0.07 [μA], respectively (plot image processed to extract values using ImageJ software). It is also reported that the measured electroactive surface area of the GluOx/Pt-SWCNT/PAA and GluOx/Pd-SWCNT/PAA sensing platforms were reported to be (2.06 ± 0.5) x 10^{-4} cm^2 and (2.25 ± 0.5) x 10^{-4} cm^2, respectively. Using equation 7, it was determined that the GluOx/Pt-SWCNT/PAA structure achieved a molar oxidation rate of 1.4 [pmol s^{-1}], while the GluOx/Pd-SWCNT/PAA structure achieved only 0.36 [pmol s^{-1}].

Normalization of the molar oxidation rates of the GluOx/Pt-SWCNT/PAA and GluOx/Pd-SWCNT/PAA sensing platforms by their respective electroactive surface areas, according to equation 8, revealed a molar flux of 0.68 and 0.16 [μmol m^{-2} s^{-1}], respectively. This demonstrates that the GluOx/Pt-SWCNT/PAA sensing structure performed more than four times better than the

GluOx/Pd-SWCNT/PAA structure, which is in agreement with the reported work regarding relative sensitivities of the two structures.[1] Because the conditions and concentrations used in both cases were the same, and because the molar oxidation rate term was normalized by the relative electroactive surface areas, it was determined that the electrocatalytic properties of the Pt-SWCNT/PAA structure afforded it the better performance or, rather, higher oxidation efficiency.

5.2.3 Mass Transport Enhancement in Static and Stirred Environments

As will be shown, convective enhancement of an analyte flow field can drastically effect the molar oxidation rate at a sensing surface. Accordingly, the measured current per given analyte concentration (sensitivity) is enhanced. To demonstrate this point, and to establish a baseline against which to compare through-flow sensing, chronoamperometric testing of Pt-CNT-MMs was conducted in static and stirred environments of H_2O_2.

Pt-CNT-MM samples were fabricated according to the methods described in section 3.1.2 and were functionalized by an electroless Pt deposition process as described in section 3.1.3 (~30% [w/w] Pt-C). Chronoamperometric testing was performed in a three electrode cell with a flexible Ag/AgCl reference electrode (saturated KCl), Pt wire counter electrode, and the Pt-CNT-MM structures operating as the working electrode with an applied voltage of 700 [mV] in a Tris buffer solution (25 [mM] Tris, $(HOCH_2)_3CNH_2$; 0.5 M NaCl; pH 10.0). It is here noted that this same Tris buffer composition was used in all following tests. An N_2 envelope was maintained above the buffer solution in order to prevent interference from the diffusion of oxygen into the electrochemical cell. Pt-CNT-MM structures were electrically connected to a PAR Model 173 Potentiostat/Galvanostat using a gold plated clip. Aliquots of H_2O_2 were prepared as described in Appendix E.2 (prepared from 0.800 ± 0.002 [M] stock H_2O_2 solution).

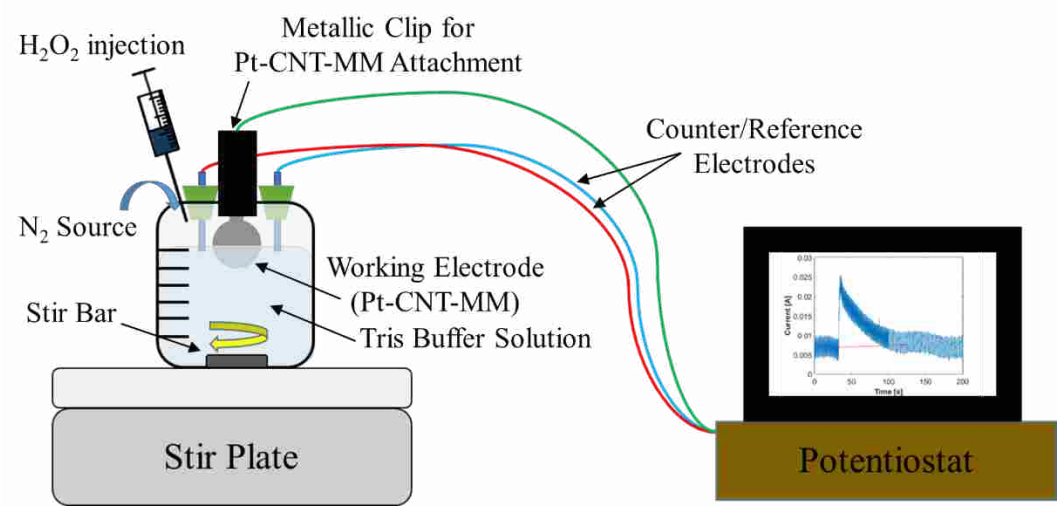

Figure 5-5: Three electrode cell used for chronoamperometric testing of Pt-CNT-MM samples in static and stirred environments of H_2O_2. Samples positioned such that approximately half of the sample was submerged in solution. Care was taken regarding sample placement in order to minimize error.

Upon applying an electric potential, reduction of the stirred buffer solution (and dissolved oxygen in solution) produces a large measurable current. As the reduction process continues, the current eventually reaches a reference baseline from which an absolute H_2O_2 oxidation current can be measured. Reference baselines for the reduced buffer solution were measured for static and stirred cases, each case lasting about 2 [min] (50, 75, 100, and 150 [rpm]). It was observed that the buffer baseline did not change significantly with increasing stir speed. After sufficiently reducing the stirred buffer solution, and once the solution had maintained a stir speed of 150 [rpm] for approximately 2 [min] (Figure 5-6, i), 5 [µL] of stock H_2O_2 (0.800 [M]) was injected into the 35 [mL] buffer solution achieving a 114 [µM] solution, similar to a realistic concentration of glucose in saliva. Electrical current measurements were taken throughout the test, with the stir speed decreased at the beginning of each 2 [min] interval (Figure 5-6, vi-x).

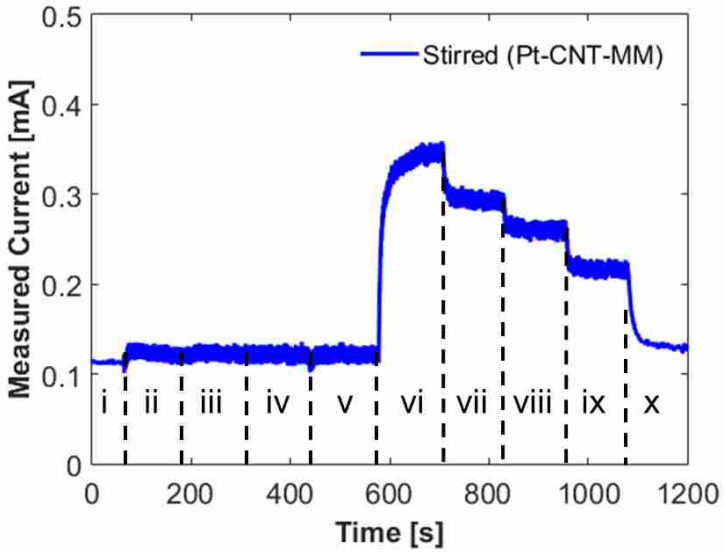

Figure 5-6: Example chronoamperometric sensing of H_2O_2 (114 [µM]) in 35 [mL] stirred Tris buffer solution using diamond patterned Pt-CNT-MM. Tris buffer reference baseline for **(i)** static environment, and stirred environment at **(ii)** 50, **(iii)** 75, **(iv)** 100, and **(v)** 150 [rpm]. After 5 [µL] injection of stock H_2O_2 (0.800 [M]) solution, measured currents were taken for stirred environments at **(vi)** 150, **(vii)** 100, **(viii)** 75, and **(ix)** 50 [rpm] as well as for **(x)** static conditions.

The decrease in measured current between successive intervals from vi to x in Figure 5-6 is due primarily to the corresponding decrease in stir speed. Because amperometric sensing requires the oxidation (or depletion) of H_2O_2, however, there exists a gradual decrease in total H_2O_2 concentration. This gradual decrease in H_2O_2 concentration also contributes to a decrease in measured electrical current, but can be shown to be negligible compared to stir speed effects. In order to quantify the maximum current drop due to H_2O_2 depletion, another test was conducted with a Pt-CNT-MM sample similar to that used for Figure 5-6 wherein the same H_2O_2 concentration (114 [µM]) and test setup was used except that the stir speed was held at the maximum value (150 [rpm]) from the beginning of interval vi onward (held for a total of 10 [min]; Figure 5-7). After the H_2O_2 injection, the measured current is observed to remain essentially constant during the first 2 [min] interval (interval vi) and decrease by about 17.6%, with respect

to the buffer baseline, over the entire post-injection range (10 [min]). It is observed that H_2O_2 depletion can contribute a significant decrease in measured electrical current. However, as the test shown in Figure 5-7 is an extreme case, it is reasonable to assume negligible interference from H_2O_2 depletion for the remaining tests mentioned herein. In other words, it will be assumed that the H_2O_2 concentration is essentially constant for the duration of a given test. Future work will be devoted to accounting for any decrease in measured electrical current due to H_2O_2 depletion.

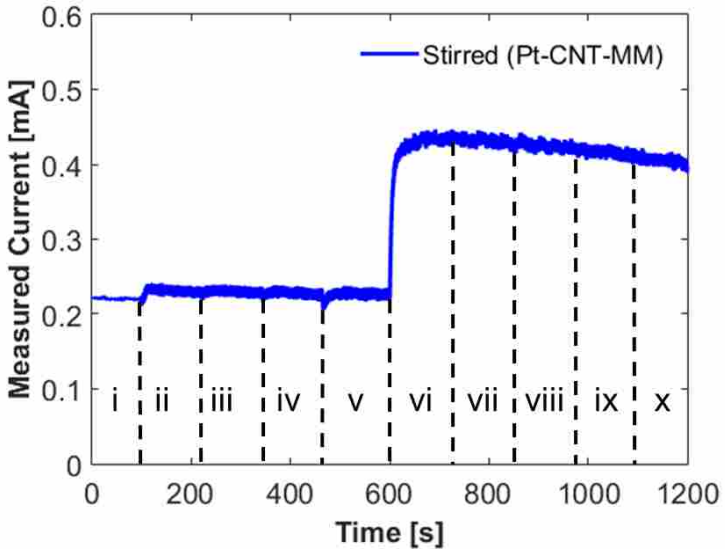

Figure 5-7: Chronoamperometric sensing of 114 [µM] H_2O_2 in 35 [mL] Tris buffer solution (using sample similar to that used for Figure 5-6; diamond patterned). The data demonstrates that even in the extreme case (maximum stir speed maintained from the beginning of interval vi onward), the measured current decreases by only 17.6 % over a 10 [min] range.

Following the procedure demonstrated earlier for GluOx/Pt-SWCNT/PAA and GluOx/Pd-SWCNT/PAA electrodes, the molar flux of the Pt-CNT-MM demonstrated in Figure 5-6 was calculated. With 2.135 [cm^2] of the total EASA exposed to the H_2O_2 solution, calculation of the molar introduction rate and flux sensed by the Pt-CNT-MM sample revealed the following (Figure 5-8). The Pt-CNT-MM achieved a maximum average molar flux of about 5.45 [µmol m^{-2} s^{-1}] at 150 [rpm] which is about thirty times larger than that of the static case (data averaged over a 20 [sec] interval). This demonstrates mass transport enhancement *via* increased flow rate resulting

from a change in stir speed. It is expected that the maximum average molar flux would continue to increase with stir speed until the maximum H_2O_2 oxidation rate achievable by the Pt electrocatalyst were reached.

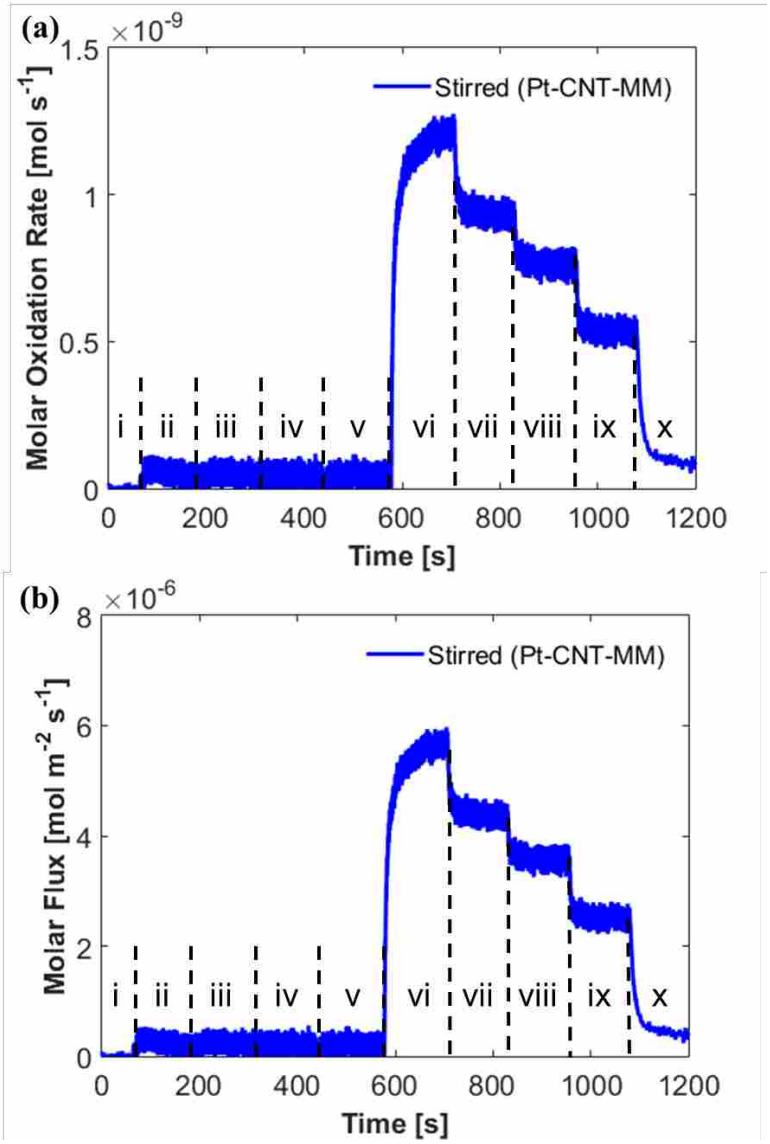

Figure 5-8: Molar **(a)** introduction rate and **(b)** flux calculated using data from Figure 5-6, with respect to stirred buffer baseline. Note change in magnitude of y-axis once normalized by frontal surface area. Regions **(i-x)** correspond with similar regions on Figure 5-6.

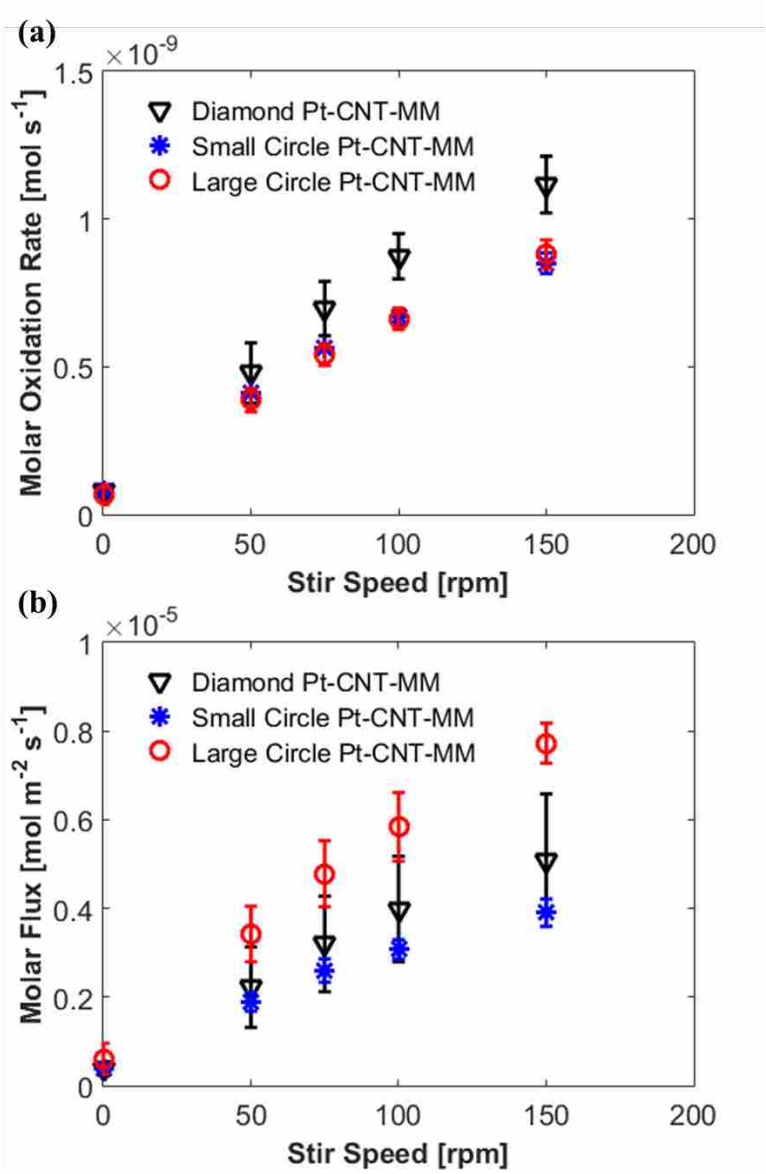

Figure 5-9: Molar **(a)** introduction rate and **(b)** flux for Pt-CNT-MM samples under static and stirred (50, 75, 100, and 150 [rpm]) conditions. Three Pt-CNT-MM samples were tested for each pattern type using 114 [μM] H_2O_2, in Tris buffer, for each of the stir speeds indicated. Introduction rates were determined using equation 7; molar flux values were calculated using equation 8 and the EASA for each respective sample. Values shown above represent an average among the samples, with error bars indicating the standard deviation among samples for a given test condition.

Also, it can be seen in Figure 5-8 that immediately after H_2O_2 injection, the molar flux rises gradually to approach steady state. Calculation of molar flux for interval vi would be skewed for

data taken during conditions preliminary to steady state. To minimize inaccurate measurements in future work, additional time will be given for interval vi such that steady state will have been achieved. Additionally, intervals following interval vi may be shortened in order to help minimize error due to H_2O_2 depletion.

Chronoamperometric testing was likewise conducted on three distinct Pt-CNT-MM samples from each of the three mask patterns (9 samples total). Figure 5-9 illustrates the molar oxidation rate and flux measured for these samples at each flow condition. In consideration of the standard deviation presented for each data point in Figure 5-9b, it is observed that the molar flux is approximately the same per stir speed, regardless of pattern type. Achieving similar response among samples for a given stir speed would be expected, in this case, as the data has been normalized by ESSA.

It is interesting to note that the Pt-CNT-MM samples having the larger hydraulic diameter (large circle pattern; hydraulic diameter of 16.1 [μm]) tend to achieve a higher molar flux as shown in Figure 5-9. Because the pressure drop required to push a fluid through a channel decreases with increasing channel diameter, it is possible that the large circle pattern allows for greater H_2O_2 penetration into the microchannels than does the alternate patterns in the stirred flow condition. The greater H_2O_2 penetration results in exposure of the H_2O_2 to greater surface area for subsequent oxidation and therefore greater measured electrical current. This result further motivates high surface area sensing platforms.

The data shown in Figure 5-9 also demonstrates transport enhancement, or increase in molar flux, of H_2O_2 in solution with increasing stir speed. The data suggests that, for the range of stir speeds tested, the correlation between stir speed and molar flux is approximately linear. As

stated previously, and confirmed by the data presented in Figure 5-9, convective enhancement of an analyte flow field drastically effects the molar oxidation rate and flux at a sensing surface.

5.2.4 Mass Transport Enhancement in Through-Flow Environments

The coupled transport enhancement made possible by an increase in surface area and analyte flow can be further enhanced by boundary-layer confinement. Accordingly, the utility of Pt-CNT-MMs applied in a *through-flow* environment is demonstrated herein and shown to dramatically increase chemical analyte introduction rates and thereby improve upon conventional sensing methods.

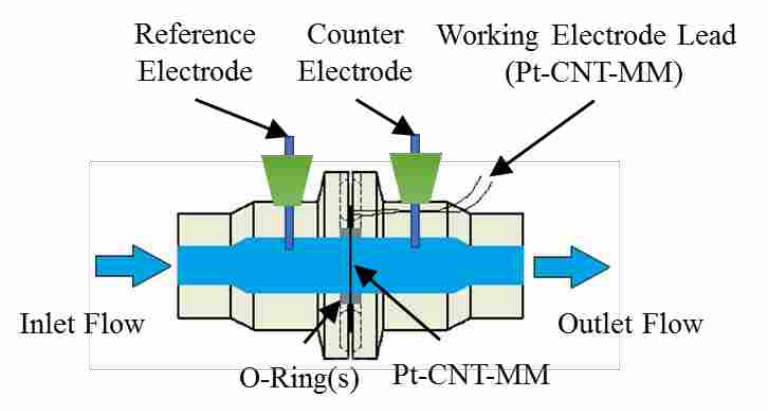

Figure 5-10: Teflon flow cell configuration for through-flow chronoamperometric testing of Pt-CNT-MM samples for the investigation of mass transport enhancement *via* boundary layer confinement.

Sensing of H_2O_2 in a through-flow environment required that a suitable test setup be fabricated. Specifically, a chemically inert flow cell was needed that allowed for the inflow and outflow of dilute H_2O_2 in a buffer solution. Furthermore, it was required that the flow cell secure a water-tight seal across Pt-CNT-MM samples without causing damage to the samples. Finally, the flow cell must allow for electrode access into the chemical flow, thereby forming a dynamic

electrochemical cell. To meet these requirements, a Teflon flow cell (Figure 5-10) was designed and manufactured for through-flow chronoamperometric testing of Pt-CNT-MM samples.

Samples were carefully secured within the flow cell, which was connected to a Harvard Apparatus syringe pump. The 'feeder' syringe, located on the syringe pump, acted to infuse and withdraw the Tris base buffer solution into, and out of, the flow cell. Air within the flow cell was evacuated as buffer solution was initially infused from the syringe pump. Exposed buffer solution was collected in a 'reservoir' syringe which was exposed to a continuous stream of N_2 gas. Reduction of the buffer solution, in preparation for sensing of H_2O_2, involved repeatedly cycling the buffer solution through the flow cell while the 700 [mV] working potential was applied to the Pt-CNT-MM sample. Once reduced, chronoamperometric testing began.

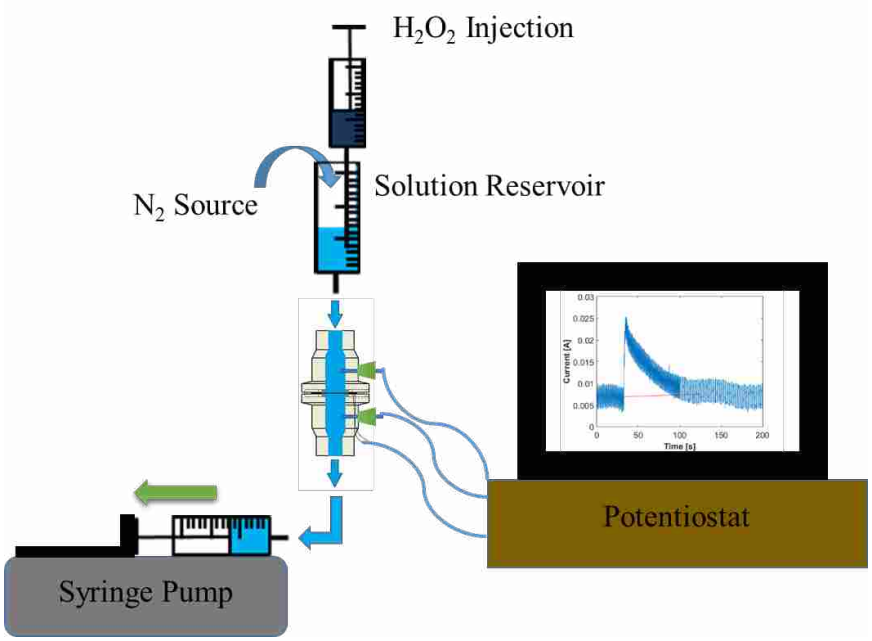

Figure 5-11: Through-flow chronoamperometric setup using flow cell. Pt-CNT-MM structures housed in flow cell act as the working electrode while the buffer solution with trace H_2O_2, is pumped through for sensing.

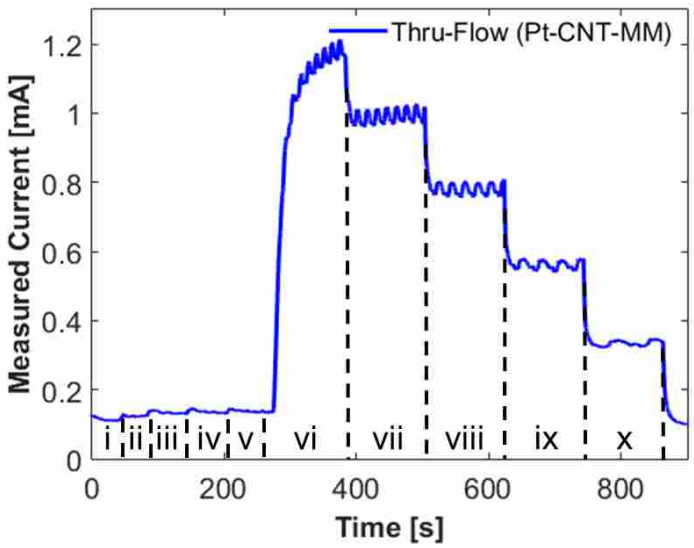

Figure 5-12: Example chronoamperometric sensing of 114 [μM] H_2O_2 (in Tris buffer) in through-flow setup using large circle patterned Pt-CNT-MM. Tris buffer reference baseline for through-flow environment at **(i)** 10, **(ii)** 20, **(iii)** 30, **(iv)** 40, and **(v)** 50 [μL s^{-1}] (measured for ~1 [min] per interval). After injection of stock H_2O_2 solution (0.800 [M]), measured electrical currents were taken for through-flow environments at **(vi)** 50, **(vii)** 40, **(viii)** 30, **(ix)** 20, and **(x)** 10 [μL s^{-1}]. Note that there was some delay between the point of injection (beginning of vi) and rise in electrical current because of the time required for the injection to reach the Pt-CNT-MM sample within the flow cell. Also, note that the signal frequency decreases with successive intervals from vi to x due to stepping of the syringe pump motor.

Through-flow chronoamperometric testing for Pt-CNT-MMs was conducted in a stepwise fashion, similar to that of the static and stirred testing. Using a syringe pump, Tris buffer solution (of the same composition as was used for static/stirred testing) was cycled through the Pt-CNT-MMs until fully reduced (Figure 5-11). The buffer solution was then withdrawn through the Pt-CNT-MMs and into the pump syringe while baseline electrical currents were measured for 10, 20, 30, 40, and 50 [μL s^{-1}] flowrates, respectively (Figure 5-12). Upon completion of measuring the baseline current for 50 [μL s^{-1}], H_2O_2 was injected into the N_2 bubbled Tris reservoir so as to create a H_2O_2 solution of approximately 114 [μM] within the reservoir (typically a 3.1 [μL] injection of 0.8 [M] H_2O_2 into 22 [mL] of Tris buffer). Upon entering the flow cell, the measured current was

observed to increase dramatically, and decrease with each successive decrease in flowrate (flowrate stepped from 50 to 10 [µL s^{-1}] at 2 [min] intervals).

As demonstrated previously, measured electrical current for the static/stirred testing was effected by H_2O_2 depletion (*i.e.* a change in the bulk H_2O_2 concentration). Because the through-flow setup utilized a flow cell, however, solution once exposed to the Pt-CNT-MM (within the flow cell) was then discharged into the syringe pump syringe and held there until the end of the testing. This ensured that Pt-CNT-MM samples would be exposed only to H_2O_2 solutions of constant concentration, thereby removing the possibility of measurement error due to bulk solution H_2O_2 depletion. This is demonstrated in Figure 5-13 by the near-constant electrical current measured for a Pt-CNT-MM sample exposed to a constant flowrate of H_2O_2 solution (50 [µL s^{-1}]; 114 [µM] H_2O_2 in Tris buffer). It can then be assumed that, post H_2O_2 injection, any change in measured electrical current is due exclusively to a change in solution flowrate.

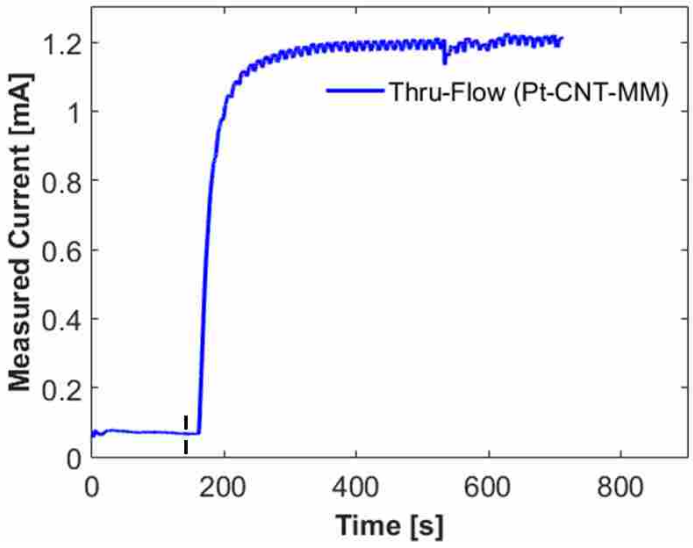

Figure 5-13: Chronoamperometric test using 114 [µM] H_2O_2 (in Tris buffer) in through-flow environment at 50 [µL s^{-1}] flowrate (using same large circle patterned Pt-CNT-MM sample as was used for the test shown in Figure 5-12). The data demonstrates that even in the extreme case (maximum flowrate held throughout duration of test), the measured current remains nearly constant post H_2O_2 injection (injection indicated by dashed line).

Initial testing has revealed much about the mass transport enhancement made possible by the Pt-CNT-MM microstructure in a through-flow environment, as well as its improvement on sensing performance compared to static/stirred conditions. Specifically, Figure 5-14 shows a ten-fold increase in molar flux for the Pt-CNT-MM sample between the initial stirred flow and through-flow conditions (150 [rpm] *vs*. 50 [µL s^{-1}]). Though a direct comparison of relative flowrates between stirred and through-flow conditions is impractical, the large increase in molar flux can be attributed to both an increase in exposed electrocatalytic surface area, as well as increase in boundary layer confinement. It was also observed that, for the prescribed test conditions, the molar flux sensed using the Pt-CNT-MM structure in a through-flow environment at 10 [µL s^{-1}] was approximately twice that achieved by the Pt-CNT-MM sample in a stirred environment at the maximum tested stir speed (150 [rpm]), and nearly fifty times that achieved in a static condition.

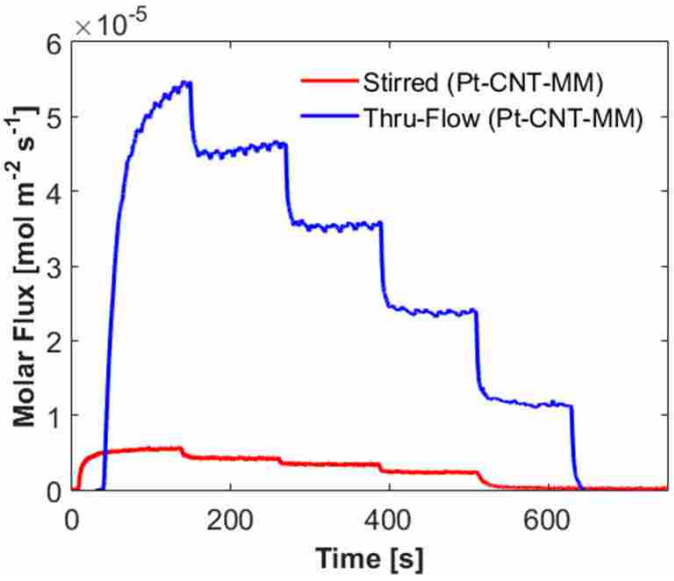

Figure 5-14: Chronoamperometric sensing of 114 [µM] H_2O_2 (in Tris buffer) using the same Pt-CNT-MM sample as was used for testing shown in Figure 5-6. It should be noted that data for the 'Thru-Flow (Pt-CNT-MM)' had a buffer baseline that was slightly increasing immediately prior to H_2O_2 injection. Given that the data is 'zeroed' on the y-axis, and that the molar flux plateaus (shown above) are fairly level, the sloping baseline likely contributed negligible error to the resultant plot.

Knowing both the H_2O_2 concentration of the buffer solution (114 [µM]) and the prescribed flowrate, the theoretical molar flux of the through-flow setup was calculated and compared to the experimentally obtained molar flux sensed by a Pt-CNT-MM sample (Figure 5-15; plot based on data shown in Figure 5-14). As shown in Figure 5-15, the calculated molar supply rate is nearly exactly matched by the sensed molar introduction rate, indicating that Pt-CNT-MM structures facilitate high mass transport from bulk solution to electrocatalytic surfaces for near-total oxidation of trace H_2O_2.

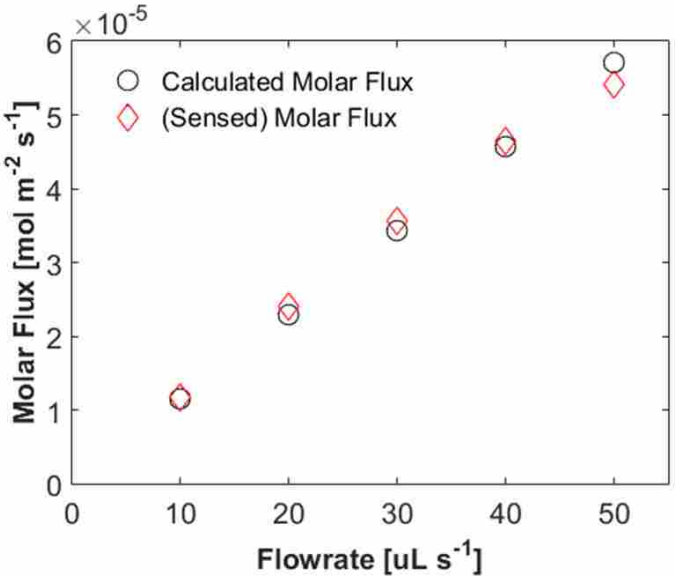

Figure 5-15: Comparison of calculated versus sensed molar flux for a Pt-CNT-MM sample in through-flow environment of 114 [µM] H_2O_2 in Tris buffer solution (calculated from data shown in Figure 5-14). Plot reveals high mass transport from bulk solution to electrocatalytic surface of Pt-CNT-MM for near-total oxidation of suspended H_2O_2.

The sensitivity of a given sensing structure can be determined from a knowledge of the electroactive surface area of the structure, as well as the amplitude of the measured electrical current when exposed to a known concentration of analyte. Testing was conducted to determine the sensitivity achieved by a diamond patterned Pt-CNT-MM sample in order to demonstrate the

utility of Pt-CNT-MMs applied in *through-flow* environments for chemical sensing and illustrate their improved performance with respect to conventional sensing methods. Accordingly, the EASA of the Pt-CNT-MM sample was determined by multiplying the sample mass (0.0801 [g]) by the respective average ESSA (53.3 [$cm^2\ g^{-1}$]), and was found to be 4.269 cm^2. This EASA was scaled according to the fraction of the sample exposed to the through-flow environment. Because the exposed sample area (predicated by the diameter of the flow cell O-rings) was 0.2314 times the total sample area, the scaled EASA was determined to be 1.000 [cm^2].

Through-flow data for the diamond patterned Pt-CNT-MM sample is shown in Figure 5-14, and repeated (in its entirety) in Figure 5-16. It was determined that an output current of 1.046 [mA], with respect to buffer baseline, was measured upon injection of H_2O_2 at a 50 [$\mu L\ s^{-1}$] flowrate (114 [μM] H_2O_2 in Tris buffer). Given that the H_2O_2 concentration was 114 [μM], and the EASA was 1.000 [cm^{-2}], the sensitivity of the Pt-CNT-MM structure was determined to be 9.18 [$mA\ mM^{-1}\ cm^{-2}$]. Therefore sensitivity of the diamond patterned Pt-CNT-MM is over one hundred times greater than that of the GluOx/Pt-SWCNT/PAA structures referenced previously (0.0724 [$mA\ mM^{-1}\ cm^{-2}$]).[1] The sensitivity demonstrated by the Pt-CNT-MM sample rivals even that of the high performance Pt-MGPNs (9.71 [$mA\ mM^{-1}\ cm^{-2}$]),[10] while allowing for further enhancement by optimizing the O_2 etching and Pt deposition schemes, as well as by increasing the H_2O_2 flowrate. These potential enhancements, and other future work, are summarized later in section 5.3.

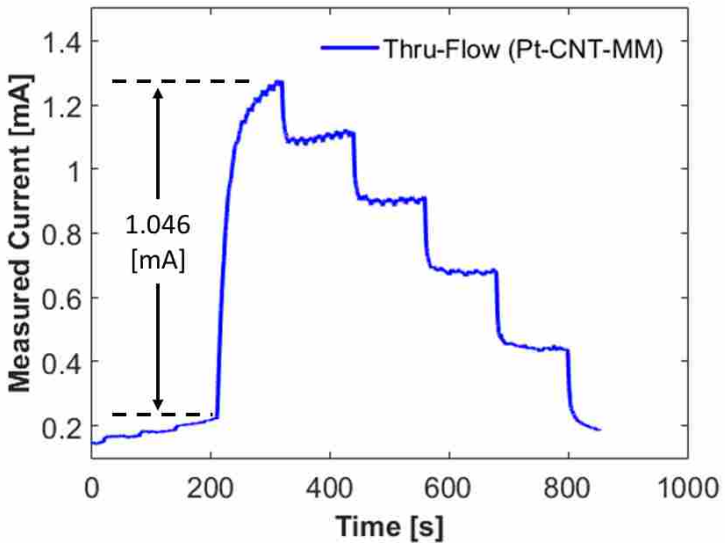

Figure 5-16: Chronoamperometric sensing of H_2O_2 (114 [µM]; in Tris buffer) using Pt-CNT-MM fabricated with the diamond pattern (sample from Figure 5-14 and Figure 5-15). Note that the upward slope of the baseline before injection may have introduced some error in the following calculations. Because of the large magnitude of the H_2O_2-induced signal, as well as the typical current trends following injection, it can be assumed that any error introduced by the sloped baseline is negligible. Initial peak current, with respect to buffer baseline, upon H_2O_2 injection is shown to be 1.046 [mA] at 50 [µL s^{-1}].

5.3 Conclusions

Application of Pt-CNT-MM structures for amperometric chemical sensing has been demonstrated for a H_2O_2 sample system. Specifically, these structures enhance the mass transport of suspended analyte (H_2O_2) to the electrocatalytic surface of the Pt-CNT-MM structure, and thereby improve overall sensor performance. Unlike other sensing platforms, Pt-CNT-MMs used in through-flow environments utilizes all three mass transport enhancement methods – increase of available electrocatalytic surface area, increase of analyte flow rate, and increase of boundary layer confinement. Performance of the Pt-CNT-MM in static, stirred, and through-flow environments

are studied and demonstrate the efficacy of through-flow sensing using high aspect ratio microstructures.

Post O_2 etched CNT-MM samples were characterized using cyclic voltammetry. These tests revealed that the CNT-MM structure is highly electrocatalytic, achieving an average ESSA of 293 ± 28 [$cm^2\ g^{-1}$]. This demonstrates that CNT-MMs are not only highly conductive, but are even electrocatalytic prior to Pt functionalization. Further testing confirmed that analyte transport to the CNT-MM structure is a diffusion-limited process, thereby validating the study of mass transport enhancement for chemical sensing.

Chronoamperometry is used to measure the H_2O_2 introduction rate to the Pt-CNT-MM microstructure. Each test was run using a 114 [μM] H_2O_2 solution, which simulated the concentration of glucose found in saliva. From the results of the chronoamperometric testing, molar introduction rate and molar flux were derived and used for comparison between flow conditions. Pt-CNT-MM testing in both static and stirred conditions confirmed that increasing the flow of analyte in suspension results in higher mass transport and, subsequently, sensor performance. Specifically, a Pt-CNT-MM sample having a (submerged) electroactive surface area of 2.135 [cm^2], exposed to a H_2O_2 solution being stirred at 150 [rpm], achieved a maximum average molar flux of 5.45 [μmol $m^{-2}\ s^{-1}$]. The molar flux achieved in the stirred condition was about thirty times that achieved in the static condition, demonstrating mass transport enhancement *via* increasing analyte flow in solution.

A chemically inert flow cell was designed and fabricated for the chronoamperometric testing of CNT-MM and Pt-CNT-MM samples in a through-flow environment. Specifically, samples were tested within a flowrate range of 10-50 [μL s^{-1}]. Initial studies revealed that the molar flux achieved for a Pt-CNT-MM sample in a through-flow environment (50 [μL s^{-1}]) was

approximately a ten-fold increase over that achieved in a stirred environment (150 [rpm]). This ten-fold increase in molar flux can be attributed to both an increase in analyte exposure to electrocatalytic surface area, as well as the introduction of boundary layer confinement. It was also observed that, for the prescribed test conditions, the molar flux sensed using the Pt-CNT-MM structure in a through-flow environment at 10 [$\mu L\ s^{-1}$] was approximately twice that achieved by the Pt-CNT-MM sample in a stirred environment at the maximum tested stir speed (150 [rpm]), and nearly fifty times that achieved in a static condition.

Using the prescribed H_2O_2 solution concentration (144 [μM]), the theoretical molar flux was calculated for each flowrate (10-50 [$\mu L\ s^{-1}$]) and compared to that sensed by a Pt-CNT-MM sample (same sample as in Figure 5-14 and Figure 5-16). Comparison of sensed molar flux to calculated molar flux revealed that Pt-CNT-MMs can achieve near-complete H_2O_2 oxidation within the flowrate range studied. This comparison also validates the accuracy of H_2O_2 sensing using Pt-CNT-MMs. Furthermore, chronoamperometric testing of the same Pt-CNT-MM sample revealed a sensitivity of 9.18 [$mA\ mM^{-1}\ cm^{-2}$], over one hundred times that of the GluOx/Pt-SWCNT/PAA structures referenced previously (0.0724 [$mA\ mM^{-1}\ cm^{-2}$])[1] and rivaling that of high performance Pt-MGPNs (9.71 [$mA\ mM^{-1}\ cm^{-2}$]).[10] Enhancement of the Pt-CNT-MM sensitivity may come by optimizing the O_2 etching scheme and Pt deposition, as well as by increasing the H_2O_2 flowrate. It is also proposed that future work involve investigating further enhancement *via* decreased microchannel diameter (greater boundary layer confinement).

CHAPTER 6. CONCLUSIONS AND FUTURE WORK

6.1 Conclusions

Rate limited chemical reactions can be enhanced by improving the mass transport of the suspended analyte to the catalytic (or electrocatalytic) surface. While many attempts have been made to enhance this mass transport, these approaches are limited to utilizing only two enhancement methods – increasing available catalytic surface area, and increasing the flow of analyte in solution. Flow through high aspect ratio microstructures, however, would provide additional mass transport enhancement *via* boundary layer confinement. Pt-CNT-MMs offer enhanced mass transport *via* all three methods, and were fabricated for demonstration in a H_2O_2 sample system, for which propulsion and chemical sensing applications were investigated.

Prior to demonstrating the efficacy of Pt-CNT-MM samples in rate limited chemical reaction applications, several characterization methods were employed. Among these, N_2 adsorption testing revealed that a typical O_2 etched CNT-MM sample provides a surface area that is roughly twenty thousand times that offered by a planar carbon structure of the same frontal dimensions, while maintaining a very small volumetric footprint. Because Pt-CNT-MM samples were also demonstrated to be hydrophilic and possess Pt coverage throughout the entirety of their microstructure, they provide high surface area catalysts which can be employed in static, stirred, and even through-flow environments for enhanced transport of suspended analyte.

H_2O_2 decomposition testing revealed that Pt-CNT-MM exhibit an activation energy of 26.96 [kJ mol^{-1}], which is among the best found in the literature. Low activation energy lends to higher H_2O_2 decomposition efficiency. This decomposition efficiency was demonstrated during propulsion testing of Pt-CNT-MM samples where, for a given H_2O_2 fuel concentration and flowrate, high fuel utilization was exhibited. Additional propulsion testing of Pt-CNT-MMs demonstrated that, under manual burst driven flow, eight inline Pt-CNT-MM samples produced 209 ± 49 [mN] of thrust. This thrust is well within the milli-newton thrust range typically required for MUV propulsion, and was shown to be at least several times greater than that produced by various biomimetic propulsion systems. Further, the proposed approach minimizes component exposure to the environment and is comprised of a simple, static architecture relative to other micro-propulsion systems. Additionally, it was shown that even greater thrust is attainable by further enhancing the introductory rate of the H_2O_2 fuel to the Pt-CNT-MMs, which would effectively increase the locomotive capability of this propulsion system.

Pt-CNT-MMs used for chemical sensing of H_2O_2 likewise demonstrated favorable performance. Initial studies revealed that the molar flux achieved for a Pt-CNT-MM sample in a through-flow environment (50 [μL s^{-1}]) was approximately a ten-fold increase over that achieved in a stirred environment (150 [rpm]). This ten-fold increase in molar flux can be attributed to both an increase in analyte exposure to electrocatalytic surface area, as well as the introduction of boundary layer confinement. Furthermore, comparison of sensed molar flux to calculated molar flux for through-flow conditions revealed that Pt-CNT-MMs can achieve near-complete H_2O_2 oxidation within the flowrate range studied. Additionally, chronoamperometric testing of a Pt-CNT-MM sample demonstrated a sensitivity toward H_2O_2 of 9.18 [mA mM^{-1} cm^{-2}] which is over one hundred times that of the GluOx/Pt-SWCNT/PAA structures referenced previously (0.0724

[mA mM^{-1} cm^{-2}]).[1] The sensitivity of Pt-CNT-MMs toward H_2O_2 was also shown to rival the sensitivity of high performance Pt-MGPNs (9.71 [mA mM^{-1} cm^{-2}]),[10] while allowing for further enhancement.

These findings suggest that mass transport enhancement, achieved by Pt-CNT-MMs applied in through-flow environments, heightens the performance achieved in rate-limited chemical reactions with respect to conventional catalysts. Specifically, Pt-CNT-MMs demonstrate high fuel utilization in H_2O_2 based propulsion applications, as well as offer a highly sensitive, preliminary microstructure for non-invasive glucose sensing.

6.2 Thesis Summary

Mass transport enhancement of rate-limited chemical reactions was realized through the use of Pt-CNT-MMs. This was achieved for a H_2O_2 sample system and demonstrated for propulsion and chemical sensing applications. This work is a culmination of the following objectives:

1. Synthesize a microarray membrane fabrication scheme.
2. Fabricate and characterize microarray membrane structure.
3. Demonstrate enhanced mass transport using microarray membrane in H_2O_2 sample system.
    - Underwater propulsion *via* decomposition of H_2O_2
    - H_2O_2 sensing for glucose detection applications

Much of the work contained herein has been demonstrated to the academic community through a variety of conferences. These include the 67th Annual Meeting of the APS Division of Fluid Dynamics (San Francisco, CA; November 2014), as well as the ASME 2013 IMECE Conference (San Diego, CA; November 2013). Additionally, material regarding Pt-CNT-MM

fabrication, characterization, and application to underwater propulsion is adapted from a paper accepted for publication by ACS Nano.[25]

6.3 Future Work

Successful demonstration of high performance propulsion and chemical sensing *via* Pt-CNT-MMs provides motivation for continued research. Major areas of interest include:

1. Thrust measurements taken for Pt-CNT-MM samples held in place using pressurized seals (O-rings, *etc*.), ensuring that fuel passes through microchannels.
2. Compare CV responses for CNT-MM and Pt-CNT-MM samples with respect to a variety of mediator solutions (ferricyanide *vs*. hydrogen peroxide, *etc*.).
3. Variability of Pt-CNT-MM ESSA with sample thickness.
4. Stirred and through-flow electroless Pt deposition schemes for improved catalyst coverage within CNT-MM microstructure.
5. Electrodeposition of Pt nanoparticles onto CNT-MMs.
6. Continued Chronoamperometric testing of CNT-MM/Pt-CNT-MM samples in a variety of flow conditions (static, stirred, through-flow).
    a. Investigate error in chronoamperometric measurements for static/stirred flow conditions caused by depleting H_2O_2 concentration (plot electrical current, with respect to time, for a variety of stir speeds given a set initial concentration).
    b. Study effects of microchannel geometry and CNT-MM microstructure (porosity, *etc*.) on sensing performance. Notably, investigate the higher performance of the large circle Pt-CNT-MM samples in Figure 5-9, with respect to alternate samples.

c. Reusability/lifetime testing.

d. Testing of Pt-CNT-MMs in phosphate buffer solution *vs*. Tris buffer solution.

7. Biofunctionalization of Pt-CNT-MMs for glucose sensing applications.
8. Compare current density of Pt-CNT-MMs with sensors found in the literature.
9. Perform pressure drop testing for each Pt-CNT-MM microchannel geometry and determine respective burst pressures.

These proposed areas of research will facilitate a greater understanding of the benefits of mass transport enhancement for rate-limited chemical reactions and is likely to produce additional opportunity for catalyst-based chemical reaction applications.

REFERENCES

1. Claussen, J. C.; Artiles, M. S.; McLamore, E. S.; Mohanty, S.; Shi, J.; Rickus, J. L.; Fisher, T. S.; Porterfield, D. M. Electrochemical Glutamate Biosensing with Nanocube and Nanosphere Augmented Single-Walled Carbon Nanotube Networks: A Comparative Study. *J. Mater. Chem.* **2011**, *21*, 11224-11231.
2. Solovev, A. A.; Mei, Y.; Bermúdez Ureña, E.; Huang, G.; Schmidt, O. G. Catalytic Microtubular Jet Engines Self-Propelled by Accumulated Gas Bubbles. *Small* **2009**, *5*, 1688-1692.
3. Soler, L.; Magdanz, V.; Fomin, V. M.; Sanchez, S.; Schmidt, O. G. Self-Propelled Micromotors for Cleaning Polluted Water. *ACS Nano* **2013**, *7*, 9611-9620.
4. Sanchez, S.; Ananth, A. N.; Fomin, V. M.; Viehrig, M.; Schmidt, O. G. Superfast Motion of Catalytic Microjet Engines at Physiological Temperature. *J. Amer. Chem. Soc.* **2011**, *133*, 14860-14863.
5. Laocharoensuk, R.; Burdick, J.; Wang, J. Carbon-Nanotube-Induced Acceleration of Catalytic Nanomotors. *ACS Nano* **2008**, *2*, 1069-1075.
6. Ke, H.; Ye, S.; Carroll, R. L.; Showalter, K. Motion Analysis of Self-Propelled Pt−Silica Particles in Hydrogen Peroxide Solutions. *J. Phys. Chem. A* **2010**, *114*, 5462-5467.
7. Campuzano, S.; Orozco, J.; Kagan, D.; Guix, M.; Gao, W.; Sattayasamitsathit, S.; Claussen, J. C.; Merkoçi, A.; Wang, J. Bacterial Isolation by Lectin-Modified Microengines. *Nano Lett.* **2011**, *12*, 396-401.
8. Sattayasamitsathit, S.; Gu, Y.; Kaufmann, K.; Jia, W.; Xiao, X.; Rodriguez, M.; Minteer, S.; Cha, J.; Burckel, D. B.; Wang, C.; Polsky, R.; Wang, J. Highly Ordered Multilayered 3D Graphene Decorated with Metal Nanoparticles. *J. Mater. Chem. A* **2013**, *1*, 1639-1645.
9. Chen, Z.; Ren, W.; Gao, L.; Liu, B.; Pei, S.; Cheng, H.-M. Three-dimensional flexible and conductive interconnected graphene networks grown by chemical vapour deposition. *Nat. Mater.* **2011**, *10*, 424-428.
10. Claussen, J. C.; Kumar, A.; Jaroch, D. B.; Khawaja, M. H.; Hibbard, A. B.; Porterfield, D. M.; Fisher, T. S. Nanostructuring Platinum Nanoparticles on Multilayered Graphene Petal Nanosheets for Electrochemical Biosensing. *Adv. Funct. Mater.* **2012**, *22*, 3399-3405.
11. Meshkani, F.; Rezaei, M. Nickel catalyst supported on magnesium oxide with high surface area and plate-like shape: A highly stable and active catalyst in methane reforming with carbon dioxide. *Catal. Commun.* **2011**, *12*, 1046-1050.
12. Bartley, J. K.; Xu, C.; Lloyd, R.; Enache, D. I.; Knight, D. W.; Hutchings, G. J. Simple method to synthesize high surface area magnesium oxide and its use as a heterogeneous base catalyst. *Appl. Catal., B* **2012**, *128*, 31-38.

13. Rezaei, M.; Khajenoori, M.; Nematollahi, B. Synthesis of high surface area nanocrystalline MgO by pluronic P123 triblock copolymer surfactant. *Powder Technol.* **2011**, *205*, 112-116.
14. Hu, S.; Gong, Y.; Xu, Q.; Liu, X.; Zhang, Q.; Zhang, L.; Dou, T. Highly selective formation of propylene from methanol over high-silica EU-1 zeolite catalyst. *Catal. Commun.* **2012**, *28*, 95-99.
15. Liu, P.; Wang, J.; Wei, R.; Ren, X.; Zhang, X. A Highly Efficient Hβ Zeolite Supported Pt Catalyst Promoted by Chromium for the Hydroisomerization of n-Heptane. *Catal. Lett.* **2008**, *126*, 346-352.
16. Parsafard, N.; Peyrovi, M. H.; Rashidzadeh, M. n-Heptane isomerization on a new kind of micro/mesoporous catalyst: Pt supported on HZSM-5/HMS. *Microporous Mesoporous Mater.* **2014**, *200*, 190-198.
17. Ginoza, T.; Okamura, K.; Fukuda, J.; Suzuki, H. In *Improvement of detection sensitivity using electrodes with micropillar structures*, Solid-State Sensors, Actuators and Microsystems Conference, 2009. TRANSDUCERS 2009. International, **2009**.
18. Guo, M.-m.; Xia, Y.; Huang, W.; Li, Z. Electrochemical fabrication of stalactite-like copper micropillar arrays via surface rebuilding for ultrasensitive nonenzymatic sensing of glucose. *Electrochim. Acta* **2015**, *151*, 340-346.
19. Schröper, F.; Brüggemann, D.; Mourzina, Y.; Wolfrum, B.; Offenhäusser, A.; Mayer, D. Analyzing the electroactive surface of gold nanopillars by electrochemical methods for electrode miniaturization. *Electrochim. Acta* **2008**, *53*, 6265-6272.
20. Forrer, P.; Schlottig, F.; Siegenthaler, H.; Textor, M. Electrochemical preparation and surface properties of gold nanowire arrays formed by the template technique. *J. Appl. Electrochem.* **2000**, *30*, 533-541.
21. Ekanayake, E. M. I. M.; Preethichandra, D. M. G.; Kaneto, K. Polypyrrole nanotube array sensor for enhanced adsorption of glucose oxidase in glucose biosensors. *Biosens. Bioelectron.* **2007**, *23*, 107-113.
22. Claussen, J. C.; Hengenius, J. B.; Wickner, M. M.; Fisher, T. S.; Umulis, D. M.; Porterfield, D. M. Effects of carbon nanotube-tethered nanosphere density on amperometric biosensing: Simulation and experiment. *J. Phys. Chem. C* **2011**, *115*, 20896-20904.
23. Chakraborty, S.; Retna Raj, C. Pt nanoparticle-based highly sensitive platform for the enzyme-free amperometric sensing of H2O2. *Biosens. Bioelectron.* **2009**, *24*, 3264-3268.
24. Wang, J.; Wang, Z.; Zhao, D.; Xu, C. Facile fabrication of nanoporous PdFe alloy for nonenzymatic electrochemical sensing of hydrogen peroxide and glucose. *Anal. Chim. Acta* **2014**, *832*, 34-43.
25. Marr, K. M.; Chen, B.; Mootz, E. J.; Geder, J.; Pruessner, M.; Melde, B. J.; Vanfleet, R. R.; Medintz, I. L.; Iverson, B. D.; Claussen, J. C. High Aspect Ratio, Carbon Nanotube Membranes Decorated with Pt Nanoparticle Urchins for Micro Underwater Vehicle Propulsion via H2O2 Decomposition. **2015**, *10.1021/acsnano.5b02124*.
26. Bian, X. J.; Qian, K.; Liao, L.; Zhou, X. F.; Guo, K.; Huang, X. D.; Yu, C. Z.; Ji, C.; Liu, B. H. Platinum Nanoparticles Supported on Hierarchical Carbon Foams for Electrocatalytic Oxidation of Methanol. *ECS Electrochem. Lett.* **2014**, *3*, F11-F14.
27. Xue, H.; Li, H.; Yi, Y. U.; Hu, H. ORDERED POROUS ANODIC ALUMINUM OXIDE FILMS MADE BY TWO-STEP ANODIZATION. *Surf. Rev. Lett.* **2007**, *14*, 1039-1045.
28. Vojkuvka, L.; Marsal, L. F.; Pallare; x; s, J. In *Study of Porous Alumina Porosity after Pore Widening Process*, Electron Devices, 2007 Spanish Conference on, **2007**.

29. Lee, W.; Ji, R.; Gosele, U.; Nielsch, K. Fast fabrication of long-range ordered porous alumina membranes by hard anodization. *Nat. Mater.* **2006**, *5*, 741-747.
30. Nessim, G. D. Properties, synthesis, and growth mechanisms of carbon nanotubes with special focus on thermal chemical vapor deposition. *Nanoscale* **2010**, *2*, 1306-1323.
31. Shahrokhian, S.; Rastgar, S. Electrochemical deposition of gold nanoparticles on carbon nanotube coated glassy carbon electrode for the improved sensing of tinidazole. *Electrochim. Acta* **2012**, *78*, 422-429.
32. Rakhi, R. B.; Sethupathi, K.; Ramaprabhu, S. A Glucose Biosensor Based on Deposition of Glucose Oxidase onto Crystalline Gold Nanoparticle Modified Carbon Nanotube Electrode. *J. Phys. Chem. B* **2009**, *113*, 3190-3194.
33. Hutchison, D. N.; Morrill, N. B.; Aten, Q.; Turner, B. W.; Jensen, B. D.; Howell, L. L.; Vanfleet, R. R.; Davis, R. C. Carbon Nanotubes as a Framework for High-Aspect-Ratio MEMS Fabrication. *J. Microelectromech. Syst.* **2010**, *19*, 75-82.
34. Song, J.; Jensen, D. S.; Hutchison, D. N.; Turner, B.; Wood, T.; Dadson, A.; Vail, M. A.; Linford, M. R.; Vanfleet, R. R.; Davis, R. C. Carbon-Nanotube-Templated Microfabrication of Porous Silicon-Carbon Materials with Application to Chemical Separations. *Adv. Funct. Mater.* **2011**, *21*, 1132-1139.
35. Cho, Y.-R.; Lee, J. H.; Song, Y.-H.; Kang, S.-Y.; Hwang, C.-S.; Jung, M.-Y.; Kim, D.-H.; Lee, S.-K.; Uhm, H.-S.; Cho, K. I. Photolithography-Based Carbon Nanotubes Patterning for Field Emission Displays. *Mater. Sci. Eng. B* **2001**, *79*, 128-132.
36. Zhang, L.; Shi, T.; Xi, S.; Liu, D.; Tang, Z.; Li, X.; Lai, W. Carbon Nanotube Integrated 3-Dimensional Carbon Microelectrode Array by Modified SU-8 Photoresist Photolithography and Pyrolysis. *Thin Solid Films* **2011**, *520*, 1041-1047.
37. Tasaltin, C.; Basarir, F. Preparation of Flexible VOC Sensor Based on Carbon Nanotubes and Gold Nanoparticles. *Sens. Actuators, B* **2014**, *194*, 173-179.
38. Maruyama, S.; Xiang, R. Chemical Vapor Deposition Growth, Optical, and Thermal Characterization of Vertically Aligned Single-Walled Carbon Nanotubes. *J. Heat Transfer* **2012**, *134*, 1-6.
39. Claussen, J. C.; Franklin, A. D.; Haque, A. U.; Marshall Porterfield, D.; Fisher, T. S. Electrochemical Biosensor of Nanocube-Augmented Carbon Nanotube Networks. *ACS Nano* **2009**, *3*, 37-44.
40. Amama, P. B.; Ogebule, O.; Maschmann, M. R.; Sands, T. D.; Fisher, T. S. Dendrimer-Assisted Low-Temperature Growth of Carbon Nanotubes by Plasma-Enhanced Chemical Vapor Deposition. *Chem. Commun.* **2006**, 2899-2901.
41. Choi, Y. C.; Shin, Y. M.; Lee, Y. H.; Lee, B. S.; Park, G.-S.; Choi, W. B.; Lee, N. S.; Jong-Min, K. Controlling the Diameter, Growth Rate, and Density of Vertically Aligned Carbon Nanotubes Synthesized by Microwave Plasma-Enhanced Chemical Vapor Deposition. *Appl. Phys. Lett.* **2000**, *76*, 2367-2369.
42. Peng, Y.; Hu, Y.; Wang, H. Patterned Deposition of Multi-Walled Carbon Nanotubes on Self-Assembled Monolayers. *Chin. Sci. Bull.* **2006**, *51*, 147-150.
43. Lalwani, G.; Kwaczala, A. T.; Kanakia, S.; Patel, S. C.; Judex, S.; Sitharaman, B. Fabrication and Characterization of Three-Dimensional Macroscopic All-Carbon Scaffolds. *Carbon* **2013**, *53*, 90-100.
44. Hsueh, Y.-C.; Wang, C.-C.; Liu, C.; Kei, C.-C.; Perng, T.-P. Deposition of platinum on oxygen plasma treated carbon nanotubes by atomic layer deposition. *Nanotechnology* **2012**, *23*, 405603.

45. Dameron, A. A.; Pylypenko, S.; Bult, J. B.; Neyerlin, K. C.; Engtrakul, C.; Bochert, C.; Leong, G. J.; Frisco, S. L.; Simpson, L.; Dinh, H. N.; Pivovar, B. Aligned carbon nanotube array functionalization for enhanced atomic layer deposition of platinum electrocatalysts. *Appl. Surf. Sci.* **2012**, *258*, 5212-5221.
46. Leskela, M.; Ritala, M. Atomic layer deposition chemistry: recent developments and future challenges. *Angew. Chem. Int. Ed. (English)* **2003**, *42*, 5548-54.
47. Yun, Y.; Dong, Z.; Shanov, V. N.; Doepke, A.; Heineman, W. R.; Halsall, H. B.; Bhattacharya, A.; Wong, D. K. Y.; Schulz, M. J. Fabrication and characterization of carbon nanotube array electrodes with gold nanoparticle tips. *Sensor. Actuat. B-Chem.* **2008**, *133*, 208-212.
48. Song, Y.-Z.; Zhu, A.-F.; Zhong, H.; Song, Y.; Wu, F.-Y.; Yang, W.-l.; Huang, H. Gold nanoparticle/single-walled carbon nanotube film on the surface of glassy carbon electrode and its application. *Mater. Lett.* **2011**, *65*, 3612-3614.
49. Meng, H.; Xie, F.; Chen, J.; Sun, S.; Shen, P. K. Morphology Controllable Growth of Pt Nanoparticles/Nanowires on Carbon Powders and its Application as Novel Electro-Catalyst for Methanol Oxidation. *Nanoscale* **2011**, *3*, 5041-5048.
50. Sun, S.; Jaouen, F.; Dodelet, J.-P. Controlled Growth of Pt Nanowires on Carbon Nanospheres and Their Enhanced Performance as Electrocatalysts in PEM Fuel Cells. *Adv. Mater.* **2008**, *20*, 3900-3904.
51. Nores-Pondal, F. J.; Vilella, I. M. J.; Troiani, H.; Granada, M.; de Miguel, S. R.; Scelza, O. A.; Corti, H. R. Catalytic activity vs. size correlation in platinum catalysts of PEM fuel cells prepared on carbon black by different methods. *Int. J. Hydrogen Energy* **2009**, *34*, 8193-8203.
52. Sun, S.; Yang, D.; Zhang, G.; Sacher, E.; Dodelet, J.-P. Synthesis and Characterization of Platinum Nanowire–Carbon Nanotube Heterostructures. *Chem. Mater.* **2007**, *19*, 6376-6378.
53. Sun, S.; Zhang, G.; Geng, D.; Chen, Y.; Banis, M. N.; Li, R.; Cai, M.; Sun, X. Direct Growth of Single-Crystal Pt Nanowires on Sn@CNT Nanocable: 3D Electrodes for Highly Active Electrocatalysts. *Chem. Eur. J.* **2010**, *16*, 829-835.
54. Soleymani, L. Programming the detection limits of biosensors through controlled nanostructuring. *Nature* **2009**.
55. Soleymani, L.; Fang, Z.; Sun, X.; Yang, H.; Taft, B. J.; Sargent, E. H.; Kelley, S. O. Nanostructuring of Patterned Microelectrodes To Enhance the Sensitivity of Electrochemical Nucleic Acids Detection. *Angew. Chem., Int. Ed.* **2009**, *48*, 8457-8460.
56. Yao, Z.; Zhu, M.; Jiang, F.; Du, Y.; Wang, C.; Yang, P. Highly Efficient Electrocatalytic Performance Based on Pt Nanoflowers Modified Reduced Graphene Oxide/Carbon Cloth Electrode. *J. Mater. Chem.* **2012**, *22*, 13707-13713.
57. Claussen, J. C.; Daniele, M. A.; Geder, J.; Pruessner, M.; Makinen, A. J.; Melde, B. J.; Twigg, M.; Verbarg, J. M.; Medintz, I. L. Platinum-Paper Micromotors: An Urchin-Like Nanohybrid Catalyst for Green Monopropellant Bubble-Thrusters. *ACS Appl. Mater. Interfaces* **2014**, *6*, 17837-17847.
58. Hanna, B. H.; Fazio, W. C.; J.D., T.; Lund, J. M.; Wood, T. S.; Davis, R. C.; Vanfleet, R. R.; Jensen, B. D. Mechanical Property Measurement of Carbon Infiltrated Carbon Nanotube Structures for Compliant Micromechanisms. *J. Microelectromech. Syst.* **2014**, *23*, 1330-1339.

59. Wang, S. C.; Chang, K. S.; Yuan, C. J. Enhancement of Electrochemical Properties of Screen-Printed Carbon Electrodes by Oxygen Plasma Treatment. *Electrochim. Acta* **2009**, *54*, 4937-4943.
60. Ovejero, G.; Sotelo, J. L.; Romero, M. D.; Rodríguez, A.; Ocaña, M. A.; Rodríguez, G.; García, J. Multiwalled Carbon Nanotubes for Liquid-Phase Oxidation. Functionalization, Characterization, and Catalytic Activity. *Ind. Eng. Chem. Res.* **2006**, *45*, 2206-2212.
61. Xin, Y.; Fujimoto, T.; Uyama, H. Facile Fabrication of Polycarbonate Monolith by Non-Solvent Induced Phase Separation Method. *Polymer* **2012**, *53*, 2847-2853.
62. Bazargan, A. M.; Keyanpour-rad, M.; Hesari, F. A.; Ganji, M. E. A Study on the Microfiltration Behavior of Self-Supporting Electrospun Nanofibrous Membrane in Water Using an Optical Particle Counter. *Desalination* **2011**, *265*, 148-152.
63. Kroll, S.; de Moura, M. O. C.; Meder, F.; Grathwohl, G.; Rezwan, K. High Virus Retention Mediated by Zirconia Microtubes with Tailored Porosity. *J. Eur. Ceram. Soc.* **2012**, *32*, 4111-4120.
64. Lu, S. H.; Ni Tun, M. H.; Mei, Z. J.; Chia, G. H.; Lim, X.; Sow, C.-H. Improved Hydrophobicity of Carbon Nanotube Arrays with Micropatterning. *Langmuir* **2009**, *25*, 12806-12811.
65. Wang, H. Z.; Huang, Z. P.; Cai, Q. J.; Kulkarni, K.; Chen, C. L.; Carnahan, D.; Ren, Z. F. Reversible Transformation of Hydrophobicity and Hydrophilicity of Aligned Carbon Nanotube Arrays and Buckypapers by Dry Processes. *Carbon* **2010**, *48*, 868-875.
66. Mathur, A.; Roy, S. S.; Hazra, K. S.; Wadhwa, S.; Ray, S. C.; Mitra, S. K.; Misra, D. S.; McLaughlin, J. A. Oxygen Plasma Assisted End-Opening and Field Emission Enhancement in Vertically Aligned Multiwall Carbon Nanotubes. *Mater. Chem. Phys.* **2012**, *134*, 425-429.
67. Li, P.; Lim, X.; Zhu, Y.; Yu, T.; Ong, C.-K.; Shen, Z.; Wee, A. T.-S.; Sow, C.-H. Tailoring Wettability Change on Aligned and Patterned Carbon Nanotube Films for Selective Assembly. *J. Phys. Chem. B* **2007**, *111*, 1672-1678.
68. Dai, X.; Huang, X.; Yang, F.; Li, X.; Sightler, J.; Yang, Y.; Li, C. Enhanced Nucleate Boiling on Horizontal Hydrophobic-Hydrophilic Carbon Nanotube Coatings. *Appl. Phys. Lett.* **2013**, *102*, 1-5.
69. Li, H.; Geng, H.-Z.; Meng, Y.; Wang, Y.; Xu, X.-B.; Ding, E.-X.; Gao, J.; Chen, L.-T.; Ma, S. Fabrication and Test of Adhesion Enhanced Flexible Carbon Nanotube Transparent Conducting Films. *Appl. Surf. Sci.* **2014**, *313*, 220-226.
70. Chen, J.; Chen, Q.; Ma, Q. Influence of Surface Functionalization via Chemical Oxidation on the Properties of Carbon Nanotubes. *J. Colloid Interface Sci.* **2012**, *370*, 32-38.
71. Huang, J.-Q.; Zhang, Q.; Zhao, M.-Q.; Xu, G.-H.; Wei, F. Patterning of Hydrophobic Three-Dimensional Carbon Nanotube Architectures by a Pattern Transfer Approach. *Nanoscale* **2010**, *2*, 1401-1404.
72. Burton, Z.; Bhushan, B. Hydrophobicity, Adhesion, and Friction Properties of Nanopatterned Polymers and Scale Dependence for Micro- and Nanoelectromechanical Systems. *Nano Lett.* **2005**, *5*, 1607-1613.
73. Tsen, S. C. Y.; Crozier, P. A.; Liu, J. Lattice Measurement and Alloy Compositions in Metal and Bimetallic Nanoparticles. *Ultramicroscopy* **2003**, *98*, 63-72.
74. Kwak, D.-H.; Lee, Y.-W.; Lee, K.-H.; Park, A.-R.; Moon, J.-S.; Park, K.-W. One-Step Synthesis of Hexapod Pt Nanoparticles Deposited on Carbon Black for Improved Methanol Electrooxidation. *Int. J. Electrochem. Sci.* **2013**, *8*, 5102-5107.

75. Chen, E.; Sheng-wei, H.; Wei-Han, W.; Jen-Hwa, G. In *Side Scan Sonar Grid Map for Unmanned Underwater Vehicle Navigation*, OCEANS, Waikoloa, Institute of Electrical and Electronics Engineers: **2011**.
76. Mohseni, K. Pulsatile Vortex Generators for Low-Speed Maneuvering of Small Underwater Vehicles. *Ocean Eng.* **2006**, *33*, 2209-2223.
77. Kodati, P. *Biomimetic Micro Underwater Vehicle with Ostraciiform Locomotion: System Design, Analysis and Experiments*. ProQuest: Ann Arbor, 2006; pp 1-2.
78. Crimmins, D. M.; Patty, C. T.; Beliard, M. A.; Baker, J.; Jalbert, J. C.; Komerska, R. J.; Chappell, S. G.; Blidberg, D. R. In *Long-Endurance Test Results of the Solar-Powered AUV System*, OCEANS, Boston, Institute of Electrical and Electronics Engineers: **2006**.
79. Hobson, B. W.; Bellingham, J. G.; Kieft, B.; McEwen, R.; Godin, M.; Yanwu, Z. In *Tethys-Class Long Range AUVs - Extending the Endurance of Propeller-Driven Cruising AUVs from Days to Weeks*, Autonomous Underwater Vehicles (AUV), Southampton, The Insitute of Electrical and Electronics Engineers Oceanic Engineering Society: **2012**.
80. Hyakudome, T.; Tsukioka, S.; Yoshida, H.; Sawa, T.; Ishibashi, S.; Ishikawa, A.; Ishiwata, J.; Watanabe, K.; Nakamura, M.; Aoki, T. In *Autonomous Underwater Vehicle for Surveying Deep Ocean*, Institute of Electrical and Electronics Engineers International Conference on, Gippsland, Institute of Electrical and Electronics Engineers: **2009**.
81. Rusek, J. J. In *Hydrogen Peroxide for Propulsion and Power Applications: A Swift Perspective*, 2nd International Conference on Green Propellants for Space Propulsion, Sardinia, European Space Agency: **2004**.
82. Kim, J.; Nam, D.-G.; Oh, W. Electrochemical Oxidations of Alcohols on Platinum/Carbon Nanotube Composites. *Trans. Electr. Electron. Mater.* **2013**, *14*, 125-129.
83. Watt, G. D. Kinetic Evaluation of the Viologen-Catalyzed Carbohydrate Oxidation Reaction for Fuel Cell Application. *Renew. Energ.* **2014**, *63*, 370-375.
84. Wernimont, E. J. In *Monopropellant Hydrogen Peroxide Rocket Systems: Optimum for Small Scale*, 42nd AIAA/ASME/SAE/ASEE Joint Propulsion Conference & Exhibit, Sacramento, American Institute of Aeronautics and Astronautics: **2006**.
85. Gibbs, J. G.; Zhao, Y. P. Autonomously Motile Catalytic Nanomotors by Bubble Propulsion. *Appl. Phys. Lett.* **2009**, *94*, 163104-163106.
86. Baraban, L.; Makarov, D.; Streubel, R.; Mönch, I.; Grimm, D.; Sanchez, S.; Schmidt, O. G. Catalytic Janus Motors on Microfluidic Chip: Deterministic Motion for Targeted Cargo Delivery. *ACS Nano* **2012**, *6*, 3383-3389.
87. Manesh, K. M.; Cardona, M.; Yuan, R.; Clark, M.; Kagan, D.; Balasubramanian, S.; Wang, J. Template-Assisted Fabrication of Salt-Independent Catalytic Tubular Microengines. *ACS Nano* **2010**, *4*, 1799-1804.
88. Mirkovic, T.; Zacharia, N. S.; Scholes, G. D.; Ozin, G. A. Fuel for Thought: Chemically Powered Nanomotors Out-Swim Nature's Flagellated Bacteria. *ACS Nano* **2010**, *4*, 1782-1789.
89. Gao, W.; Sattayasamitsathit, S.; Orozco, J.; Wang, J. Highly Efficient Catalytic Microengines: Template Electrosynthesis of Polyaniline/Platinum Microtubes. *J. Am. Chem. Soc.* **2011**, *133*, 11862-11864.
90. Wang, Y.; Hernandez, R. M.; Bartlett, D. J.; Bingham, J. M.; Kline, T. R.; Sen, A.; Mallouk, T. E. Bipolar Electrochemical Mechanism for the Propulsion of Catalytic Nanomotors in Hydrogen Peroxide Solutions†. *Langmuir* **2006**, *22*, 10451-10456.

91. Mei, Y.; Huang, G.; Solovev, A. A.; Ureña, E. B.; Mönch, I.; Ding, F.; Reindl, T.; Fu, R. K. Y.; Chu, P. K.; Schmidt, O. G. Versatile Approach for Integrative and Functionalized Tubes by Strain Engineering of Nanomembranes on Polymers. *Adv. Mater.* **2008**, *20*, 4085-4090.
92. Choudhary, V.; Gaikwad, A.; Sansare, S. Activation of Supported Pd Metal Catalysts for Selective Oxidation of Hydrogen to Hydrogen Peroxide. *Catal. Lett.* **2002**, *83*, 235-239.
93. Ishida, T.; Kuroda, K.; Kinoshita, N.; Minagawa, W.; Haruta, M. Direct deposition of gold nanoparticles onto polymer beads and glucose oxidation with H2O2. *J. Colloid Interface Sci.* **2008**, *323*, 105-111.
94. Frikha, N.; Schaer, E.; Houzelot, J.-L. Experimental study and modelling of thermal runaway: Application to dichromate catalysed hydrogen peroxide decomposition. *Thermochim. Acta* **2006**, *449*, 47-54.
95. Huang, H.-H.; Lu, M.-C.; Chen, J.-N. Catalytic decomposition of hydrogen peroxide and 2-chlorophenol with iron oxides. *Wat. Res.* **2001**, *35*, 2291-2299.
96. Seol, Y.; Javandel, I. Citric acid-modified Fenton's reaction for the oxidation of chlorinated ethylenes in soil solution systems. *Chemosphere* **2008**, *72*, 537-42.
97. Mededovic, S.; Locke, B. Platinum catalysed decomposition of hydrogen peroxide in aqueous-phase pulsed corona electrical discharge. *Appl. Catal., B* **2006**, *67*, 149-159.
98. Hasnat, M. A.; Rahman, M. M.; Borhanuddin, S. M.; Siddiqua, A.; Bahadur, N. M.; Karim, M. R. Efficient Hydrogen Peroxide Decomposition on Bimetallic Pt–Pd Surfaces. *Catal. Commun.* **2010**, *12*, 286-291.
99. Pina, P.; Mallada, R. An example of falsified kinetics by diffusional limitations in gas-solid catalytic reactions. *Int. J. Eng. Educ.* **2004**, *20*, 1074-1084.
100. McKee, D. W. Catalytic Decomposition of Hydrogen Peroxide by Metals and Alloys of the Platinum Group. *J. Catal.* **1969**, *14*, 355-364.
101. Wang, Z.; Lv, X.; Weng, J. High Peroxidase Catalytic Activity of Exfoliated Few-Layer Graphene. *Carbon* **2013**, *62*, 51-60.
102. Klaewkla, R.; Arend, M.; Hoelderich, W. F. A Review of Mass Transfer Controlling the Reaction Rate in Heterogeneous Catalytic Systems. In *Mass Transfer - Advanced Aspects*, Nakajima, H., InTech: **2011**; pp 667-684.
103. Watson, S. A.; Green, P. N. In *Propulsion Systems for Micro-Autonomous Underwater Vehicles (μAUVs)*, Robotics Automation and Mechatronics (RAM), 2010 IEEE Conference on, Singapore, Institute of Electrical and Electronics Engineers: **2010**.
104. Kopman, V.; Porfiri, M. Design, Modeling, and Characterization of a Miniature Robotic Fish for Research and Education in Biomimetics and Bioinspiration. *IEEE/ASME Trans. Mechatronics* **2013**, *18*, 471-483.
105. Aureli, M.; Kopman, V.; Porfiri, M. Free-Locomotion of Underwater Vehicles Actuated by Ionic Polymer Metal Composites. *IEEE/ASME Trans. Mechatronics* **2010**, *15*, 603-614.
106. Hubbard, J. J.; Fleming, M.; Palmre, V.; Pugal, D.; Kim, K. J.; Leang, K. K. Monolithic IPMC Fins for Propulsion and Maneuvering in Bioinspired Underwater Robotics. *IEEE J. Oceanic Eng.* **2014**, *39*, 540-551.
107. Zhengbao, Y.; Yukui, W.; Fei, G.; Zhenlong, W.; Yangwei, W. In *Study on the hydrodynamics and kinematics of a biomimetic fin propulsor actuated by SMA wires*, Electronic and Mechanical Engineering and Information Technology (EMEIT), 2011 International Conference on, Institute of Electrical and Electronics Engineers: **2011**.
108. American Diabetes Association. Diabetes statistics. http://www.diabetes.org/diabetes-basics/diabetes-statistics/ (accessed August 22, 2013).

109. Wang, J. Electrochemical Glucose Biosensors. *Chem. Rev.* **2007**, *108*, 814-825.
110. Kumar, S. A.; Cheng, H.-W.; Chen, S.-M.; Wang, S.-F. Preparation and characterization of copper nanoparticles/zinc oxide composite modified electrode and its application to glucose sensing. *Mater. Sci. Eng. C, Mater. Biol. Appl.* **2010**, *30*, 86-91.
111. Ye, D.; Liang, G.; Li, H.; Luo, J.; Zhang, S.; Chen, H.; Kong, J. A novel nonenzymatic sensor based on CuO nanoneedle/graphene/carbon nanofiber modified electrode for probing glucose in saliva. *Talanta* **2013**, *116*, 223-230.
112. Montornes, J. M.; Vreeke, M. S.; Katakis, I. Glucose Biosensors. In *Bioelectrochemistry*, John Wiley & Sons, Ltd: 2008; pp 199-217.
113. Hall, S. B.; Khudaish, E. A.; Hart, A. L. Electrochemical oxidation of hydrogen peroxide at platinum electrodes. Part 1. An adsorption-controlled mechanism. *Electrochim. Acta* **1998**, *43*, 579-588.
114. Rivas, G. A.; Rubianes, M. D.; Rodríguez, M. C.; Ferreyra, N. F.; Luque, G. L.; Pedano, M. L.; Miscoria, S. A.; Parrado, C. Carbon nanotubes for electrochemical biosensing. *Talanta* **2007**, *74*, 291-307.
115. Ammam, M.; Easton, E. B. High-performance glucose sensor based on glucose oxidase encapsulated in new synthesized platinum nanoparticles supported on carbon Vulcan/Nafion composite deposited on glassy carbon. *Sensor. Actuat. B-Chem.* **2011**, *155*, 340-346.
116. Claussen, J. C.; Wickner, M. M.; Fisher, T. S.; Porterfield, D. M. Transforming the fabrication and biofunctionalization of gold nanoelectrode arrays into versatile electrochemical glucose biosensors. *ACS Appl. Mater. Interfaces* **2011**, *3*, 1765-1770.
117. Liu, X.; Peng, Y.; Qu, X.; Ai, S.; Han, R.; Zhu, X. Multi-walled carbon nanotube-chitosan/poly(amidoamine)/DNA nanocomposite modified gold electrode for determination of dopamine and uric acid under coexistence of ascorbic acid. *J. Electroanal. Chem.* **2011**, *654*, 72-78.
118. Cyclic Voltammetry. http://en.wikipedia.org/wiki/Cyclic_voltammetry (accessed 27 May, 2015).
119. Shi, J.; Claussen, J. C.; McLamore, E. S.; Ul Haque, A.; Jaroch, D.; Diggs, A. R.; Calvo-Marzal, P.; Rickus, J. L.; Marshall Porterfield, D. A Comparative Study of Enzyme Immobilization Strategies for Multi-Walled Carbon Nanotube Glucose Biosensors. *Nanotechnology* **2011**, *22*, 1-10.
120. Skoog, D. A. Voltammetry. In *Principles of Instrumental Analysis*, 6th ed.; Thomson Brooks/Cole: Belmont, 2007; pp 737-742.
121. Liu, B.; Wang, M. Preparation and Characterization of Size-Controlled Silver Nanoparticles Decorated Multi-Walled Carbon Nanotubes and their Electrocatalytic Reduction Properties for Hydrogen Peroxide. *Russ. J. Electrochem.* **2014**, *50*, 476-481.
122. Yang, G.-W.; Gao, G.-Y.; Wang, C.; Xu, C.-L.; Li, H.-L. Controllable Deposition of Ag Nanoparticles on Carbon Nanotubes as a Catalyst for Hydrazine Oxidation. *Carbon* **2008**, *46*, 747-752.
123. Guo, D.-J.; Li, H.-L. High Dispersion and Electrocatalytic Properties of Palladium Nanoparticles on Single-Walled Carbon Nanotubes. *J. Colloid Interface Sci.* **2005**, *286*, 274-279.

APPENDIX A. CNT-MM DESIGN MATERIAL

A.1 Mask Design Tutorial (KLayout)

Preface: This tutorial is designed to guide the user through the basic mask fabrication process using AutoCAD and KLayout programs as applies to BYU facilities. Due to the wider availability of AutoCAD tutorials and customer support, the main focus here will be on the usage of KLayout. KLayout is introduced here as a means to more quickly manipulate large file sizes and prepare the file for the actual mask creation.

Preparation:

Access to AutoCAD (or another program that can export as a DXF)
Download KLayout (http://www.klayout.de/build.html)
A computer with at least 8GB of RAM (RGS blade is sufficient)

1. **Go to:**
   http://www.cleanroom.byu.edu/mask_fab.phtml
   a. Become familiar with best practices for mask designing and the capabilities of laser printing here on campus. Especially note the different resolution laser tips.
2. **AutoCAD:**
   a. It is much easier to define and constrain the basic geometry relationships in AutoCAD as opposed to KLayout (although some basic operations are possible there).
   b. Make the design modularly in sections if possible, import the various parts of the cell (completed unit to be repeated on the mask) from separate files. This helps provide quicker access to backups in case of a crash or memory overload (which are both very likely when working with a high number of geometries). The geometries for our example are shown in Figure A-1.
   c. Make sure your geometry is correct as it will be nearly impossible to fix it after the following step.
   d. After defining and positioning the geometries as desired, use the "join" or "unite" command to connect arcs, splines, and lines into single polylines. By doing this, the geometry is saved as it appears on the screen and that everything is tied together.
      i. Be sure to unite the geometry as early as possible before patterning, given that memory and other issues will surface later when trying to join too many objects simultaneously.
      ii. Uniting destroys all previous geometrical constraints (parallel, perpendicular, *etc*.) as well as set dimensional constraints making the file smaller and more manageable.

e. After the basic geometries are created and imported together, (in this case the "Big Circle Pattern" was imported into the "Circle Tab Unpatterned" file), select the "Duplicate" command, pick the reference point you wish to use and the geometry you wish to pattern (the "Big Circle Pattern") and copy as many sets of the geometry as desired.
    i. Highlighting the selection before selecting "Duplicate" is harder on the memory and can cause lag for larger copy groups.
    ii. Terminate the "Duplicate" command periodically, allowing AutoCAD to process the change, allow you to select a bigger/different geometry set, and to save your work.
    iii. Be sure not to overlap identical geometries by using clever reference points. This makes deleting individual shapes easier and minimizes memory usage and confusion later.
f. Once your geometry and all other respective cleanup operations are complete, save your file as a DXF file type. Varying the save parameters will affect the resolution of the final image. As always, make the file as small as is possible.

3. KLayout:

a. Open your DXF and check the resolution of circles, the scale, and general completeness (with some settings, parts get simplified out of existence).
b. Save the new file as a type GDS2 *file* (not a GDS2 *text*), varying the parameters until the size is as small as possible while maintaining functional details.
    i. It might be possible to use other file types, but GDS2 is the most compatible with the mask printing software and will help avoid formatting issues later.
    ii. GDS2 files greater than roughly 2GB are likely to have problems during printing and the actual mask creation. Generally, however, the default GDS2 save values are acceptable.
    iii. To save periodically, you must select File > Save. Ctrl + S doesn't work.
    iv. Sometimes after working on a part it won't be possible to open it again due to memory overload. Using the "Save As" function, and renaming your file, allows you to go back and open the part. Completing the file in one sitting works the best. Saving as a GDS2 significantly increases your file size making the following steps more memory intensive.
c. Ensure that the figure is oriented properly with respect to the origin/grid system.
    i. To correct alignment issues double click on the outermost geometry (the background in this case; Figure A-2) to pull up the information window giving its coordinates and determine which one must be zeroed. In this case it was the first coordinate. Copy the coordinates of the point to be zeroed.
    ii. If the alignment is off it will be more complicated to pattern your cell on the mask later.
d. Select the entire workpiece (If your part is too big you will have to repeat this step with chunks of geometry at a time, moving each individually). Then click on Edit > Selection > Move By. A window will pop up in which you can paste and invert the copied values from the previous step to adjust the image.

e. Decide which features should be chrome plated and which are to be etched away by the laser.
    i. It is not possible to change the shaded appearance of some geometry groups in the software if there are too many features (all of the micron-scale circles in this case). Instead, it is easiest to have those features remain shaded on their own layer. Normally, the shaded features will be those where the chrome is removed although this can be inverted for the entire mask in the mask printing software.
f. Managing layers. The final goal of this step is to move all geometries which are desired to be chrome (or clear) onto one layer with only blank space around them.
    i. The bottom two layers have no useful purpose other than to confuse us and the laser operators. Delete them by highlighting them > right mouse click > Delete Layer Entry.
    ii. To begin, create a few working layers which you can move things onto by clicking on Edit > Layer > New Layer until the desired number of layers is attained. Layer numbers and names aren't very important, but must all be different.
    iii. Select the geometry immediately surrounding the most complicated or numerous shape. In this case it is the shape which contains all of the small circles, labelled in Figure A-3 as the "Outline". With the shape still selected, select the layer you wish to move it to. With the shape and its target layer selected, click Edit > Selection > Change Layer. Repeat this process to break all but the most memory intensive layers off of the main 0/0 layer as shown in Figure A-3.
    iv. To subtract the layers, and thereby alternating the chrome and blank spaces, select Edit > Layer > Boolean Operations. From this window you will be able to select which layers you would like to subtract, add, *etc*. with the changes being saved to the "Result" layer. This operation was done in Figure A-4 and the "BackGround" layer was then deleted as shown in Figure A-5. Repeat this process until the shaded and blank regions are properly staggered and alternating.
g. Polygons and other KLayout manipulations
    i. While AutoCAD is better for complicated geometries and patterns, KLayout does have some functionality in that respect, allowing you to finalize your design. For example: if we were to print the above geometries as is, there would be no border lines to differentiate between the different cells when patterned together on a mask.
    ii. To make a border, we will draw two squares on separate layers and subtract them from each other and finally from the "Outline" layer.
    iii. Select the layer to be drawn on, and make sure the "Background Combination Mode" is set to "Add", click on "Box" and draw a square near the edge, but inside, of your object. Repeat this with a second smaller square on a separate layer (Figure A-6).
    iv. Finally subtract the layers from each other as shown in step f-iv, and afterwards delete the unneeded layers as shown in Figure A-7.

v. Combine all geometries onto one layer by the same process used in step f-iii changing the layers of the simplest shapes onto that of the most memory intensive one.

4. Work Order

a. To send your file off to be printed, an excel sheet order form is found on the cleanroom website on the link in step 1. Fill out this form and send it to Joseph Bussio (Joe) with your mask to be printed.
   i. Given the size of the files, it is easiest to save them to a jump drive and physically deliver them to the EE shop on the 4th floor of the Clyde building. However, other methods are also acceptable.
b. Talk with Joe before actually printing your mask to make sure that the layering and patterning are done how you planned them to be. It is also helpful to be present when your file is uploaded to the printer to answer any last minute questions the operators may have.
c. Expect around 1 week of actual printing time. The mask pictured in Figure A-8 cost about $300, with costs varying on laser specifications as stated on the cleanroom website.

5. Clean the mask:

a. When the mask is finished it will be covered with bits and pieces of photoresist and chrome from the printing process as shown in Figure A-9.
b. A good primary way to clean the mask is first with copious amounts acetone and IPA, making sure to remove any residual chemicals when finished.
c. However, if the mask cannot be cleaned immediately after printing, it will probably be necessary to use nanostrip to remove the residual dried resist.
   i. Using nanostrip requires acid bench training which can be obtained by contacting Jim Fraser. Jim is also helpful if a nanostrip process plan, beyond that which is provided here, is desired.
   ii. Fill a shallow dish with nanostrip to where the acid rises about ½" above the mask.
   iii. Be sure to carefully place the mask chrome side down and avoid scratching the surface. (the chrome side is the silver colored one). By putting the chrome side down, the released photoresist will fall to the bottom of the dish rather than back onto the mask.
   iv. The chrome plating on the mask is fairly resistant to nanostrip and, as such, the mask can be exposed ranging anywhere from 10 minutes to about 2 hours if necessary. The mask shown in Figure A-9 was soaked for about 10 minutes.
d. Examine the mask for defects and check for sufficient removal of photoresist.

Start the photolithography!

KLayout Tips and Tricks:

Scrolling on the mouse will adjust the zoom
Clicking the scroll button will move the viewing window
Double click on a layer to hide/show its contents
Double click on polygons to edit their dimensions and placement.
Use the ruler tool to check dimensions (units in microns).

Use “Open In Same Panel” option to combine various DXFs.

An overflow error will result if memory allocations are exceeded with any operation.

Helpful Contacts:

Joseph Bussio
Staff Contact
joseph_bussio@byu.edu

Jim Fraser
Lab Manager
(801) 422-4344
cleanroom_manager@byu.edu

Chad Rogers
PhD Candidate
(801) 682-6761
chadirogers@gmail.com

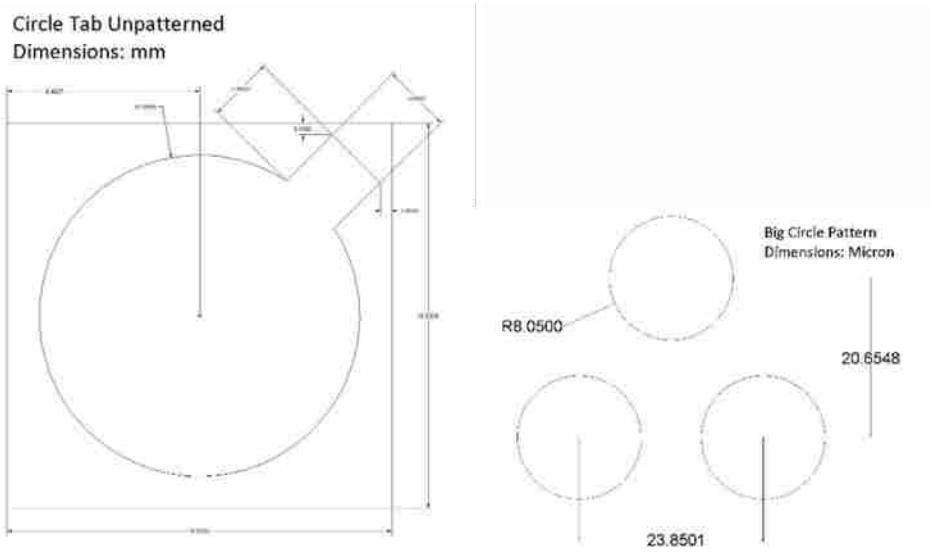

Figure A-1: Circle tab cell with a separate file for the respective “Big circle pattern” to fill it.

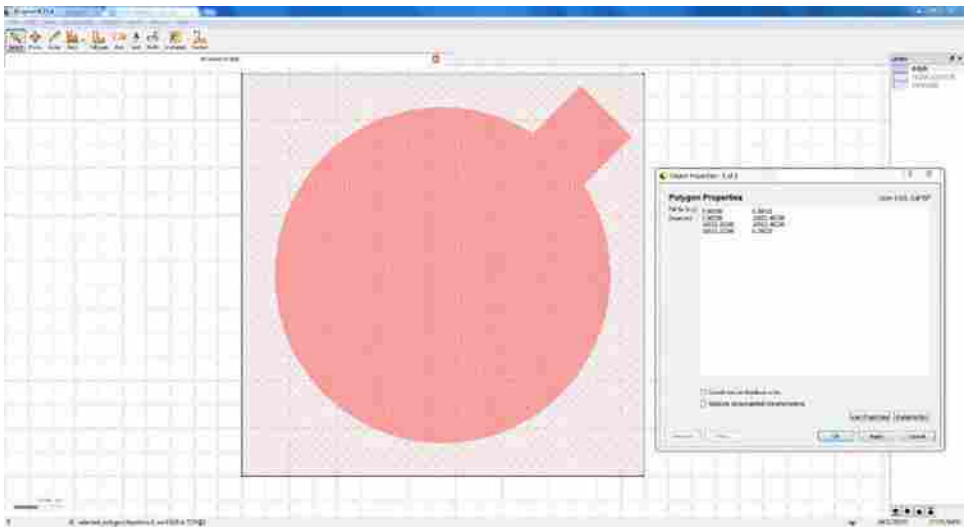

Figure A-2: Aligning cell to (0,0) location.

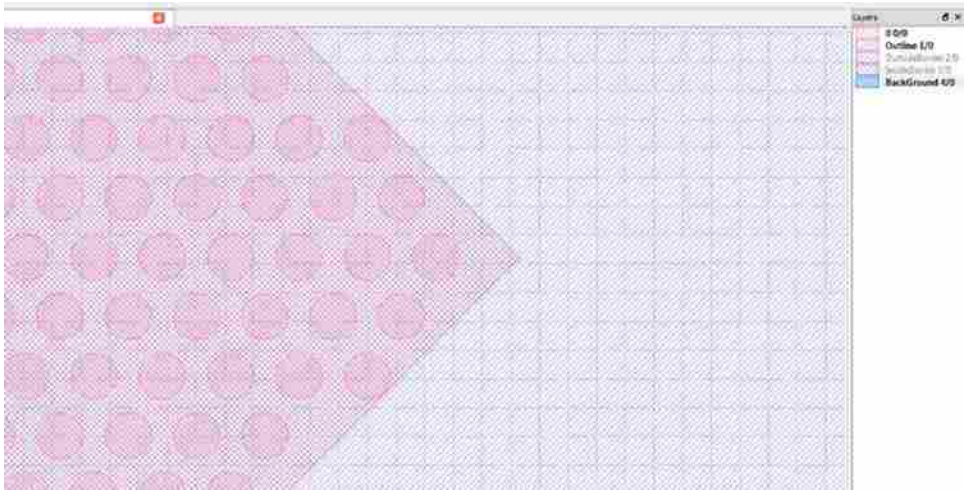

Figure A-3: Separating cell geometries onto different layers.

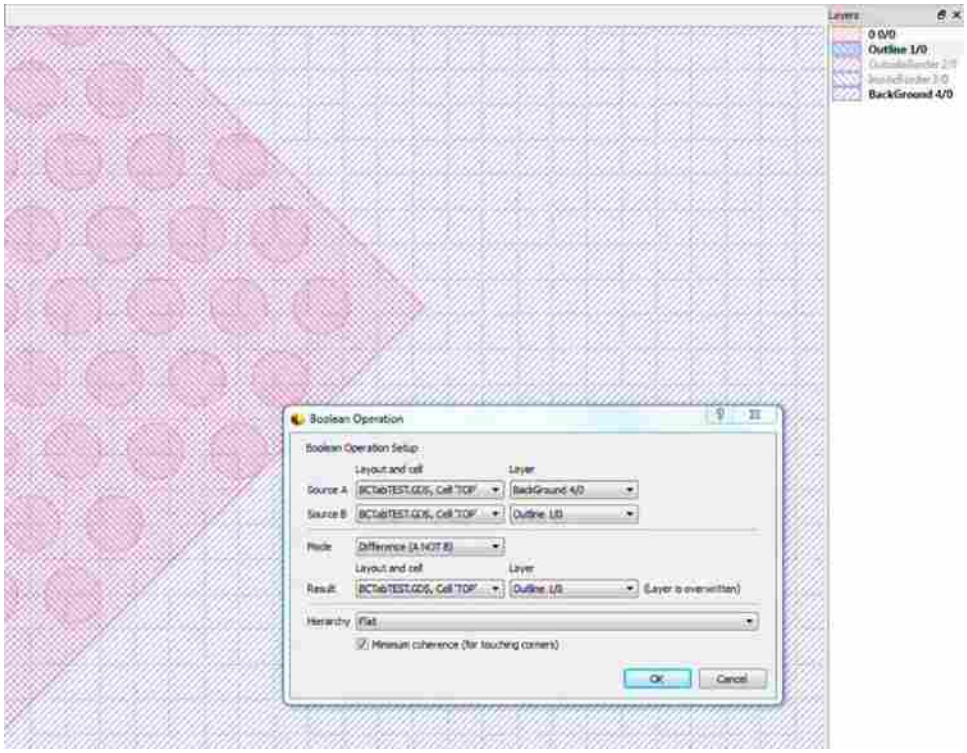

Figure A-4: Boolean subtraction to remove shaded “Outline” geometry.

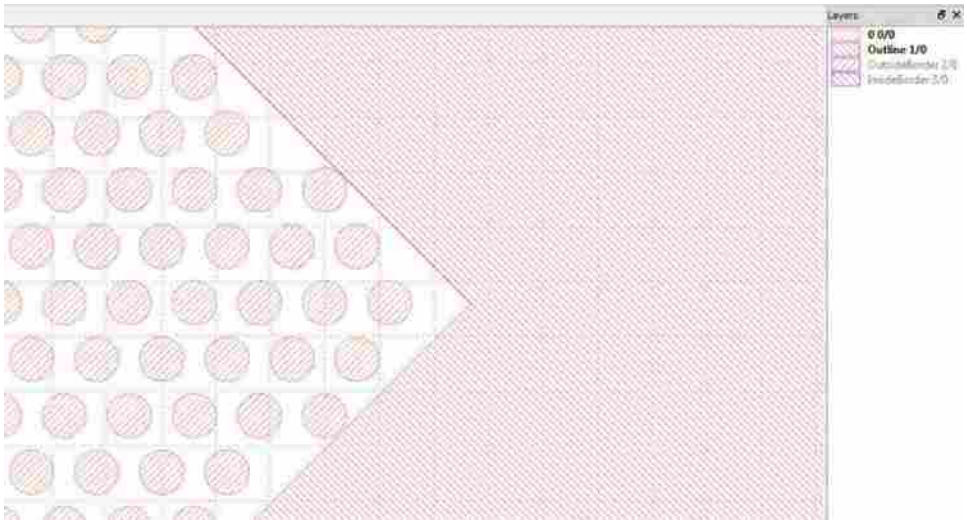

Figure A-5: Completed subtraction displays alternating shaded and blank space.

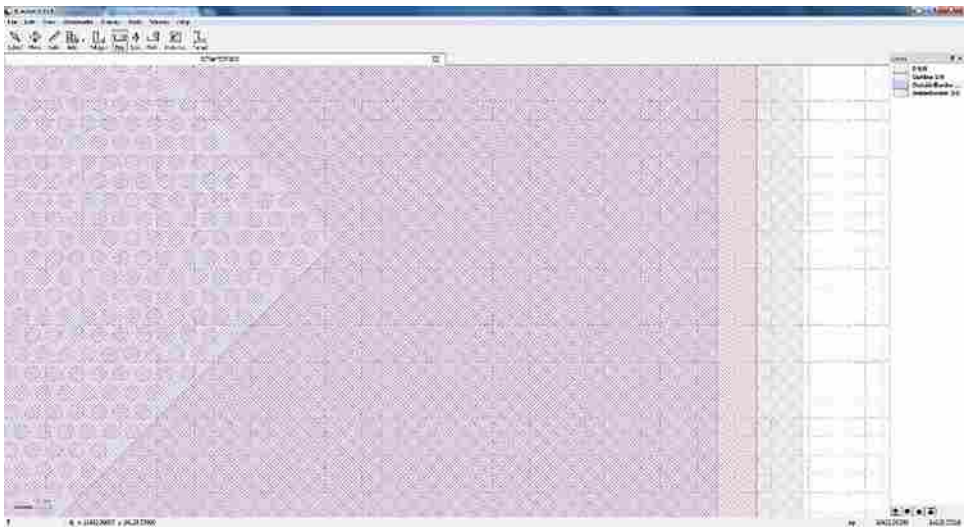

Figure A-6: Box polygon creation in preparation for cell border.

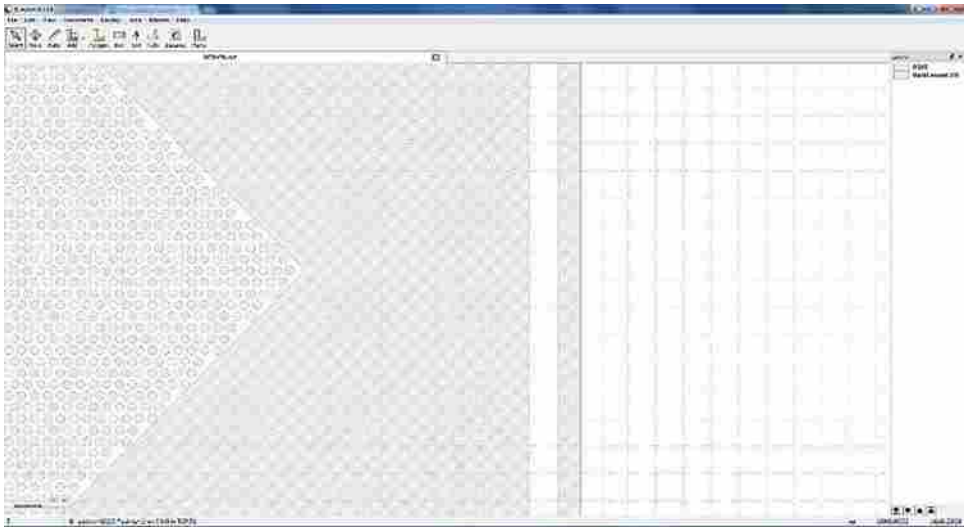

Figure A-7: Boxes have been subtracted from each other and the background.

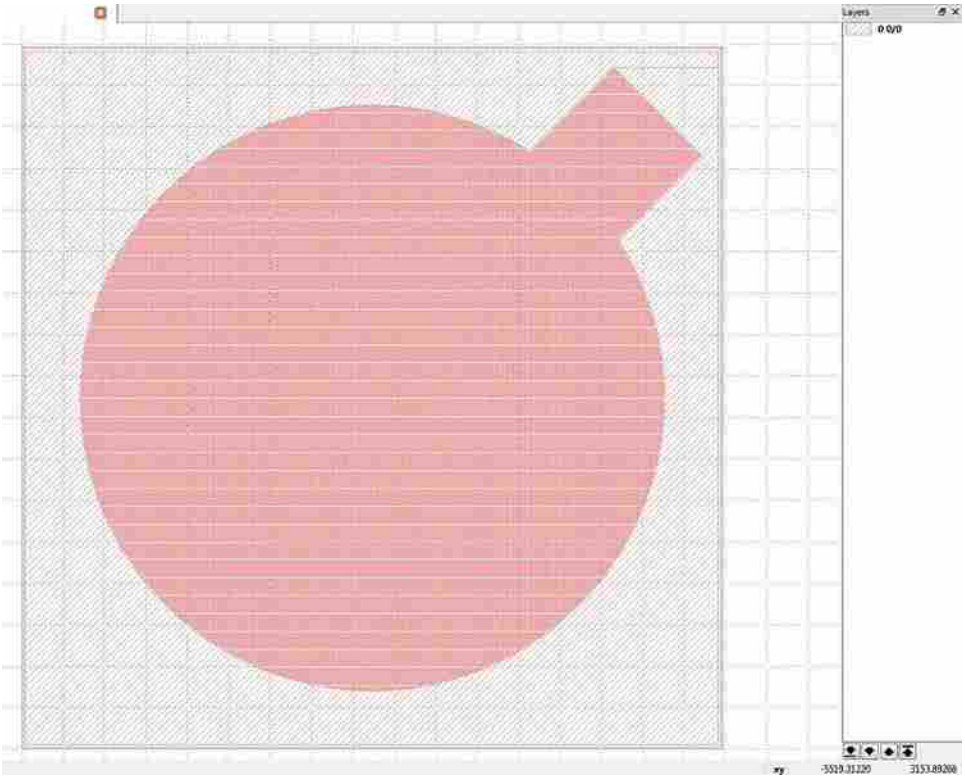

Figure A-8: Completed cell with all layers merged.

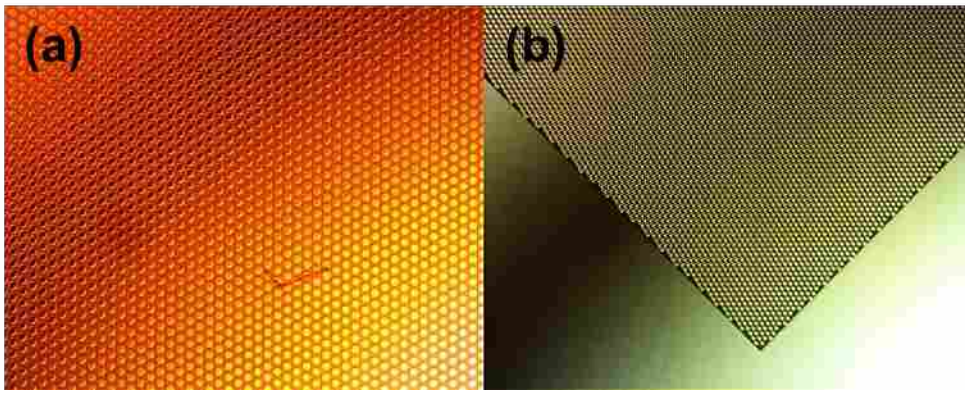

Figure A-9: Piece of photoresist on the mask (a). Cleaned mask, no photoresist visible (b).

A.2 Mask Drawings

The following is a collection of mask drawings and channel geometry.

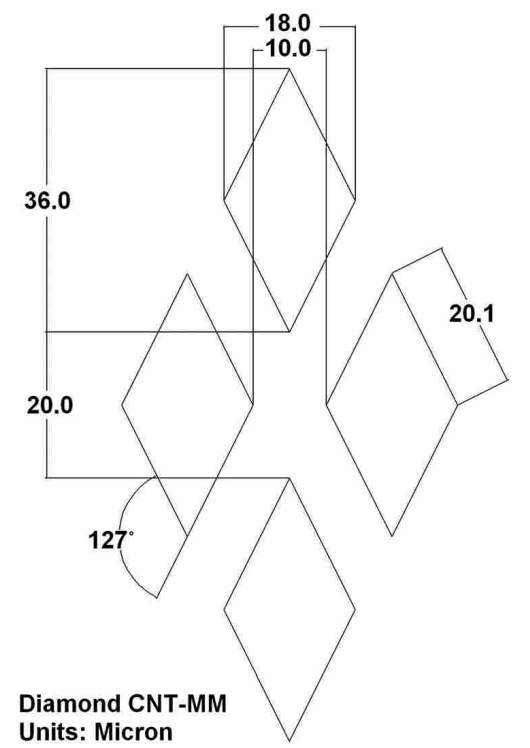

Figure A-10: Diamond pattern; Hydraulic diameter is 4.0 [μm].

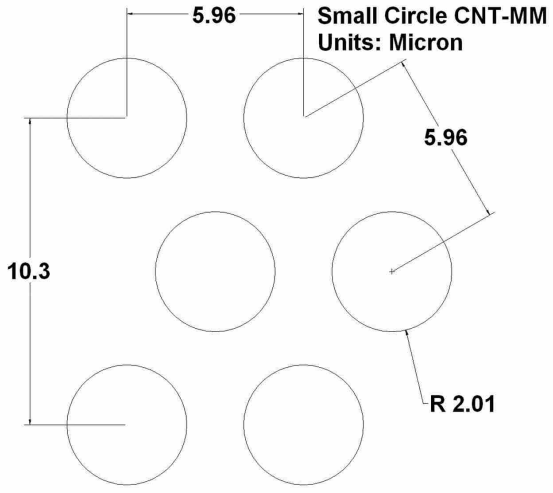

Figure A-11: Small circle pattern; Hydraulic diameter is 4.0 [μm].

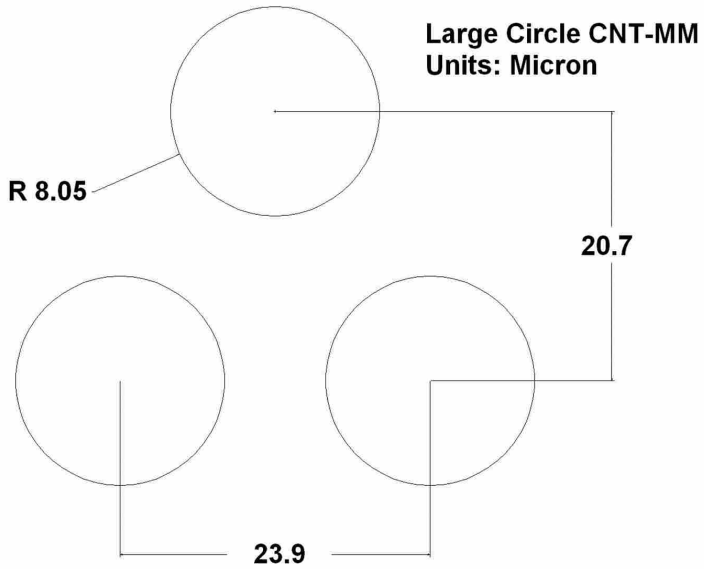

Figure A-12: Large circle pattern; Hydraulic diameter is 16.1 [μm].

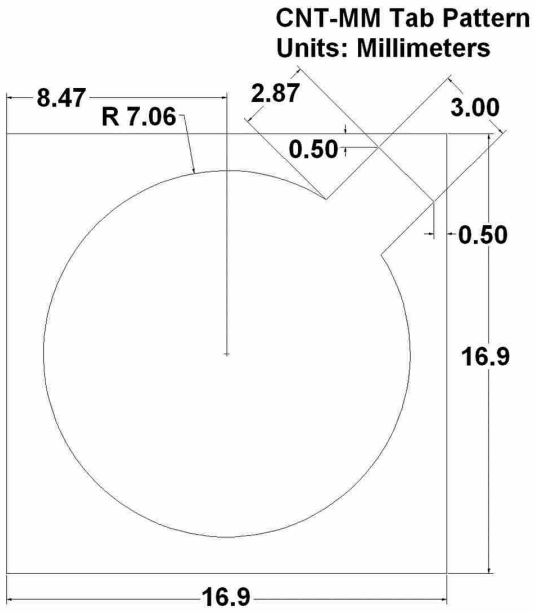

Figure A-13: CNT-MM tab pattern; CNT-MM samples of this macroscopic geometry employed the small and large circle microchannel patterns.

APPENDIX B: STANDARD PROCESSES AND EQUIPMENT PROCEDURES

B.1 Wafer Solvent Clean

1. Ensure that the motor speed on Solitec spinner is set to 0 rpm, and that the vacuum and motor switches are both turned off before beginning cleaning process
2. Turn main power for the Solitec spinner on
3. Slide wafer-positioning fixture around chuck collar
4. Place wafer onto chuck face, using fixture as alignment guide
5. While fixture (and wafer) are being pressed against bottom face of chuck collar, turn vacuum switch on
6. Lower fixture until wafer adheres to chuck face
7. Carefully slide fixture away from chuck
8. Turn motor switch on and slowly increase rotational speed to ~3,000 rpm
9. Spray continuous stream of Acetone onto center of wafer for several seconds
10. Begin to spray Isopropyl Alcohol (IPA) onto center of wafer concurrently with Acetone
11. After 1-2 seconds, discontinue Acetone stream and allow for 2-3 more seconds of IPA dispensing to continue (this ensures that no residual Acetone is left on wafer)
12. Once IPA dispensing is discontinued, allow a few seconds for the IPA to spin off of wafer (this is indicated by an outward spiral color change on wafer surface)
13. Repeat steps 9-12 three times per wafer
14. Slowly decrease spinner speed until chuck (wafer) is no longer rotating
15. Turn motor switch off
16. Turn vacuum switch off
17. Turn main power off
18. Carefully remove wafer from chuck face

B.2 Laser Cut using Epilog Legend 36EXT (120 Watt; 36” x 24”)

1. Turn on main power to Epilog laser engraver
2. Turn on power to laser engraver ventilation system
3. Open protective Plexiglas door and carefully place sample on engraving table in desired location
4. Manually focus the laser according to the sample thickness
    a. Connect manual focus gauge (V shape tool) to laser head

    b. Using the table up/down switch (found on the inner perimeter of the engraver), slowly bring the table upward until the manual focus gauge almost touches the sample
    c. Carefully remove the manual focus gauge and place back in storage
5. Using Corel Draw software on designated computer, open desired file/pattern for cutting sample
6. Ensure that all lines in file/pattern are defined as *hairline* (these will be cut as vectors) and that the pattern's page dimensions fit tight around pattern
7. Select File → Print
8. Ensure that the Epilog Engraver system is the designated printer
9. Select Properties
10. Change the workpiece dimensions to match that of the page dimensions referenced in step 6
11. Adjust vector settings (power, speed)
12. Select OK
13. Select Print
14. On Epilog Engraver control pad, ensure that desired job is in queue
15. Press Pointer key on control pad (green LED should turn on)
16. Select X/Y Off
17. Select OK
18. Adjust laser to be in desired location respective to the sample piece
19. Select Set Home
20. Close protective Plexiglas door
21. Select OK (this will begin the laser cutting process)
22. Upon completion of the cutting, open protective Plexiglas door
23. Carefully remove sample and excess material
24. Close protective Plexiglas door
25. Turn off power to Epilog laser engraver
26. Turn off power to laser engraver ventilation system
27. Close Corel Draw program on computer

B.3 Oxygen (O_2) Plasma Etch using Anelva Reactive Ion Etcher (RIE) DEM-451

1. Fill out process log sheet accompanying Anelva RIE
2. Turn on main power to Anelva
3. Ensure that Edwards 1605 Datametrics Mass Flow Controller (MFC) is on and O_2 control set to desired flowrate in Standard Cubic Centimeters per Minute (sccm)
    a. Note: Display will read 10x the actual flow rate value (i.e. 31.0 read on the display provides flow of 3.1 sccm)
4. Ensure that the Advanced Energy RFX 600 power source set at a max power of 300 Watts (W)
5. Turn chiller valve switch on
6. Ensure that oxygen tank/source is open (set to approximately 100 KPa)
7. Turn on roughing switch and blower switch simultaneously on Chiller control box
8. Ensure that mechanical Baratron Etching Gauge valve is closed (prevent damage to transducer when chamber is vented)

9. Vent Anelva etching chamber
10. Once vented, open chamber lid
11. Place samples in symmetric pattern (sides of samples should be directly adjacent to each other)
12. Use silicon holder fragments to border the outer perimeter of the samples (helping to ensure no movement of the samples during gas exchange; helping to ensure more even distribution of plasma during etch)
13. Place extra silicon holder fragments in circular pattern around samples (helping to ensure more even distribution of plasma during etch)
14. Close chamber lid slowly
15. While pressing firmly on chamber lid, slowly open etching valve
    a. Once vacuum begins to pull, let off the chamber lid and begin to slowly open etching valve further so as to increase the rate of vacuum creation within the chamber
16. Once chamber pressure (read on Roughing Gauge pressure readout) reaches 100 mTorr, open Baratron (MKS Baratron Type 127) etching gauge
17. Turn MFC oxygen (O_2) switch to Auto
18. Turn Anelva O_2 gas switch on
19. Use the Anelva etching valve to bring the pressure (indicated by the Baratron Etching Gauge display) to approximately 20 mTorr *below* target chamber pressure (pressure will rise once etching process begins)
20. Set process timer to 5 seconds beyond target process time (5 seconds allows for adjustment time for flowrate and minimizing reflected power)
21. Select Process Start on process timer
22. Once process has started, continue monitoring reflected power indicator on RFX 600 power source
    a. Adjust Impedance (coarse) and Tuning (fine) knobs as needed to minimize reflected power (target value should be 3-5 W)
23. Monitor (simultaneously with reflected power) chamber pressure (indicated by the Baratron Etching Gauge)
    a. Adjust etching valve to maintain target chamber pressure
24. Once etching process is complete, turn the Anelva O_2 gas switch off
25. Turn MFC O_2 switch to Close
26. Once the Baratron Etching Gauge display indicates that the chamber is less than 100 mTorr, close the mechanical Baratron Etching Gauge valve
27. Close etching valve
28. Vent Anelva etching chamber
29. Carefully remove samples and arrange silicon holder fragments back to storage placement
30. Repeat steps 14-16
31. Once Baratron Etching Gauge displays 100 mTorr or less, close the mechanical Baratron Etching Gauge valve
32. Close etching valve
33. Turn off roughing switch and blower switch simultaneously on Chiller control box
34. Turn Anelva Chiller switch off
35. Turn off main power to Anelva

36. Note: Chamber may be coated with molecules from previous runs (such as CF_4, or Tetrafluoromethane), making the etch not exclusive to oxygen but, rather, partially contaminated with other species (such as flourines)

B.4 Dice Samples using Disco DAD-320 Dicing Saw

1. Place wafer onto Ultron Systems, Inc. UH114 according to patterned outlined on stage
2. Place wafer ring onto stage, against alignment pegs
3. Pull adhesive sheet over wafer ring and use roller to ensure adhesion
4. Use X-Acto knife to cut adhesive sheet away from roll
5. Gently pull up on applied adhesive sheet to free ring and wafer from stand
6. Using hands, pull up on a side of the adhesive sheet, pull tightly, and re-secure on ring
    a. Repeat this step along entire perimeter of ring such that the adhesive sheet is taut
7. Use X-Acto knife to trim excess adhesive sheet along outer perimeter of ring
8. Turn on Disco DAD-320 Dicing Saw
9. Turn on dicing saw monitor
10. Ensure that water supply to dicing saw is turned on
11. Lift up on saw blade shield
12. Swing spindle armature outward
13. Use accompanying dicing saw chuck tool to loosen spindle set ring
14. Place dicing saw blade onto spindle and secure with spindle set ring using dicing saw chuck tool
15. Close saw blade shield
16. Using dicing saw control pad, select System Initialize
17. Once system initialization is complete, select Setup and confirm that the Blade Outer Diameter and Chuck Table Size are set to the correct values
18. Select Enter
    a. (Dicing saw will begin a testing procedure to validate the blade diameter value)
19. Once validation process is complete, select Spindle (this will stop spindle rotation)
20. Select Exit
21. Select F1
    a. Ensure that the Device Data Number is set to 100
    b. Ensure that the Device ID is set to Silicon
    c. Enter sample dimension (side length for square samples)
        i. Enter length (mm) in both Channel 1 (CH1) and 2 (CH2) for both Square Working Size and Y Index
    d. Ensure that Blade Height is set to correct value (dependent on blade dimensions)
22. Select Exit
23. Select F5 (for any necessary blade setting changes)
24. Select F1 and ensure that entered values were saved
25. Place wafer onto dicing saw chuck table with sheet side down and position according to pattern on chuck
26. Select Vacuum to secure wafer onto chuck
27. Select F7
28. Enter the desired number of cuts

29. Use the chuck orientation/positioning keys and optical cameras (displayed in the dicing saw monitor) to align the blade with the wafer pattern
    a. Use the Slow button to make fine adjustments
    b. Use the Index button to move cameras a preset distance (according to Index values set previously)
        i. Note: location of camera dictates cut position
30. Once aligned, and camera is located on position of desired first cut, ensure that the Slow button is activated and select U, T, /, -
    a. Note: This step is necessary because the last steps required by the dicing saw are counterclockwise and up
31. Select F5 to indicate cut direction (or other key based on dicing saw prompts)
32. Select Start/Stop to being dicing process
33. Follow additional prompts given by dicing saw as displayed on monitor
34. Once dicing process is complete, spray off wafer with accompanying air gun once cuts are complete
35. Select Spindle to stop spindle rotation
36. Select Vacuum
37. Remove wafer
38. Using X-Acto knife, trim adhesive tape around outer perimeter of wafer
39. Carefully fracture wafer along cut lines
40. Place wafer in clean wafer carrying case
41. Dispose adhesive tape on wafer ring
42. Reverse procedure outlined in steps 11-15 to remove dicing saw blade
43. Turn water supply off
44. Turn off dicing saw monitor
45. Turn off Disco DAD-320 Dicing Saw

B.5 Film Deposition using Denton Vacuum Integrity 20 E-Beam Evaporator

1. Fill out E-Beam Evaporator logbook
2. If chamber is initially under vacuum, ensure that all functions/valves are off and select Vent button
3. Once chamber is vented, the chamber door should open easily allowing for placement of wafers
4. Turn Vent button off
5. Inspect wafer planetary system and ensure that motor fixtures are installed
6. Secure wafers to wafer plates by gently tightening set screws around perimeter of wafer
7. Use thumbs to ensure that wafer is securely fasted to wafer plate
8. Use clean air or nitrogen gun to gently blow off each wafer assembly before installation onto planetary system in E-Beam Evaporator chamber
9. Use set screw on backside of wafer plate to mount securely to motor fixtures
10. Gently pull on each wafer plate after installation to ensure that plates are securely fastened
11. Secure wires from each battery on motor fixtures to accompanying electric motor to begin rotation of wafer plates
12. On E-Beam Evaporator display, select Rotation to begin rotation of planetary system

a. Note: Speed button can also be used to adjust rotational speed of planetary system
13. Ensure E-Gun Shutter is open (green) so as to allow access to the crucible receiver
14. Acquire crucible of desired material
15. Using large tweezers, place crucible into receiver of E-Beam Evaporator
16. Use a flashlight to illuminate crucible within chamber
    a. Flashlight should be placed such that it does not need to be held in place
17. Align E-Beam Evaporator mirrors such that the crucible can only be seen through the sightglass by reflection off mirrors, and not by direct line of sight
    a. Note: If crucible can be seen by direct line of sight, deposition will occur on sightglass
18. Turn off, and remove, flashlight from E-Beam Evaporator chamber
19. Shut chamber door and press firmly on door until vacuum is pulled in chamber during following steps
20. Select Mech Pump button (turn on; green)
21. Select Roughing Valve button (turn on; green)
22. Wait till Chamber TC display indicates a chamber pressure of 1.0E-1 Torr or lower
23. Select Roughing Valve button (turn off; red)
24. Select High Vac Valve button (turn on; green)
25. Wait till Chamber TC display reads 'High Vac'
26. Select Ion Gauge Emission (turbo pump) button (turn on; green)
27. Wait till Chamber IG display indicates a chamber pressure of 5.5E-5 Torr or lower
    a. Note: Proceed to steps 28.a.-28.g. While waiting for chamber pump down
28. Record respective pump down times in E-Beam Evaporator logbook
29. Perform deposition
    a. Turn on main power to Telemark TT-3 Power Supply
    b. Ensure that Voltage/Emission button is off
    c. Turn on main power to Inficon XTC/2 deposition controller box
    d. Set parameters on deposition controller box according to material
        i. Select Reset
        ii. Select Stop
        iii. Change parameters by selecting Program (navigate using arrow keys; be sure to select either the up or down arrows after a value is entered in order to store the value)
            1. Tooling factor
            2. Density
            3. Z-Ratio
        iv. Select Program to return to main screen
    e. Allow at least 2 min for power supply and deposition controller box to warm up
    f. Select Life to display crystal life (XTAL%)
    g. Record crystal life in logbook
    h. Turn Voltage/Emission button on
    i. Slowly ramp up Emission Current Adjustment knob, allowing for about 5 seconds between each value of 10 on dial
    j. Once a visual of the crucible can be seen through sightglass, adjust current pattern as desired
        i. Change current pattern type by using Spiral/Triangle/Manual

ii. Adjust pattern spread using Lateral Frequency, Longitudinal/Modular Frequency, Lateral Amplitude, and Longitudinal/Modular Amplitude knobs
iii. Adjust pattern location using Sweep joystick, ensuring that current pattern is located exclusively within the material to be deposited

k. Select E-Gun Shutter button (turn off; red) to ensure that deposition will not begin prematurely during ramp up
l. Once shutter is closed, continue slowly ramping up Emission Current Adjustment knob until desired current is achieved
m. Select E-Gun Shutter button (turn on; green) to open shutter
n. Select Start button on deposition controller box to begin deposition measurements
o. Continue deposition until desired thickness is met (read in KA)
p. Select E-Gun Shutter button (turn off; red)
q. Begin slowly ramping down current using Emission Current Adjustment knob
r. Record deposition thickness on E-Beam Evaporator logbook along with operating pressure, *etc*.
s. Once current reads 0.0 mA (off), turn Voltage/Emission button off
t. Allow power supply and deposition controller box at least 2 minutes to cool down
u. Turn power supply and deposition controller box off

30. Select Ion Gauge Emission button (turn off; red)
31. Select High Vac Valve button (turn off; red)
32. Select Mech Pump button (turn off; red)
33. Select Vent to vent chamber
34. Select E-Gun Shutter button (turn on; green)
35. Once chamber is vented, reverse procedure outlined in steps 6-12 to remove wafers from planetary system and disconnect wafers from plates
36. Once wafers are removed, shut chamber door and press firmly on door until vacuum is pulled in chamber during following steps
37. Put E-Beam Evaporator in standby mode
    a. Select Mech Pump button (turn on; green)
    b. Select Roughing Valve button (turn on; green)
    c. Wait till Chamber TC display indicates a chamber pressure of 100 Torr or lower
    d. Select Roughing Valve button (turn off; red)
    e. Select Mech Pump button (turn off; red)

B.6 Hexamethyldisilazane (HMDS) Spin Coating

1. Place and center wafer on Laurell WS-400-6NPP Spin Coater chuck
2. Select Vacuum button to turn on vacuum
3. Select Program button to cycle through preset spin settings (adjust as needed)
    a. Program D
        i. Speed: 3000 rpm
        ii. Acceleration: 550 rad/s^2
        iii. Time: 10 sec
4. Spray surface clean with clean air or nitrogen gun
5. Dispense about 3-4 drops of HMDS onto center of wafer surface

6. Immediately close spin coater lid and select Run/Stop button
7. Close HMDS bottle
8. Open spin coater lid and inspect wafer once spin coating is complete
    a. If coating is not satisfactory, solvent clean wafer and bake in oven at 150 °C for 8-10 min
    b. Repeat HMDS spin coating process
9. Select Vacuum button to release wafer
10. Remove wafer and place in storage case
11. Use Acetone to remove excess photoresist from inside of spin coater

B.7 AZ 2020 (or AZ 3330) Spin Coating

1. Place and center wafer on Laurell WS-400-6NPP Spin Coater chuck
2. Select Vacuum button to turn on vacuum
3. Select Program button to cycle through preset spin settings (adjust as needed)
    a. Program T
        i. Speed: 2750 rpm
        ii. Acceleration: 2750 rad/s^2
        iii. Time: 60 sec
4. Spray surface clean with clean air or nitrogen gun
5. Dispense about ~40 drops of AZ 2020 onto center of wafer surface
6. Immediately close spin coater lid and select Run/Stop button
7. Close AZ 2020 bottle
8. Open spin coater lid and inspect wafer once spin coating is complete
    a. If coating is not satisfactory, solvent clean wafer and bake in oven at 150 °C for 8-10 min
    b. Repeat AZ 2020 spin coating process
9. Select Vacuum button to release wafer
10. Remove wafer and place in storage case
11. Use Acetone to remove excess photoresist from inside of spin coater

B.8 AZ 2020 Development

1. Rinse and dry crystallizing dish
2. Pour AZ developer (300 MIF) into crystallizing dish
3. Place wafer in the beaker
4. Agitate developer gently for 30 s -1 min
5. Monitor the progress of the development
6. Using wafer tweezers, remove wafer and hold under a gentle stream of deionized (DI) water in sink for 30 s -1min
7. Place wafer onto cleanroom paper towel
8. Gently blow off water, beginning at center of wafer and moving radially outward, using clean air or nitrogen gun
9. Inspect wafer under optical microscope to ensure development completion
10. Repeat steps 3-9 with short development times until the development is complete

    a. Note: If development becomes ruined, use aluminum wet etch as prescribed on cleanroom website (http://www.cleanroom.byu.edu/wet_etch.phtml)
11. Place wafer in storage container
12. Dispose of 300 MIF
13. Rinse and dry crystallizing dish

B.9 Photoresist Exposure with 4" MA 150 CC Karl Suss Mask Aligner/Bonder

1. Ensure that aligner is powered on, gas valves are open, and desired channel wavelengths are available
    a. Channel 1: 365 nm
    b. Channel 2: 405 nm
    c. Note: If aligner is not powered on, follow Operating Instructions given on the cleanroom website (http://www.cleanroom.byu.edu/ma150.phtml)
2. Set exposure parameters on aligner
    a. Select Change Program button
    b. Select Edit button
    c. Select Page 1 button
        i. Set Max Exposures
        ii. Set Exposure Time
        iii. Set Alignment Gap (0 μm)
        iv. Set Hard Contact Time (10 sec)
    d. Select Return button
    e. Select Page 2 button
        i. Set Resist (Negative)
        ii. Set Mode (First Mask)
        iii. Set WEC (Contact)
        iv. Set Alignment Check (Off)
        v. Set Prealigner Type (0)
    f. Select Return button
    g. Select Continue button
    h. Select Change Type
    i. Select Hard Contact
    j. Select Return button
    k. Select Return button
3. Select Start button
4. Vacuum will release on mask panel, allowing for removal of mask if one is present
5. Select Continue button
    a. Wafer chuck will rise
6. Place wafer onto chuck, ensuring that the flattened edge of the wafer is aligned with patterned edge on chuck
7. Use fingers around outer perimeter of chuck to center wafer
8. Select Vacuum: Off button (should now read Vacuum: On)
9. Select Continue button
10. Chuck will lower and panel will unclamp

11. Gently slide panel away from aligner about halfway along track (a 'click' should be heard, indicating the max recommended draw for the panel)
    a. Warning: Pulling panel any farther will cause panel to fall off of track
12. Gently place mask, chrome side down, onto panel using alignment pins for centering
    a. Note: a light solvent clean is recommended for mask prior to exposures
        i. Lightly rinse both sides of mask with Acetone, followed by IPA, and dry with clean air or nitrogen gun
13. Select Vacuum: Off button (should now read Vacuum: On)
14. Once vacuum is pulled on mask, gently apply pressure to mask with fingers to ensure that mask is securely held to panel
15. Firmly slide panel back into aligner until seated
16. Select Clamping: Off button (should now read Clamping: On)
17. Select Continue button
18. Chuck will rise and press wafer against mask; exposure process will begin
19. After exposure, chuck will lower and clamping will turn off
20. Gently slide panel away from aligner about halfway along track
21. Select Vacuum: On button (should now read Vacuum: Off) and remove mask
22. Gently place mask back in storage container
23. Firmly slide panel back into aligner until seated
24. Select Clamping: Off button (should now read Clamping: On)
25. Select Continue button
26. Chuck will rise and vacuum will turn off
27. Gently remove wafer and place in storage container, ensuring that wafer is not exposed to ultraviolet (UV) light until after subsequent bake and development processes
28. Repeat steps 5-26 for additional wafers
29. Once wafer is removed, select Cancel
30. Chuck will lower (aligner display will return to main screen)

B.10 CNT Growth using Lindberg/Blue M Tube Furnace

1. Pour acetone in crystallizing dish, or solvent-resistant container
2. Carefully place diced samples into container (with photoresist coating side up)
3. Sonicate for at least 15 min
4. After sonication, carefully remove sample with tweezers while maintaining a thin Acetone film so as to ensure that Acetone does not evaporate (leaving residue) during transport of sample
    a. Now that the sample has no protective coating use extra caution when transporting samples so as to not scratch iron (Fe) layer
5. Rinse Acetone film off using IPA
6. Gently blow off IPA (before evaporation begins as with Acetone) using clean air or nitrogen gun
7. Inspect pattern under optical microscope
8. Repeat steps 4-7 for each sonicated sample
9. Dispose of Acetone
10. Rinse crystallizing dish and dry
11. Ensure regulators on gas tanks (Hydrogen, Ethylene, Argon) are closed

12. Open main valve on each tank
13. Slowly adjust regulator to bring outflow pressure on each tank to 20 psi
14. Using Mass Flow Controller (MFC), set desired flow parameters
    a. Ensure left switch for each gas is set to Off
    b. Using right switch for each gas, select Set
    c. Dial in desired Setpoint (%); see calibration sheet for conversion from sccm
    d. Return right switch for each gas to Flow position
    e. Repeat steps 14.a-14.d for each gas
15. Unlatch and open furnace lid so as to deactivate the heating element
16. Ensure that furnace has cooled sufficiently since last growth
17. Loosen and remove metal inflow cap from glass tube
18. Use retrieval tool to slide quartz boat out of tube
    a. Note: Latex or Nitrile gloves should be worn to avoid contamination of quartz boat by skin oils/greases
19. Gently blow off particulate matter from samples using clean air or nitrogen gun
20. Place samples on quartz boat
21. Place quartz boat back into glass tube and position near center of tube
    a. Note: boat should be centered about furnace thermocouple
22. Replace and tighten metal inflow cap on glass tube
23. Enter first setpoint temperature using digital gauge on front of furnace
24. Rotate mechanical valve to H_2 position (this allows flow of hydrogen and ethylene gases, while preventing flow of oxygen)
25. Using left switch for hydrogen gas on MFC, select Manual (this will begin flow of hydrogen gas)
26. Ensure that bubbles begin to form in outflow beaker
    a. Note: If no bubbles are present, return MFC switches to Off position and inspect setup; seek consultation before proceeding
27. Close, and latch, furnace lid (heating element will be activated)
28. Once first setpoint temperature is reached, select Manual on left switch for ethylene gas on MFC
29. Start timer for growth
30. Once prescribed growth time is reached, select Off for ethylene gas on MFC
31. Enter second setpoint temperature using digital gauge on front of furnace
32. Once second setpoint temperature is reached, select Manual for ethylene gas on MFC
33. Start timer for infiltration
34. Once prescribed infiltration time is reached, select Off for ethylene gas on MFC
35. Enter 20 °C using digital gauge on front of furnace and allow furnace to begin cooling
36. Once furnace reaches ~600 °C, unlatch and open furnace lid
37. Cool furnace with fan
38. Allow furnace to cool sufficiently before handling glass tube and components
    a. Note: Temperature of quartz boat is higher than that measured by thermocouple; consider using tweezers during transport of boat
39. Once furnace has cooled, select Off for hydrogen gas on MFC
40. Select Manual for argon gas on MFC
41. Allow several seconds for evacuation of hydrogen gas
42. Select Off for argon on MFC

43. Loosen and remove metal inflow cap from glass tube
44. Use retrieval tool to slide quartz boat out of tube
45. Remove samples from quartz boat and place in storage container
    a. Note: Depending on growth conditions, samples may have self-released from silicon substrate; extra care should be taken to ensure that samples do not fall from substrate during transport
46. Place quartz boat back into glass tube and position near center of tube
47. Replace and tighten metal inflow cap on glass tube
48. Perform burn-out process
    a. Enter 950 °C as furnace setpoint temperature
    b. Close, and latch, furnace lid
    c. Rotate mechanical valve to Air position
    d. Ensure that no gases are flowing through tube by inspection of MFC and outflow beaker
    e. Select On for Air on MFC
    f. Once furnace temperature has reached 950 °C, allow ~2-3 min for burn-out
    g. Select Off for Air on MFC
    h. Unlatch and open furnace lid
        i. Note: If glass is not cleaned, continue burn-out process
    i. Allow furnace to cool by natural convection
49. Note: If samples did not self-release, place in potassium hydroxide (KOH) solution and let stand at ~60 °C until samples separate from substrate

B.11 Iron Deposition using Thermal Evaporator

1. Vent the chamber and raise the bell jar.
    a. The system should be in standby. Ensure the ion gauge is off and both the gate valve and roughing valve are closed.
    b. Open nitrogen tank with the regulator set to 10 psi.
    c. Open the vent valve to pressurize the chamber to 760 Torr. When the chamber is pressurized, the rubber seal should break. Close the vent valve and nitrogen tank.
    d. Raise the bell jar by pressing the raise button.
2. Prepare sample and source material.
    a. Use Kapton tape to place the sample on the target plate above the closed shutter.
    b. Secure iron evaporator boat between electrodes. Ensure boat contains sufficient iron material.
    c. Clean or replace glass slide window as needed.
3. Check the crystal monitor and set material properties on the INFICON deposition monitor.
    a. Turn on the monitor and press the “XTAL” button. If XTAL reading is 100%, replace the crystal.
    b. Set the density, z-ratio, and tooling factor. This can be done while the chamber is pumping down. Press the PROG button to change properties. For iron, the settings are

i. Density = 7.86
ii. Z-Ratio = .349
iii. Tooling factor = 109.5%

c. Press PROG to save changes.

4. Pump down the chamber.
    a. Lower the bell jar with the sealing surface centered.
    b. Make sure the vent valve is closed. Slowly open the roughing valve, keeping the foreline pressure (TC2) below 3 x 10^2 Torr.
    c. When the chamber pressure (TC1) reads 1.5 x 10^0 Torr, close the roughing pump valve. This should take around 3 minutes.
    d. Open the gate valve.
    e. Turn on the ion gauge by pressing the "EMIS" button on the VARIAN SenTorr.
        i. The filament should light up, and a pressure reading will be given on the SenTorr next to the IG label.
    f. Let the cryo pump reduce pressure to 1 x 10^{-5} Torr or less.
5. Deposition.
    a. Toggle the "FILAMENT" switch on the control panel to turn on the current supply.
    b. Slowly ramp up the current supply with the VARIAC knob.
        i. To prevent thermal hardening of the boat, do not exceed a ramp speed of 20 V/min.
        ii. The current supply should never exceed 10 amps.
    c. Increase the current until the deposition rate on the monitor reads.5 angstroms/s (usually about 150 V or more).
    d. Simultaneously open the shutter and press ZERO on the deposition monitor to reset and record sample thickness.
    e. Close the shutter when the monitor reaches the desired thickness (about 7 nm, or 70 angstroms).
    f. Ramp down the current no faster than 30 V/min.
    g. Wait at least 10 minutes for the system to cool before venting the chamber.
6. Vent chamber and remove samples.
    a. Turn off ion gauge and toggle the gate valve switch to "closed".
    b. Open nitrogen tank and vent valve, as before.
    c. When the rubber seal breaks at 760 Torr, close vent valve and nitrogen tank.
    d. Raise the bell jar and remove your samples.
7. System standby.
    a. Lower the bell jar with the seal centered.
    b. Slowly open the roughing valve, being sure not to exceed 3 x 10^2 Torr for the foreline pressure.
    c. Allow the pressure to reach 5 x 10^{-1} Torr. Close the roughing valve.

B.12 Fabrication of CNT-MM

1. Start with 4" SiO_2 wafer
2. Spin solvent clean
3. Dehydrate bake wafer at 150 °C for 10 min
4. Deposit Al_2O_3 ~30 nm thick
    a. Note: If wafer was coated with Al_2O_3 previously, perform steps 2-3 to remove accumulated particulate matter/residues
5. Spin coat with HMDS
6. Spin coat with AZ 2020
7. Soft bake wafer on hot plate for 60 sec at 110 °C
8. Allow 1 min for wafer to cool
9. Expose photoresist with mask
10. Hard bake wafer on hot plate for 60 sec at 110 °C
11. Allow 1 min for wafer to cool
12. Develop AZ 2020 photoresist
13. Evaporate Fe ~7 nm thick
14. Sonicate wafer for at least 15 min in Acetone, or N-Methyl-2-pyrrolidone (NMP), and rinse with IPA
15. Dry with clean air or nitrogen gun
16. Spin coat with AZ 3030
17. Soft bake wafer on hot plate for 60 sec at 110 °C
18. Dice samples
19. Grow samples
20. O_2 etch samples
21. Perform chemical deposition (A.13)
22. Soak in DI water for 5 min (leaving samples on Teflon stands in order to expose both sides of samples and avoid crash-out of Pt)
23. Dehydrate bake samples (samples should still be on Teflon stands) at 150 °C for 10 min
24. Carefully remove samples from Teflon stands and place in storage container

B.13 Static Pt Deposition onto CNT-MM

1. Note: Latex, or Nitrile gloves, should be worn for all following steps
2. Calculate required mass of Chloroplatinic Acid Hexahydrate ($H_2PtCl_6*(H_2O)_6$) to achieve desired solution molarity
3. Place chemical weighing boat on Mettler AE 240 Balance and tare
4. Ensure weighing boat mass is properly accounted for by removing and replacing boat and checking that scale returns to ~0.0000 grams (g)
    a. Calibrate balance and tare weighing boat as needed
5. Weigh each carbon (C) sample three times and record average mass
    a. Note: Remove weighing boat (containing sample) from balance and replace between each measurement
    b. Note: Weigh empty weighing boat between each run (three measurements) to ensure that balance still reads ~0.0000 g; tare as needed

    c. Note: combined mass of carbon samples in deposition will dictate Pt-C weight percent (% [w/w] Pt-C); adjust, as desired, by removing or adding carbon samples from proposed deposition
6. Carefully secure CNT-MM to Teflon stand and place in beaker
7. Use balance to achieve required amount of chloroplatinic acid
    a. Note: Use clean Teflon-coated spatula (or other chemically inert tool) to transport chloroplatinic acid
8. Suction required volume of water into syringe
9. Use impinging jet from syringe to rinse chloroplatinic acid from weighing boat into beaker containing carbon sample
10. Suction required volume of formic acid (HCOOH) into syringe
11. Dispense formic acid into beaker
12. Use calibrated pH meter to measure pH of solution while gently agitating solution to ensure mixing
    a. Note: Calibrate meter as needed prior to measurement
    b. Note: Sodium Hydroxide additives can be used to increase pH for variation in deposition time and resultant Pt morphology
13. Close beaker using Parafilm sheet
14. Allow time for deposition to occur
    a. Note: Deposition process is finished once amber-like colored solution becomes clear
15. After deposition, carefully remove CNT-MM (still attached to Teflon stand) from deposition solution and submerge in clean water for ~ 5 min.
16. Remove CNT-MM (still attached to Teflon stand) from water and place in dehydration bake oven for at least 8 min.
17. Remove CNT-MM from oven and from Teflon stand

APPENDIX C: SUPPLEMENTARY CHARACTERIZATION MATERIAL

C.1 Nitrogen Gas Adsorption Testing

Nitrogen adsorption analysis was performed on a Micromeritics ASAP 2010 system at 77 [K] (Micromeritics Instrument Corporation, Norcross, GA). Samples were degassed at 100 [°C] prior to analysis. Surface area was calculated by the Brunauer-Emmett-Telller (BET) method, pore size was measured by the Barrett-Joyner-Halenda (BJH) method using the adsorption branch of the isotherm, and total pore volume was determined by the single point method at relative pressure (P/P0) 0.97.

Figure C-1 shows the N2 adsorption isotherms for both (O2 etched) CNT-MM and Pt-CNT-MM samples. The CNT-incorporated membranes each exhibited a type II nitrogen adsorption-desorption isotherm indicative of a macroporous material. The calculated BET surface area and pore volume for the CNT-MM sample was 61 [m^2 g^{-1}] and 0.118 [cm^3 g^{-1}], respectively. BET surface area and pore volume for the Pt-CNT-MM sample was 14 [m^2 g^{-1}] and 0.118 [cm^3 g^{-1}], respectively. Pore size distributions for both samples were wide and showed no distinct peaks.

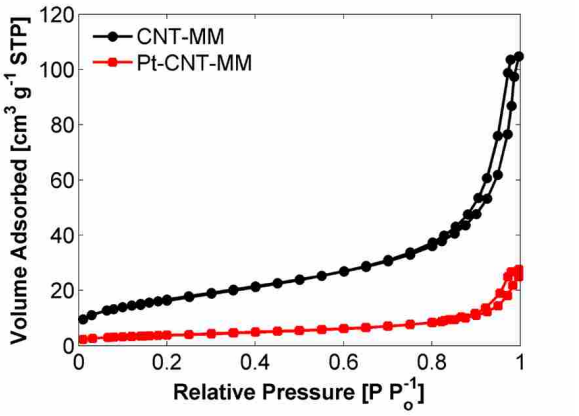

Figure C-1: N2 adsorption isotherms used for Braunauer-Emmett-Teller (BET) surface area analysis of CNT-MM and Pt-CNT-MM samples.

APPENDIX D: SUPPLEMENTARY INFORMATION (PROPULSION)

D.1 Activation Energy Testing

Activation energy tests, by H_2O_2 decomposition, was determined using three Pt-CNT-MM samples fabricated following the procedure described previously. Each sample was tested three times, after which the pressure data was averaged per sample. The test apparatus consisted of two, 125 [mL], round-bottom flasks. One flask was used for the Pt-CNT-MM test environment and the other as a reference environment (Figure 7). Magnetic stir bars were placed inside each flask to increase the amount of H_2O_2 contacting the catalytic Pt-CNT-MM samples. To ensure the flasks were airtight, rubber septums with a rim seal were positioned on each flask. The flasks were placed inside ice or water baths on top of a hot plate stirrer to maintain isothermal conditions during each of the three runs per sample (0 [°C], 17.5 [°C] and 35 [°C]). To ensure that no steam was produced during testing, such that all generated pressure was due to the release of O_2, a low concentration H_2O_2 solution (1% [w/w] H_2O_2, diluted from 30% [w/w] H_2O_2; Fisher Scientific BP2633-500) was used for all tests. The H_2O_2 solution stock was placed within a 50 [mL] container and immersed in the respective ice/water baths in order to achieve thermal equilibrium prior to testing. After achieving thermal equilibration, each flask was vented by temporary insertion of an unattached needle and allowed to equilibrate with atmospheric pressure. The amount of O_2 generated during each test was measured as a pressure differential between the testing and reference environments. To measure the pressure differential, an Extech HD750 Differential Pressure Manometer

(measuring up to ± 5 [psi] / 34.5 [kPa]) is connected to each flask *via* two high strength silicone tubes (diameter 0.375 [in]/9.525 [mm]). The tubing was connected to the manometer and syringe needles using barbed fittings. The two syringe needles connected to the pressure manometer were inserted into the test and control flasks, respectively, by piercing through the diaphragm of each septa. The differential pressure between the test and control flasks was zeroed before recording data and then measured as a function of time with a laptop computer *via* a USB connection. Finally, 10 [mL] of the H_2O_2 solution was simultaneously injected into each flask while the magnetic stir bars stirred the solution at 200 [rpm]. Resultant differential pressure *vs.* time data was then used to determine catalyst performance and activation energy with the Arrhenius Equation.

Figure D-1: Experimental apparatus used to monitor the increase in pressure due to O_2 generation during H_2O_2 decomposition. Water maintained at a constant temperature holds test and control flasks on a hotplate while a differential pressure monitor measures transient pressure data.

D.2 MUV Fabrication and Testing

The MUV test submersible was designed with computer aided design software (SolidWorks®) and printed with an Objet500 Connex 3D printer with a PMMA like resin. The test submersible was then fitted to a 30.5 [in.] (0.77 [m]) rigid arm through screw thread fastening

and submerged into a water tank (350 [gal]). The opposite end of the arm was secured to a torque transducer (Interface model 5350-50: 50 [oz-in] sensor) mounted above the water tank. The transducer reported torque measurements with 0.001 [N-m] precision along the parallel axis of the test submersible *via* a CPU connection. Force (thrust) measurements were calculated *via* software on the CPU. H_2O_2 was pumped into the reaction chamber *via* a 50 [mL] syringe connected to the test submersible's reaction chamber *via* high strength silicone tube (dia.: 0.375 [in.] / 9.525 [mm]) that fits over a plastic barbed fitting.

APPENDIX E: SUPPLEMENTARY INFORMATION (SENSING)

E.1 Cyclic Voltammetry

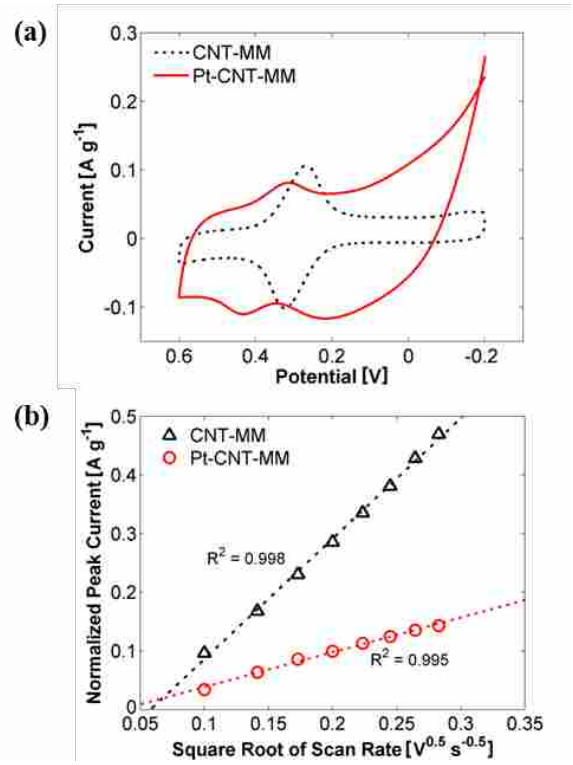

Figure E-1: CV characterization of CNT-MM and Pt-CNT-MM samples within ferricyanide mediator solution (4 [mM] $Fe(CN)_6^{3-}$ and 1 [M] KNO_3). **(a)** Comparative cyclic voltammogram (current normalized by sample mass) for CNT-MM and Pt-CNT-MM samples. CNT-MM samples were shown to have an average ESSA of 293.1 ± 27.8 [$cm^2\ g^{-1}$] whereas Pt-CNT-MM samples were shown to have an average ESSA of 53.3 ± 6.3 [$cm^2\ g^{-1}$], with respect to the ferricyanide mediator solution. **(b)** Plot of the magnitude of the normalized anodic peak current versus the square root of the scan rate for both a CNT-MM substrate and Pt-CNT-MM sample, indicating that the transport of ferricyanide to the catalytic surface is a diffusion-controlled process.

E.2 Amperometric Measurement of H_2O_2 Samples

Note: Prescribed volumes should be adjusted according to electrochemical cell size, *etc*. The procedure outlined below is for use of Dr. Richard Watt's electrochemical setup.

E.2.1 Prepare the Buffer Solution

1. Locate a clean 15 mL or 50 mL plastic tube container in a drawer opposite to the potentiostat
2. Fill the container to the desired volume with de-ionized water or miliQ water
    a. De-ionized water comes from the left faucet at any of the sinks
3. Locate Tris Base powder (in a blue container, usually above the potentiostat)
4. Zero the scale opposite the potentiostat with a plastic saucer on it
5. Weigh out the required amount of Tris Base to achieve a 25 mM solution
    a. For example, a 12 mL solution would require 36.3 mg of Tris Base

$$(121.14\ [g\ mol^{-1}])(25e^{-3}\ [M])(\#\ [L]) = (\#\ [g])$$

6. Pour some of the water from the container into the saucer containing the Tris Base
7. Pour mixture into tube container and repeat if necessary
8. Locate Sodium Chloride (NaCl) (in a small white container in the cabinet above the scale) with 25 mM Tris base and 0.5 M Sodium Chloride (NaCl)

$$(58.44\ [g\ mol^{-1}])(0.5\ [M])(\#\ [L]) = (\#\ [g])$$

9. Repeat steps 4-7 adding 0.5 M Sodium Chloride to solution
    a. Again if making 12 mL of buffer, add 350.6 mg NaCl

E.2.2 Prepare the Sample

1. Locate a 5 to 10 mL glass container with a 10 mm opening (in the drawers under the vacuum machine)
2. Use a few specks of powered soap to clean out the glass container
3. Scrub with a brush above the sink
4. Rinse several times with de-ionized water (at least 5 rinses)
5. Let air dry or dry with a paper towel
6. Add about 1-2 mL of the sample to be tested to the glass container
    a. If the concentration needs to be reduced follow the equation provided below (note that this requires that you have measured the concentration of the stock H_2O_2 solution; likely 0.882 [M]):

$$M_1V_1 = M_2V_2$$

7. Locate the aluminum cap with the pre-installed septum (in a drawer under the vacuum machine)
8. Locate the red cap clamper (found in the drawer next to the caps, the one with missing an arm)
9. Place the cap on the glass container and use the clamper to secure the cap on the container
    a. This process is important to insure that oxygen does not leak into the sample after de-gassed

    b. Apply pressure with your weight over the container as you clamp down
    c. Rotate the container to clamp down the part where the missing arm did not secure
    d. Sometimes multiple clamps helps, but sometimes it also could make it worse
10. Peirce the septum of the container with one of the needles of the vacuum machine (there should be several needles in a row that are pointed down)
    a. The container will hang off of the needle while it is being de-gassed
11. Turn the knob that is directly above the container's needle counterclockwise to open that passage way
12. Make sure that the other knobs above the other needles are closed
13. Turn the glass knob that is farthest to the left so that it is vertical (the blue side should be up for vacuuming)
14. Turn on the vacuum machine with the little black switch on the floor
    a. The machine should start glugging away
15. Let the vacuum work on the container for about a minute
16. Remove the container from the needle and flip the container upside down and check if any air bubbles come through
    a. If there are bubbles, the seal is not good enough
        i. Remove the cap with the specialized pliers with blue handles (found in the same drawer as the red clamper
        ii. Repeat steps 9 to 16 until no air bubble emerge from the septum
    b. If there are no bubbles, continue to the next step
17. Place the container on the needle again for a couple more minutes
18. Turn the glass knob 180 degrees to fill the container with nitrogen
    a. Do this until the sample stops rippling (about 5 to 10 seconds)
19. Turn the glass knob back to the vacuum (180 degrees) and leave it on for a few more minutes
20. Do one final nitrogen filling (repeat step 18)
    a. Make sure to end with nitrogen to not leave a vacuum on the container
21. Turn the glass knob to the horizontal position
22. Turn the knob above the needle being used until it is closed
23. Remove the container from the needle
24. Turn off the vacuum machine with the same black switch on the floor

E.2.3 Prepare the Electrochemical Cell

1. Remove previous solution from cell with large syringe
2. Add about 3 mL of buffer solution to the cell
    a. The solution should come above where the cell starts to get bigger but below the little arm that sticks out of the cell
3. The working electrode is a mesh and should already be in the cell
    a. The mesh should be positioned about in the middle of the buffer solution
4. Locate the reference electrode with a black rubber stopper in a nearby beaker
5. It is easiest to place this electrode through the small hole on the left toward the front of the cell
    a. The end of the electrode must be in the solution but positioned above the mesh of the working electrode

6. Locate the outer glass tube of the counter electrode in a 15 mL tube of saturated KCl (usually on the counter just on the other side of the wall where the vacuum machine is located)
    a. The glass tube is most easily taken out of the saturated KCl using the tip of the large syringe for leverage
7. Locate the wire that is the inner portion of the counter electrode (it should already be hooked up to the potentiostat)
8. Place the wire inside the glass tube
9. Place the two part electrode through the largest center hole of the cell
    a. Similar to the reference electrode, the end of the counter electrode must be in the buffer solution but above the working electrode
    b. The electrode end can rest on the knob of the working electrode where the mesh comes together into one wire
    c. Alternatively, tape can be placed around the center of the electrode to make it thicker and to hold it in place better
10. Locate the line for the nitrogen (a clear tube coming from the ceiling near the potentiostat)
11. Place the nitrogen line through the large hole that also has the counter electrode
    a. The nitrogen line does not need to be submerged in the buffer solution, just have it come right above the buffer surface
12. Turn on the nitrogen tank in the back corner of the adjoining room
    a. Little bubbles should form in the beaker on the counter to the right of the tank
13. Turn on the stirrer that is directly below the cell by turning the block knob on the stirrer until the white marker is approximately lined up the two pen lines drawn on the stirrer
    a. The stirring device can be very temperamental and may need to be adjusted slightly to get the stirring speed
14. Before turning on the potentiostat, make sure that the settings on the front panel of the potentiostat are correct
    a. The center black switch should be in the off position
    b. The A on the bottom left should be lit
    c. The switch under the A label under the Applied Potential should be set to the minus sign
    d. The number in the black box under A should be .800
    e. The operating mode should be on Contr. E
    f. The black part of the red knob under the display should point to current, while the white dot should point to 1
15. Turn on the potentiostat by flipping the switch under the display from “Off” to “Power”
16. Wait about 10 seconds for the machine to warm up
17. Apply voltage to the cell by flipping the black center switch from “Off” to “Ext. Cell”
    a. This is when the chemical reactions begin
18. The display will likely overflow initially, but by turning the black knob in the upper right to 10 mA, the range will be changed to be able to read the current
19. The current will go down very fast initially and can soon be changed to the 1 mA setting
    a. If small concentrations are being measured, the black knob can be turned once more to 100 μA setting
20. The cell will take about 30 minutes to reach its baseline current (about 5-15 μA)

E.2.4 Visualizing the Current in the Cell

1. Log on to the computer directly above the potentiostat (info is on the computer tower)
2. Click on the "Etch-A-Sketch" LabVIEW program shortcut on the desktop
    a. This can take several moments to boot up
3. Run the program by clicking the white arrow at the top of the screen (just under the edit tab)
    a. Make sure the electrochemical cell if on before running the program
4. Click the "Analog" button toward the top center of the program
5. Click the "X(V)" button at the top of the column of buttons in the upper right of the program
6. If you want to save the data, change the setting from "Don't Save" to "Save"
    a. Specify the name and location to save the file by clicking the folder under file name
    b. Make sure to change the name of the file for each run to avoid overwriting your data
7. Click the "Start/Stop" button
    a. A white curve should appear in the programs display
        i. If there is an error instead of a white curve, restarting the computer usually fixes this problem
    b. If the electrochemical cell was just recently turned on, there should be a fairly steep downward slope
    c. Once the cell reaches its baseline, the curve should be fairly level, although there will still be noise in the signal
    d. If you change the current setting on the potentiostat, this will change the units of the y-axis on the current plot and the curve will jump accordingly
    e. The y-axis will automatically adjust as soon as the data reaches the left side of the display
8. Adjust the time shown along the x-axis by changing the value of "Display last"
    a. Usually 150 to 250 seconds is a good range
9. Once done collecting data, click on the "Start/Stop" button again to stop the run
    a. The data will be saved to a "File" which can then be changed to a text file or opened directly in MATLAB

E.2.5 Running the Experiment

1. Start the LabVIEW program (as described in A.4.)
2. Let the program collect at least 1 minute of baseline data before injecting the sample
    a. This will allow for a sufficient number of points to get a good baseline average
3. Locate the 50 µL syringe (usually found on the counter next to the potentiostat)
4. Rinse the inside of the syringe by pulling water in and pushing it out several times
5. Pierce the septum of the degassed sample (from A.2.)
    a. Try to pierce a new location each time to avoid making any hole too large
6. Turn the container upside down so that the liquid is up against the septum
    a. This will allow you to reach the sample without sticking the needle so far in the container

7. Withdraw some of the sample (say 30 μL), remove the syringe and discard the drawn sample
    a. This will get the syringe ready for the experiment
8. Repeat steps 5 and 6
9. Slowly withdraw the sample into the syringe
10. There will likely be bubbles in the syringe, so quickly inject the sample back into container
11. Repeat steps 9 and 10 until there are no air bubbles
12. Continue to slowly withdraw until the desired volume is achieved
13. Carefully remove the syringe from the container
14. Inject the sample into the cell fairly quickly
    a. It works best to stick the needle of the syringe part way into the buffer solution
    b. The injection will cause a large abrupt spike in the current
15. Wait until the current curve levels back down to the previous baseline level
    a. This usually takes a few minutes, but will depend on the concentration and the volume injected
16. Stop the program to finish collecting data

E.2.6 Clean Up

1. Turn off the cell by flipping the black center switch from "Ext. Cell" to "Off"
    a. It is important to turn off the cell before turning off the potentiostat
2. Wait at least 10 seconds after turning off the cell, then turn off the potentiostat with the switch under the display from "Power" to "Off"
3. Turn off the stirring machine
4. Remove the nitrogen line and turn off the nitrogen tank
5. Place the reference electrode (the one with the rubber stopper) back in the beaker next to the potentiostat
6. Remove the counter electrode (the one with the glass) and leave the wire still attached near the potentiostat
7. The glass portion needs to be put back in the saturated KCl tube
    a. It is also good to shoot some of the saturated KCl solution into the glass tube with the large syringe that was used to put the buffer in the cell
8. Either leave the solution in the cell or remove it for a quicker start next time. Leave everything neat and tidy

E.2.7 Pictures of the Potentiostat Setup

Figure E-2: Sample being degassed.

Figure E-3: Potentiostat front panel (‘on’ position).

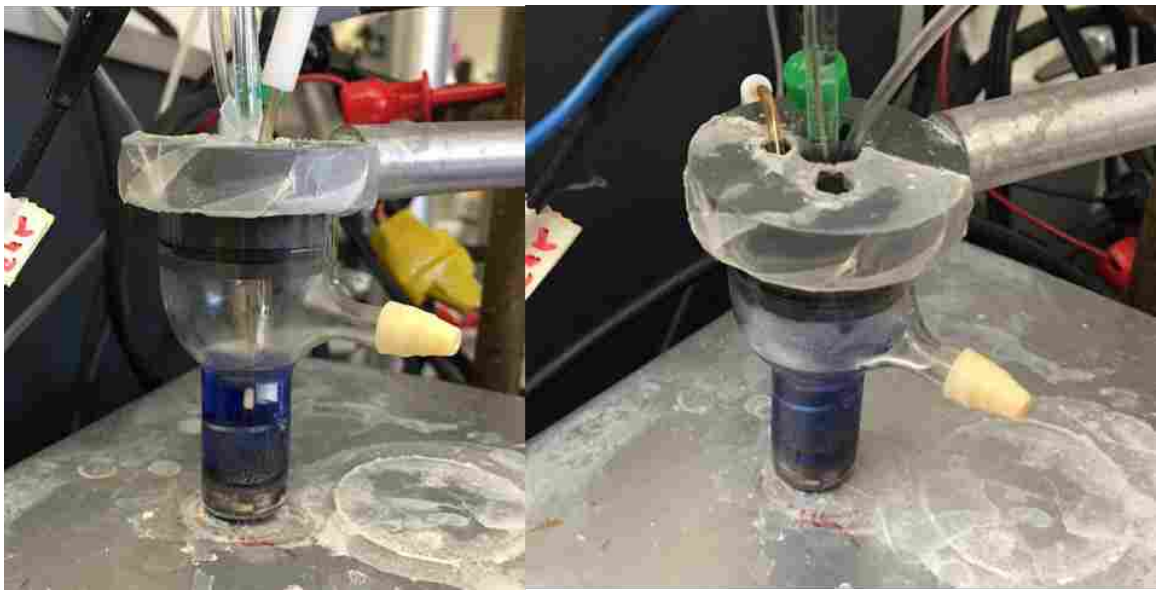

Figure E-4: Electrochemical cell (blue color from methyl viologen run).